

**MICROSTIMULATION AND MULTICELLULAR ANALYSIS:
A NEURAL INTERFACING SYSTEM FOR
SPATIOTEMPORAL STIMULATION**

A Thesis
Presented to
The Academic Faculty

by

James Ross

In Partial Fulfillment
of the Requirements for the Degree
Doctor of Philosophy
Department of Biological Engineering

Georgia Institute of Technology
August 2008

**MICROSTIMULATION AND MULTICELLULAR ANALYSIS:
A NEURAL INTERFACING SYSTEM FOR
SPATIOTEMPORAL STIMULATION**

Approved by:

Dr. Stephen DeWeerth, Advisor
Department of Biomedical Engineering
Georgia Institute of Technology

Dr. Michelle LaPlaca
Department of Biomedical Engineering
Georgia Institute of Technology

Dr. Robert Lee
Department of Biomedical Engineering
Georgia Institute of Technology

Dr. Steve Potter
Department of Biomedical Engineering
Georgia Institute of Technology

Dr. Bruce Wheeler
Department of Bioengineering
*University of Illinois at Urbana–
Champaign*

Date Approved: May 14, 2008

ACKNOWLEDGEMENTS

First, and foremost, I would like to thank my wife, Kyla. Whether in or out of the lab, graduate school brought with it some significant challenges. There were moments—like when I was climbing Kilimanjaro or dog sledding in the Alaskan arctic wilderness—that I would wonder, “how on earth did I get here?” The answer was always there, standing next to me (or usually ahead of me). Thank you, Kyla, for gracefully knocking down all of life’s obstacles, be they in travel or graduate school or wherever.

I would also like to acknowledge the DeWeerth group members—Richard Blum, Alex Bragg, Scott Buscemi, Shane Migliore, Mike Reid, Jevin Scrivens, Michael Sorenson, Kartik Sundar, JoAnna Todd, Carrie Williams, and Kate Williams. This was truly one of the most creative and fun groups one could hope to work with. Whether it was turning coffee straws and air canisters into weapons of war, or under-water beer drinking (not condoned by the university), or sneaking into the 4th floor faculty lounge (also not condoned by the university), or ‘punking’ the faculty, lab work was always a pleasure. I felt very fortunate to work among people with such exceptional talent; every aspect of this work benefited from their advice, mentorship, and assistance.

I am very grateful to my friends and family, who were very supportive throughout graduate school. Brian and Richard have a contagious energy, and their friendship keeps me propped up even when they are miles away. My mother, father, brother, and sister remind me of how much goodness there is in the world; they are a constant source of wisdom, perspective, and support. I am also grateful to Ken and Sandy, who welcomed me as one of their own when I married Kyla at the start of this graduate school venture.

This work could not have happened without some specific technical assistance. I am grateful to Mr. Swami Rajaraman for processing the kapton-based multielectrode arrays. Dr. Radhika Madhavan collected and analyzed the electrophysiological data for the impedance-dependant stimulation studies. Dr. Kacy Cullen acquired and categorized the 3-D cortical cultures and assisted in the statistical analysis of the 3-D image processing algorithms. Mr. Shawn O’Conner developed the physical interface to the impedance-controlled electroplating device. Mr. Scott Buscemi developed the lion’s share of ‘switchimus maximus’, an automated system that facilitated the rapid acquisition of electrode impedance data. I am also very grateful to Ms. Michelle Kykendall, Dr. Doug Bakkum, and Ms. Maxine McClain for their assistance in cell culture, dye labeling, and pharmacological manipulation.

In the course of this work, there were several people that considerably influenced the content of this thesis—Edgar Brown, Dr. Steve Potter, and Nakul Reddy. Edgar, thank you for your tireless mentorship and ‘dry erase’ discussions; whether it was advice on circuit design or ‘debates’ on neural excitation mechanisms, this work was significantly influenced by our discussions. Dr. Steve Potter, thank you for not only shaping and editing the content of this thesis, but also for providing significant mentorship and resources on electroplating, cell culture, and all things optical (dyes, microscopy, imaging, etc.), all of which were instrumental in developing the automated Ca^{2+} imaging system. Finally, Nakul, thank you for your tremendous assistance in assembling the Ca^{2+} imaging system; the scripts that you wrote to coordinate and

automate the optical acquisition of Ca^{2+} data will be continue to be useful for many generations of grad students.

I am very grateful to my advisor, Dr. Steve DeWeerth, who was one the primary visionaries behind the Neurolab, a confederation of principle investigators, in which its members are encouraged to collaborate and ‘play’. Under Dr. DeWeerth’s guidance, multidisciplinary research bears no obstacles. The neurolab provides experts on almost any subject (mathematics, biology, electronics, MEMs, chemistry, etc.) with equipment resources to match. This work could not have happened without such people and resources. I would like to also thank all of the members of my committee—Dr. Bob Lee, Dr. Michelle LaPlaca, Dr. Steve Potter, and Dr. Bruce Wheeler. This work significantly benefited from their advice and mentorship.

TABLE OF CONTENTS

	Page
ACKNOWLEDGEMENTS	iii
LIST OF TABLES	x
LIST OF FIGURES	xi
LIST OF SYMBOLS AND ABBREVIATIONS	xxii
SUMMARY	xxiii
CHAPTER 1: INTRODUCTION	1
1.1 Multielectrode Arrays	2
1.1.1 MEA Design	3
1.1.2 MEA Applications	4
1.2 Cell Imaging	5
1.2.1 Static Fluorescence Imaging	5
1.2.2 Functional Fluorescence Imaging	6
1.2.3 Image Processing	7
1.3 Selective Stimulation	8
1.3.1 Limitations in Spatiotemporal Stimulation	9
1.3.2 Temporal Manipulations	10
1.3.3 Spatial Manipulations	10
1.4 An Experimental Platform for Selective Stimulation	12
CHAPTER 2: MICROELECTRODE TECHNOLOGIES: INTERFACING NEURAL CELLS	14
2.1 Microfabrication of MEAs	15
2.1.1 Glass MEAs with Integrated Electronics	16

2.1.2	Kapton MEAs on Manufactured Substrates	19
2.1.3	Design Tradeoffs: Choosing a Process	23
2.2	Electrode Conditioning	23
2.2.1	Linear Electrode Models	25
2.2.2	Impedance Manipulations	28
2.2.3	Closed-Loop Electrode Deposition	30
2.2.3.1	Electroplating Feedback Strategies	30
2.2.3.2	Electroplating Device	32
2.2.4	Results	36
2.2.4.1	Device Performance	37
2.2.4.2	Pulsed Plating Performance	39
2.3	Applications to neural Stimulation	40
2.4	Discussion	43
CHAPTER 3: IMAGE PROCESSING TECHNOLOGIES: OBSERVING NEURAL CELLS		46
3.1	Automated 2-D Somata Segmentation	49
3.1.1	Color Filtering and Global Thresholding	51
3.1.2	Optional Morphological Filtering	52
3.1.3	Distance Transforms	52
3.2.4	2-D Watershed Segmentation and Object Classification	53
3.2	Automated segmentation of 3-D somata	55
3.2.1	Algorithm Overview	55
3.2.2	3-D Merging and Error Identification	56
3.2.3	Software Assisted Manual Validation	59
3.2.4	Algorithm Performance	61
3.2.4.1	Test Cultures	61

3.2.4.2	Defining the ‘Gold Standard’	63
3.2.4.3	Validation Methodology and Statistical Analysis	65
3.2.4.4	Validation Results	66
3.3.4.5	Sensitivity to User-Defined Parameters	68
3.3.4.6	Performance Validation in Brain Slices	70
3.3	Automated Tracking of Functional Activity	71
3.4	Discussion	75
CHAPTER 4: AUTOMATED CELLULAR TRACKING: ELECTRICAL STIMULATION AND OPTICAL MONITORING		79
4.1	High Throughput Stimulus Tracking	80
4.1.1	Biological Design	81
4.1.1.1	Neural Cultures	81
4.1.1.2	Fluorescent Ca^{2+} Dyes	82
4.1.1.3	Pharmacological Synaptic Blockers	83
4.1.2	Hardware and Software Design	84
4.1.2.1	System Overview	84
4.1.2.2	Stage Control	86
4.1.2.3	Experimental Sequencing	87
4.1.2.4	Signal Conditioning and Data Extraction	88
4.1.2.5	Inputs and Outputs	91
4.2	Results: Analysis of Evoked Activity	93
4.2.1	System Validation: Tracking Neural Thresholds	93
4.2.2	Spatial Excitation Patterns	99
4.2.3	Inhibitory Stimulus waveforms	100
4.2.3.1	Mechanisms for Cellular inhibition	101
4.3.3.2	Characterization of Inhibitory waveforms.	102

4.3 Discussion	107
CHAPTER 5: DISCUSSION	113
5.1 Novel Contributions of this Work	113
5.3 System Applications and Future Work	116
5.3.1 Research Applications	116
5.3.2 System Improvements	118
5.3.3 Field Sculpting	119
5.3.4 Simultaneous Optical and Electrical Recording	120
5.4 Conclusions: Taking a Lesson from the Cells	120
APPENDIX A: THE MODELING AND MANAGEMENT OF STIMULATION ARTIFACTS	122
APPENDIX B: ELECTROPLATING HARDWARE AND SOFTWARE	139
APPENDIX C: BIOLOGICAL PROTOCOLS	142
REFERENCES	144

LIST OF TABLES

	Page
Table 2.1: Reference table for electrode shaping	29
Table 3.1: Description of 3-D neuronal culture parameters by category number	64
Table 3.2: Results	67
Table 4.1: System Specifications	85

LIST OF FIGURES

	Page
<p>Figure 2.1: Fabrication and testing of glass MEAs. (A-F) Custom microfabrication steps for producing MEAs with electronics designed by (Harrison 2003) directly integrated onto the substrate. This integration strategy enables high channel count MEAs by shrinking the spring-pin pad sizes (2x3 mm) to wire-bond pad sizes (100 x 100 μm). Note the differences in scale between the wire-bonding pads (surrounding the chip) and the spring-pin pads (surrounding the MEA). Integrated circuits with on-board analog or digital multiplexers would significantly reduce the amount of output pins required to interface the device. (G) Photograph of the completed MEA. (H) Recordings performed on the MEA (note: shown signals are were not routed through the wire-bonded chip; sample signals from the chip may be found in (Blum 2003)).</p>	18
<p>Figure 2.2: Fabrication process for post-processing on manufactured PCB substrates. (A) The minimum required processing steps for high channel count MEAs on interconnecting substrates. Note that PCB vias enable simple back side connections to the MEAs. (B) an alternative strategy that enables multi-layer wiring for higher-density electrode configurations and also provides additional encapsulation from cytotoxic materials.</p>	21
<p>Figure 2.3: Post-processing of PCB substrates for the development of MEAs. (Two layer method outlined in Sec. 4.2.2.) (A) Custom Kapton FlexBoard™ PCB substrates with patterned wiring traces and microelectrodes. (B) Close-up of the micro-electrode area of a processed substrate. (C) Micro-photograph of the area in which the microfabricated traces contact the PCB traces (gold traces in the PCB are 25 μm thick 200 μm wide, microfabricated traces are 0.5 μm thick 30 μm wide). (D) Differential interference contrast microphotograph focused on the SU-8 top surface in a section of the electrode area. Lighter and darker areas are a result of constructive and destructive light interference; this highlights surface features in the sub-micron scale. The planarizing effect of thin (3.4 μm) SU-8 smooths the surface roughness of the PCB from its original 5 μm variations down < 200 nm variations (profilometer data not shown). Impedance measurements show that the gold electrodes are viable with a mean impedance magnitude of 191 KΩ at 1 KHz.</p>	22
<p>Figure 2.4: Electrode modeling. (A) The impedance magnitude of microelectrodes is represented by an interface capacitance, C_I, shunted by a charge transfer resistance, R_T, in series with the spreading resistance, R_S. (B) Demonstration of model accuracy: The model in (A) was tuned to match the impedance magnitude of a 10μm diameter Au electrode using a multidimensional unconstrained nonlinear minimization method (i.e. the Nelder-Mead method).</p>	28
<p>Figure 2.5: Shaping the impedance spectrum of modeled microelectrodes. By careful manipulation of the electrode's physical elements—electrode material, base area, and surface area—one can control individual model parameters (Gray band indicates the</p>	

area of interest for recording neural action potentials). (A) Changes in the electrode material or electrolyte composition, J_o , modifies the charge transfer resistance and the impedance magnitude at low frequencies. (B) Likewise, changes in the electrode surface area, A_s , modify both the charge transfer resistance and interfacial capacitance to alter low- and mid-band impedances. (C) Finally, changes in the base area, A_B , of the electrode directly influence the spreading resistance or impedance magnitude at high frequencies.

29

Figure 2.6: Impedance controlled electroplating strategies. (A) A sinusoidal, single-frequency voltage source, V_m , is capacitively coupled onto a DC electroplating current, I_S . The impedance magnitude is sampled continuously until the impedance of the electrode reaches the target level (It is important to note that the lumped circuit model of section 2.1 does not capture the non-linear dependencies of impedance on electrode voltage; thus the applied electroplating current will place the electrode into a different measurement regime than under zero-current conditions). (B) A potentially more robust alternative to DC plating is to sample the impedance between brief bursts of pulsed electroplating current.

32

Figure 2.7: High level schematic and illustration of the closed loop electroplating system. (Left) System level schematic of electroplating circuitry. A computer, via a serial connection to a PIC 16F73 microcontroller and custom circuitry, switches electroplating current onto individual electrodes. A 1 KHz sine wave is capacitively coupled (not shown) across the reference resistor and plating bath; the waveforms across the reference resistor and bath are sampled with the PIC A/Ds and communicated back to the computer for processing. (Right) Illustration of electroplating. During electroplating, the MEA electrode surface becomes negatively charged and attracts positive platinum ions. As the surface area increases, the impedance magnitude of the electrode at 1KHz decreases.

35

Figure 2.8: System integration of the electroplating device. The switching circuitry and impedance measuring electronics are physically separate from the electrode array (a ribbon cable, not shown, connects the two sections). Electroplating solution is introduced into the culture well of the MEA and a Pt-wire anode is inserted into the solution.

35

Figure 2.9: Automated impedance measurement tool. (A): System level schematic of Impedance diagnostic tool. Over 206 switching elements enable impedance measures of virtually any conformation, including common ground and intra-electrode schemes. (B) High level schematic of the switching and impedance measurement circuit. (C&D) Photograph of the impedance measuring system.

37

Figure 2.10: Reduction in electrode impedance variability. (A) Impedance Magnitude for (1) untreated 30 μm diameter Au electrodes in an Ayanda Biosystems MEA (MEAv5), and (2) platinized electrodes with a target impedance of 75 K Ω at 1KHz. (B) Coefficient of variation (Standard Deviation divided by the mean) for a set of 10 after electroplating (blue traces). Electroplated platinum black electrodes traditionally have

substantial variation in their impedance magnitudes. For example, (Franks 2005) report variations of 600%. 38

Fig. 2.11: Independent electrode control. (A) Optical micrograph of an electroplated Ayanda Biosystems MEA (MEA60Au). Each 30 μm Au electrode within a quadrant of the planar MEA was electroplated with platinum to match impedances. Various plating densities (clockwise from left: w, x, y, and z $\mu\text{A}/\text{cm}^2$) produced different surface morphologies corresponding to different colors). The red circles indicate three electrodes that were electroplated without feedback (B) In a separate study on a different MEA, each square (dashed line) represents an individual electrode in an 8X8 MEA. The outer perimeter of each square indicates the targeted impedance magnitude at 1Khz ($\text{K}\Omega$), and the inner square represents the actual impedance value achieved by the device (clockwise from left, target impedance values of 50 $\text{K}\Omega$, 100 $\text{K}\Omega$, 15 $\text{K}\Omega$, and 75 $\text{K}\Omega$ respectively). 39

Figure 2.12: Electrode Robustness. Electrodes were subjected to 30 seconds of ultrasonic agitation to emulate mechanical wear on the MEA devices. Shown is the shift in mean impedance for both DC and pulsed plating methods. When normalized for mean relative shift, this graph indicates that electrodes that underwent DC plating shifted 3.5 times more than pulsed-plated electrodes. 40

Figure 2.13: The effect of impedance on the cellular response to stimulation. (A) Normalized V_{max} as a function of the stimulus voltage and electrode impedance using the model depicted in Fig 1A. For a given stimulus input, the nominal impedance electrode (blue trace: $R_s = 10\text{K}\Omega$, $R_M = 1\text{K}\Omega$, $C_1 = 3\text{pF}$, $\Delta t = 10\text{ ns}$) presents a lower V_{max} to the culture dish than the lower impedance electrode ($C_{1,2} = 4 \times C_1 = 12\text{ pF}$) (B) The cellular response (as a function of stimulus magnitude) of a low impedance electrodes (15 $\text{K}\Omega \pm 4$) is compared to a high impedance electrodes (75 $\text{K}\Omega \pm 12$). Cellular Response is defined as the total number of spikes, recorded across the entire dish, that occur within 50 ms of a stimulus. Biphasic pulses with random inter stimulus intervals and random order of magnitudes were applied to the electrodes. Low impedance electrodes were able to elicit a greater cellular response for a given stimulus magnitude. 43

Figure 3.1 Flow diagram for the 2-D segmentation of cell bodies. (Top) Flow diagram for 2-D segmentation. Graphic representation of 2-D segmentation process: (A) The color component for the fluorescent dye of interest was extracted to form an achromatic intensity image; (B) A global threshold was applied for each 2-D frame in the z-stack, separating pixels into foreground (regions of interest) and background; (C) The regional minima were defined by applying the Euclidean distance transform (or alternatively the chebyshev transform) to the 'thesholded' image; (D) The watershed algorithm was applied to the transformed image: the mottled contours of the neurites produced very fractured segmentation boundaries, while the rounder, smoother morphologies of the soma produced accurate segmentation boundaries; (E) Objects were classified as either soma or neurite fragments according the area enclosed by the watershed lines, and neurite

fragments were removed from consideration. (F) Picture of the cell body boundaries projected back onto the original image. 50

Figure 3.2 Distribution of segmented objects binned according to pixel area. The morphological differences between neurites and somata produce watershed segmentation boundaries that, when binned according to pixel area, fall into two distinct populations. The threshold, α (vertical, dashed line), is used to separate objects into neurites and cell-bodies. Objects with a pixel count or area $\geq \alpha$ are labeled ‘cells’; objects with an area $< \alpha$ are labeled ‘neurite fragments’. (Inset) Watershed boundaries for somata and neurite fragments. 55

Figure 3.3: Illustration of 3-D merging and error identification. (Left) This figure exemplifies segmentation results for three cells—A, B, and C—which appear in frames F_i , F_{i+1} , and F_{i+2} . In Frame F_{i+1} , we show three correctly segmented somata. In Frames F_i and Frames F_{i+2} we illustrate over-and under-segmentation errors respectively. 2-D objects are merged into 3-D cell bodies if the percentage overlap between the objects is $\geq \beta$, where β can be any number between 0 (no overlap) and 1 (100% overlap). The merging algorithm considers two frames at a time, and segmentation errors are identified when multiple objects in a single frame exceed β . (Top Right) For example, cell B from frame F_{i+1} was projected into F_{i+2} . All object(s) in F_{i+2} that overlapped with B’s projection (dashed cell boundary) were considered as merging candidates; in this case, the object B+C satisfied the percentage overlap criteria. However, the reverse projection of B’s best merging candidate, B+C, back onto the previous frame identified two objects that satisfied the merging criteria: B and C. Because three objects—B, C, and B+C—were eligible for merging, the under-segmentation error was identified (gray box). (Bottom Right) In a similar fashion, the forward projection of A_1 into F_{i+1} overlapped best with A; however, the reverse projection of A_1 ’s best merging candidate significantly overlapped with two objects: A_1 and A_2 , thus identifying a 2-D segmentation error. 57

Figure 3.4: Illustration of software tools. The segmentation algorithms were integrated into a graphical user interface (GUI) to facilitate visual feedback, parameter selection, and software-assisted error correction. (A) Segmentation boundaries (white) are projected onto individual frames in the z-stack (a scroll bar, not shown, is used to switch between frames.) Segmentation data, including cell ID number, area, and diameter (white box), are displayed for a selected cell. (B) Potential segmentation errors are automatically flagged in red. (C) A user-applied mouse command instructs the software to perform a merge operation. Blue pixels outline the object in the forward adjacent frame that is connected to the merged cell. (Gray pixels, not shown, indicate connected objects in the previous frame.) 60

Figure 3.5: Image testing categories. Variation in testing conditions was achieved by dividing cultures into four categories based on culture complexity. Levels one through three consisted of mainly spherical neurons with increasing amounts of neurite outgrowth. Specifically, (A) level one had spherical neurons with few neurites and no cell clustering; (B) level two had mainly spherical neurons with increased neurite outgrowth and little clustering; (C) level three had robust neurite outgrowth with increased cell

clustering (yellow circles). Finally, (D) level four had increased complexity due to more diverse, non-spherical neuronal morphologies (white circle), cell clustering (yellow circle), and significant neurite outgrowth. Images are 2-D reconstructions of confocal z-stacks (100 μm total thickness); scale bar = 50 μm . 62

Figure 3.6: The total error percentage, defined as the number of false positives counts plus the number of false negative counts in comparison to the actual number of cells, was calculated for levels one through three (spherical morphology with increasing levels of neurite outgrowth) and level four (complex morphology with high neurite outgrowth). Two-way repeated measures ANOVA revealed that the total error was reduced by the presence of automated error correction ($p < 0.001$), and was further reduced by correction of software-identified probable error points ($p < 0.05$). Tukey's post-hoc pair-wise comparisons revealed significant error reduction within levels two through four; asterisks denote significant reduction in total error percentage versus "Before Automated Error Correction" within each level (* $p < 0.05$; ** $p < 0.01$; *** $p < 0.001$). 67

Figure 3.7: Sensitivity to user-defined parameters. Cell count error as a function of α and T both with (A) and without (B) 3-D error correction. The dashed box indicates the region of parameters an operator would likely select based on histogram data from the software. In (A) the 5% error region occupies 44% of the shown parameter space; in contrast, the same error region occupies only 18% of (B). In (A), the removal of neurite segments and the merging of over-segmented somata accounts for the reduced sensitivity to user defined parameters. 69

Figure 3.8 Demonstration of system robustness: soma segmentation in ex vivo brain tissue. Custom 3-D segmentation algorithms were applied to z-stacks attained from confocal imaging of brain slices from cerebral cortex. The z-stacks tested varied based on the density of viable cells, ranging from relatively low (A) to high (B) densities. Following the same protocol of the in vitro testing, the algorithms achieved accuracies of 93% (A) and 97% (B) ($\alpha = 50$, $\beta = 0.15$, $T_A = 80\%$, $T_B = 95\%$). 70

Figure 3.9 Tracking evoked behavior. A priori knowledge about the cellular response to an externally applied stimulus can be used to rapidly identify stimulated cells. (A) An image captured before the application of the stimulus (t_1) can be subtracted from an image captured during the peak response (t_2). This so-called difference image is illustrated in (B). Images captured at two points in time, t_1 and t_2 , look very similar. However, subtracting the two images clearly identifies the objects that changed. Image segmentation routines can be applied to the difference image to automatically identify the boundaries of changed/stimulated objects (black outlines). 72

Figure 3.10: Process flow for tracking evoked in 2-D cultures. (A) Estimations for peak and base-line activity are used to identify the frames used in image subtraction in (B). Simple optimizations can be used to determine the true peak response. (C) Optional: Non-linear intensity transforms are applied to the difference-image to enhance contrast in preparation for object segmentation. (D) The 2-D segmentation and classification algorithms of section 3.1 are used to distinguish somata from 'illuminated' neurites. (E)

Following the identification of stimulated cells from the difference image, the full fluorescence waveforms are extracted and stored in a database (F) that relates the response to the stimulus parameters.

73

Figure 3.11: Functional image processing. (A) The image from the average of 15 frames measured before the stimulus event. (B) The image from the average of 15 frames at the anticipated peak of the response. (C) The difference image. (C) The image processing algorithms were written in Matlab (Mathworks, version 7.01) and integrated into a graphical user interface (GUI) that was designed to facilitate parameter selection, visual feedback, and user-guided edits. Shown in the figure is a difference image of 15 averaged frames measured at the peak of the response subtracted by 15 averaged frames at the base-line response (gray bars on the blue $\Delta f/f$ trace) The following features were incorporated into the GUI: (1) databases for maintaining cell coordinates and boundary information, (2) histograms and segmentation statistics for assisting parameter selection, (3) saving and reloading options for revisiting and revising image-movies, (4) computer assisted manual segmentation for error correction, (5) morphological operator and process selection for preprocessing, (6) idealized graphic reconstructions of segmented cultures, and (7) automated signal extraction for individual cells.

74

Figure 4.1 System level schematic of stimulus tracking system (Counter clockwise from top left) Matlab scripts specify stimulus sequences and synchronization pulses that are transferred via USB to an arbitrary waveform stimulus generator (Multichannel systems, STG-2004). A software trigger engages the stimulus generator, which applies the current waveforms to electrodes in an MEA docked in a recording preamplifier (Multichannel systems, MEA-1060). In total, four independent trigger pulses can be used to synchronize activities among the shutter, camera, stimulator, and preamplifier. Automated stage positioning (Intelligent Imaging Solutions, MS-2000) enables precise, arbitrary stage positioning. Following optical recording of the evoked response of the stimulus sequence, a new stimulation sequence is transmitted to the stimulus generator and the process is repeated. Although the present system runs open-loop scripts to vary the stimulus input and record evoked responses, automated image processing routines present an opportunity to implement closed loop control in the future.

85

Figure 4.2 Automated stage displacement. Electrode coordinates were mapped to stage displacements by measuring the stage coordinates when the microscope was manually positioned over four corner electrodes. An affine transformation related electrode coordinates into stage displacements. Arbitrary control of the stage (to within 2 μm), enabled observation of the cellular response well outside of the 400 x 400 μm field of view (20x objective).

86

Figure 4.3 Sequencing formula for stimulus application and synchronized optical monitoring of evoked activity. (A) The microscope is positioned over the array using an electrode-based coordinate system. A typical 8x8 array, with 200 μm center-to-center electrodes, could be observed with approximately 16 separate stage displacements (indicated by dashed lines). (B) The stimulation and optical monitoring instruments are programmed and queued for triggering, which includes selecting the electrodes and

specifying the arbitrary stimulus waveforms. (C) The shutter, camera, and stimulus system are triggered in sequence (the optional electrical MEA recording system may be triggered as well). The timing is managed such that camera captures both base line and recovery activity. 88

Figure 4.4 Maximizing the signal-to-noise ratio. Signal processing techniques for evaluating evoked-response patterns. (A) Stimulation waveforms are repeated n times (10 shot illustrated) with 50 - 100 ms inter-stimulus intervals (optimized based on Ca^{2+} signaling decay). (B) This n -shot stimulus sequence is repeated m times to further enhance the signal with triggered averaging. Subtraction of t_b averaged frames of base-line activity from t_p averaged frames at the peak of Ca accumulation (gray bars), produces high contrast images like the one shown in (C). Automated image segmentation routines are used to identify the cellular boundaries of each stimulated soma (gray outlines indicate soma boundaries), which facilitates spatial averaging (D) and quantification of stimulus-induced changes in evoked action potentials. 89

Figure 4.5 Managing the system inputs and outputs. (Left) Illustration of how a simple script is translated into experimental execution. (Right) Illustration of the database structure. Shown is a sample of the data fields for each of the three main data categories (1) Soma image information, (2) Stimulus trial conditions, and (3) Raw calcium data. It is important to note that raw Ca data is recorded in every trial for any segmented cell body, regardless of whether a particular stimulus trial elicited a response. Such data enables direct comparison between stimulus trials. 92

Figure 4.6 Experimental design for the evaluation of excitatory cathodic current pulses. 25 cathodic current pulses swept from from -10 uA to 50 uA and 100 us to 500 us (in 10 uA and 100 us steps respectively) were applied to 11 different electrodes (gray dots) with the microscope field of view (blue line) centered over the electrode. In actual experimentation, the fields of view were chosen such that there was no spatial overlap between trials. 94

Figure 4.7 Illustration of Ca^{2+} data extraction. Within the graphical user interface, the high contrast image of stimulated somata is depicted with automatically segmented boundaries. Shown, in blue traces, are the calcium signals ($\Delta f/f$ over time) extracted from three of the stimulated cells for all 25 stimulus conditions (sorted by charge). Arrow indicates the direction of increasing stimulus charge (Range: 1 to 25 nC). 95

Figure 4.8 Charge-based threshold tracking. The average relative fluorescent intensity at baseline is subtracted from the averaged peak response and plotted as a function of the applied stimulus charge. The red trace depicts a sigmoid curve fit, in which the fit error (sum of squares) was minimized by a Nelder-Mead non-linear regression using the optimization toolbox in Matlab. (Inset) Shown are 25 individual fluorescent intensity traces for cell (c) (Figure 4.7). The gray trace indicates that the neuron only fired four action potentials during the ten shot stimulus. The gray data point on the sigmoid curve fit represents the peak response of this trace. In general, sampling the evoked response in two dimensions (pulse, amplitude) and then mapping to one (charge) may provide a very

robust measure for determining the threshold (as the 2-D sweep samples a very broad stimulus space).

97

Figure 4.9 Characterization of neural threshold behavior. (A) The slope of the sigmoid describes the probability that a given stimulus will evoke a response (or, alternatively, how well cellular excitation is modeled as a switch). The distribution for the full set of slopes spans approximately two orders of magnitude and is depicted in log scale. The mean slope is approximately 3.5 (1/nC), which indicates that the threshold is an accurate predictor of the cell firing to within ± 0.8 nC. At the extremes of the distribution, a slope of 0.3 and 30 would be accurate to within ± 8 nC and ± 0.1 nC respectively. (Inset) Histogram of sigmoid slope on a linear scale. (B-D) traces depict sigmoid curves with slopes of 0.3, 1, and 8. The higher the slope, the more likely the cell is to behave in an off-on, switch-like fashion. The wide range in threshold behavior could potentially be related to the geometry of the cell with respect to the stimulating electrode.

98

Figure 4.10 Excitation parameters as a function of space. The 30 μm diameter electrode is in the center of the field of view. (A) Firing threshold (nC) for each cell. (B) Firing threshold (nC) in which only cells with a 95% probability of firing within ± 1 nC of the threshold are depicted. (C) Threshold tolerance (log of slope) or the degree to which a cell behaves like a switch in response to a stimulus charge. (1/nC) (D) Cells are binned according to the electrode that stimulated them, demonstrating that there was very little clustering between trials.

100

Figure 4.11 Experimental design for the evaluation of monopolar temporal inhibition. Although it is not practical/feasible to temporally sum voltage fields at targeted cells and tissue, the neural membrane and ion-channel time constants introduce a temporal component that can be used to sculpt regions of excitation. (A) Stimulus pulses were swept over one electrode to investigate the duration of the inhibitory effect. Accordingly, the interval between the inhibitory prepulse and excitatory control pulse, Δt , was varied and the Ca response observed. (B) Pre-pulse parameters (i.e. amplitude, duration) were swept over five electrodes to evaluate the pre-pulse efficacy for modulating single cell excitability in dissociated cortical cultures (-2 to $-10 \mu\text{A}$ in $-2 \mu\text{A}$ intervals and 2 ms to 10 ms in 2 ms intervals; Stimulus control pulse was $-60 \mu\text{A}$, $400 \mu\text{s}$). For studies (A) and (B), the field of view ($400 \times 400 \mu\text{m}$ blue boxes) was centered over the electrode of interest. (In actual implementation, there was no spatial overlap between recordings.)

103

Figure 4.12 Depolarizing pre-pulses transiently inhibit neuronal excitability. (A) Background subtraction image illuminates cell bodies that were stimulated with a 2 ms, $-5 \mu\text{A}$ pre-pulse followed by 0.4 ms, $-20 \mu\text{A}$ stimulus (the crossbars indicate the stimulation site). (B) Extending the pre-pulse duration three-fold to 6 ms suppressed stimulation in most of the neurons. The segmentation boundaries indicate somata with suppressed activity. (C) In a separate study, the time interval between the pre-pulse ($-5 \mu\text{A}$, 4 ms) and stimulus ($-30 \mu\text{A}$, 0.4 ms) was adjusted to determine the length of time for which activity was suppressed. Shown are changes in fluorescent intensity ($\Delta F/F$) for one of the

suppressed neurons. (D) For the same neuron, Peak $\Delta F/F$ plotted as a function of the time interval between the pre-pulse and stimulus. The cell becomes excitable again around 3ms after the pre-pulse. Normal activity is resumed around 7ms. 104

Figure 4.13 Relative changes in neural excitability. Depicted in each graph is a histogram of cell counts (y axis scale: 0 to 40 cells) as function of relative excitability as it relates to the stimulus amplitude and duration (x axis scale: 0 to 2, where 0 and 2 indicate a 100% decrease and increase respectively in relative excitability.) Shaded blue region indicates relative inhibition; Red region indicates relative excitation. Cross bars depict the mean and standard deviation. Higher amplitude, longer duration sub-threshold inhibitory pulses induce a near global reduction in relative excitability. The left most bar of each histogram indicates the number of cell for which there was $\leq 5\%$ chance that an action potential would be evoked under the relevant stimulus conditions. 105

Figure 4.14 Percentage of cells that were either relatively inhibited or excited as a function of stimulus charge. Stimulus pre-pulses on the order of 100nC achieve near global reduction in neuronal excitability within the microscope field of view. Red trace indicates the percentage of cells which experienced a relative increase in excitability. The blue trace, in contrast represents cells that were relatively inhibited. (Inset) Percentage of cells that were either 100% inhibited (blue trace) or at least marginally excitable (red trace.) 106

Figure 4.15 Spatial relationship of relative excitability to soma-electrode distances. 30 μm TiN stimulating electrode is in the center of the picture. (A) Relative change in excitability for a 100 nC stimulus pulse (0 indicates 100% inhibition, 1 indicates no change in excitability, and 2 indicates 100% increase in excitability). (B) Cells were color coded blue if they were relatively inhibited and red if they were relatively excited. Picture demonstrates near global inhibition in the vicinity of the electrode. 107

Figure 4.16 Future studies: Multipolar lateral inhibition: (A) A ‘moat’ of inhibition could potentially be created by applying inhibitory prepulses to electrodes surrounding the cells of interest while an excitatory pre-pulse is applied to the center electrode. The application of prepulses could be used to enhance sensitivity to extracellular stimuli in the center while reducing sensitivity in the periphery. This allows for the application a *low-amplitude* excitatory pulse to the target area, which could further improve spatial control of the stimulus. (B) Model of voltage fields during the prepulse conditioning stage as captured 20 μm above the dish. 110

Figure A.1: Circuit diagram for the non-linear electrode model and stimulation circuitry. 126

Figure A.2: Non-linear Simulink model of the electrode and stimulation artifact. 127

Figure A.3: Voltage Trace measured at V_r both without (A) and with (B) switching circuitry present. 128

Figure A.4: Voltage Trace measured at V_r demonstrating that charge is trapped on the electrode. 128

Figure A.5: Artifact elimination technology (A) micrograph of custom IC for simultaneous stimulation and recording. White box highlights the electrode control circuitry for a single electrode, for which a high level schematic is depicted. (B) The stimulating, recording, and artifact elimination circuitry integrate the electrode into a feedback loop, which is capable of removing accumulated charge at the electrode-electrolyte interface. 131

Figure A.6: Definition of Artifact Duration. Example of the output of the recording system after a $\pm 500\text{mV}$, $200\text{ }\mu\text{s}$ per phase stimulation and a 2 ms discharge (not enough to eliminate the artifact). This 25 trace recording is a transient behavior at the initiation of 8 Hz periodic stimulation (darker traces happened later in time). The artifact variability can be seen to converge towards a narrow range of values. The initial spike (as the main amplifier is turned on), and the relatively flat region that follows, is due to the activity of the discharge loop. In this case the recording system saturates at approximately 2.25mV . The inset shows the artifact duration depending on the chosen threshold (the shading corresponds to the thresholds indicated by dashed lines in the main figure). 133

Figure A.7: Artifact duration after an initial discharge period of $500\text{ }\mu\text{s}$ at $10\text{ }\mu\text{A}$: (a) Set of time traces of artifact data with a discharge current of $10\text{ }\mu\text{A}$ parameterized by discharge time, the arrow indicates the direction of increasing discharge time. (b) Artifact duration with respect to discharge time parameterized by discharge current (logarithmically spaced, 20 current traces from $10\text{ }\mu\text{A}$ to $0.1\text{ }\mu\text{A}$). The dashed line corresponds to a higher artifact threshold of 2mV (the sloped region is the total discharge time as the artifact does not exceed the threshold). (c) 3-D representation of the data set from (b). Note that the artifact duration slightly worsens for larger discharge currents and times. 134

Figure A.8: Soft transients improve recording performance. Example of two artifacts with (black) and without (gray) a soft transition between the high and low discharge currents. The bottom plot shows R_{disch} for each curve; both start and stop at the same values and have a total discharge time of 3.5 ms . The initial peak saturates the amplifiers though the higher currents make it too fast to be captured at this sampling rate. The gray regions denote the areas in which the corresponding amplifiers are turned off. Note that the larger overall current (smaller overall R_{disch} value) performs worse than having a smooth transition. 135

Figure A.9: Artifact duration with respect to pole shift time and frequency after a discharge period of 1 ms at $5\text{ }\mu\text{A}$, followed by 1.5 ms at $1\text{ }\mu\text{A}$. The pole shift effect is additive to the recording high-pass frequency of 200 Hz (the frequencies shown are actual high-pass values): (a) Set of time traces of artifact data with a pole shift frequency of 800 Hz parameterized by pole shift time, the arrow indicates the direction of

increasing pole shift time. (b) Artifact duration with respect to pole shift time, parameterized by pole shift frequency. (c) 3-D representation of the data set from (b). 136

Figure A.10: Graphical user interface for designing stimulus waveforms and managing the artifact elimination parameters. The interface, which translates user specified parameters into PIC microcontroller commands, is divided into five sections, which clockwise from the bottom left are (1) Electrode Selector: Allows the user to turn individual recording channels on or off as well as designate which channel(s) are used for stimulation. (2) Stimulation: A panel for specifying the stimulation and discharge parameters, which are graphically represented in (3) Graphic Panel: The red phase designates the stimulus profile, the dark and light blue phase represent the duration of the 1st and 2nd discharge phase respectively. The vertical dashed and solid line indicate the 1st and 2nd Poleshift phase respectively. (4) Terminal: The terminal displays microcontroller commands that are echoed back from the microcontroller. Finally, (5) Biasing Panel: a multilevel text entry panel for setting the chips biases. Inputs, such as high pass cut off frequency, are mapped through calibration curves into ADC voltage codes. 137

Figure A.11: Recording evoked neural responses. Recordings through our system with a discharge time of 2 ms @ 50 μ A, two pole-shift phases of 0.5 ms @ 2200 Hz and 0.5 ms @ 700 Hz. High-pass filter setting: 200 Hz. Stimuli were positive-first biphasic pulses (pulse width 200 μ s for each phase) with an amplitude of 0.1V (bottom trace) or 0.5V (top trace). Note the recorded responses starting 4 ms after stimulation. Data collected by Johnny Nam at the University of Illinois Urbana Champaign. 138

Figure A.12: Performance of Artifact elimination technology. Recordings through our system with a discharge time of 2 ms @ 50 μ A, two pole-shift phases of 2 ms @ 2000 Hz and 0.5 ms @ 500 Hz. High-pass filter setting: 10 Hz. Acquired data were filtered by a digital 2nd order Butterworth high-pass filter with a cutoff frequency of 200 Hz. The stimuli were positive-first biphasic pulses with 200 μ s per phase, at ± 0.5 V. The circles denote additional crosstalk artifacts in the IC, the arrows show time-locked action potentials. (Note that in this figure the time axis is relative to the beginning of the stimulus.) Data collected by Johnny Nam at the University of Illinois Urbana-Champaign. 138

Figure B.1: Electrical Schematic for closed loop electroplating circuitry. The electroplating current is switched onto individual electrodes through two daisy chained, SPI-controlled, Maxim analog switches. A low amplitude (<10 mV) AC 1 khz signal is capacitively coupled onto the electrode and a reference resistor. Waveforms across these elements are amplified (INA129P) and sampled using the PIC 16F73, 8-bit analog to digital converters and transmitted serially (through RS-232) to Matlab for processing. 139

LIST OF SYMBOLS AND ABBREVIATIONS

AC	Alternating Current
ANOVA	Analysis Of Variance
APV	2-amino-5-phosphonova-leric acid
BMI	Bicuculline Methiodide
CNQX	6-cyano-7-nitroquinoxaline-2,3-dione
DBS	Deep Brain Stimulation
DC	Direct Current
DPP	Depolarizing Pre-pulse
FEM	Finite Element Modeling
FES	Functional Electrical Stimulation
GPIB	General Purpose Interface Bus
HPP	Hyperpolarizing Pre-pulse
I&Q	In-phase and Quadrature
LTP	Long Term Potentiation
MEA	Multielectrode Array
MEMS	Microelectromechanical systems
SNR	Signal-to-Noise
PBS	Phosphate Buffered Saline
PCB	Printed Circuit Board
PIC	Programmable Interface Controller
SU8	Photo Sensitive Epoxy

SUMMARY

Willfully controlling the focus of an extracellular stimulus remains a significant challenge in the development of neural prosthetics and therapeutic devices. In part, this challenge is due to the vast set of complex interactions between the electric fields induced by the microelectrodes and the complex morphologies and dynamics of the neural tissue. Overcoming such issues to produce methodologies for targeted neural stimulation requires a system that is capable of (1) delivering precise, localized stimuli—a function of the stimulating electrodes and (2) recording the locations and magnitudes of the resulting evoked responses—a function of the cell geometry and membrane dynamics. In order to improve stimulus delivery, we developed microfabrication technologies that could specify the electrode geometry and electrical properties. Specifically, we developed a closed-loop electroplating strategy to monitor and control the morphology of surface coatings during deposition, and we implemented pulse-plating techniques as a means to produce robust, resilient microelectrodes that could withstand rigorous handling and harsh environments. In order to evaluate the responses evoked by these stimulating electrodes, we developed microscopy techniques and signal processing algorithms that could automatically identify and evaluate the electrical response of each individual neuron. Finally, by applying this simultaneous stimulation and optical recording system to the study of dissociated cortical cultures in multielectrode arrays, we could evaluate the efficacy of excitatory and inhibitory waveforms. Although we found that the proximity of the electrode is a poor predictor of individual neural excitation thresholds, we have shown that it is possible to use inhibitory waveforms to globally reduce excitability in the vicinity of the electrode. Thus, the developed system was able to provide very high resolution insight into the complex set of interactions between the stimulating electrodes and populations of individual neurons.

CHAPTER 1

INTRODUCTION

Electrically interfacing cells and tissue with electrodes creates extraordinary opportunities for scientific discovery and medical advancement. For example, neural stimulators have demonstrated great promise for restoring complex sensory functions—such as vision, hearing, and bladder control—and relieving debilitating disease symptoms, like those that arise from Parkinson’s, epilepsy, and depression (Kumar 1997; Benabid 2005). Despite the multitude of applications for neural stimulators, all of these devices rely on the same basic strategy: stimulate *targeted* cells and tissue to manipulate a specific neural function. The ability to precisely target specific tissues is critical, as poorly focused or misdirected stimuli will either fail to produce the desired effect or, worse, produce an altogether unintended side-effect.

The precise targeting of extracellular stimuli, however, remains a significant challenge in neural engineering. In part, this is because the stimulus response is determined by a vast number of complex variables, including cell geometry and orientation, non-linear ion channel dynamics, electrode geometry, and extracellular voltage fields. Thus, any advances in stimulus control will require some mastery over these variables. One tool that may provide the required precision to address these variables is the multielectrode array (MEA).

The MEA, as a minimally invasive toolset with both high resolution and broad exposure to neural tissue, provides a unique opportunity to shape the extracellular voltage

fields using both multi-site and multipolar stimulation. The development of spatiotemporal stimulus waveforms with MEAs may allow researchers to use extracellular techniques to approach intracellular fidelities. Such developments would enable the exploration of contributions of individual neurons to network-wide processing; an ability that is critical to the understanding of sensory input processing, memory formation, and behavior (Potter 2001). Further, the development of selective multielectrode stimulation technology would ultimately lead to advancements in neural medical technology. This includes stimulation of any part of the nervous system to bridge neural damage, restore function, or correct aberrant activity patterns, which would create new applications for aural, vision, and epilepsy control.

In this thesis, we aim to create new tools and methodologies that enable the design and testing of multi-site microelectrode stimulation. Such an experimental platform requires the integration of novel MEMs devices, electronics, and signal processing techniques with optics, cells, and pharmacological agents. In this chapter, we review these elements as well as the current state of selective stimulation.

1.1 Multielectrode Arrays

Multielectrode arrays (MEAs) are an invaluable tool for scientific discovery and medical advancement. Because they can actively manipulate and monitor cellular activity at both the single cell and tissue level, these tools provide extraordinary insight into complex neural interactions (Morin 2005). Furthermore, because they can both elicit and suppress neural activity, they can be used in the development of medical devices for neural disorders (Wagenaar 2005). Today, MEAs are used in applications as far ranging as drug screening, bio-sensing, cardiac pacing, and epilepsy research.

1.1.1 MEA Design

The technology for MEAs consists of two components: (1) the physical MEA itself that interfaces to neural tissue, and (2) the electronics that monitor and manipulate the electrodes. The physical MEAs is made up of a grid of tightly spaced electrodes, where each electrode is capable of simultaneously monitoring the activity of a dozen or more cells. The arrangement of multiple electrodes in a grid extends the recording range across a relatively large area, providing concurrent access to both single cell and tissue-level activity. Monitoring and manipulating this activity is made possible by the electronics, which are used to impart multiple functions to each electrode. Preamplifiers allow researchers to record cells, stimulation electronics to excite the cells, and impedance monitoring circuitry to image the cells. The electronics required to achieve these sensory functions are highly specialized due to the complexity of the electrode environment. For example, the minute extracellular signals are easily concealed by noise from the electrode or electronics.

Since the introduction of MEAs 30 years ago (Gross 1977), advances in semiconductor manufacturing technology and materials research have allowed both researchers and commercial enterprises to produce a large variety of planar and 3D arrays. Today, the electrodes may be composed of metals (Haro 2002), ceramics (Weiland 2002; Meyer 2001), polymers (Abidian 2006; Cui 2002), or active transistor gates (Fromherz 2005; Merz 2005). Additionally, the electronics may be external or directly integrated into the substrate of the MEA (Najafi 1986). As a result of these technical advances, there appears to be very few limits in the design and conformation of electrode arrays.

1.1.2 MEA Applications

Given the recent proliferation of MEAs designs, applications have emerged that are critically advancing neuroscience. For example, MEAs were instrumental in the landmark discovery on spontaneous waves in the developing retina (Wong 1993). They have also been used to investigate the role of extracellular stimulation in the suppression of bursting activity (Wagenaar 2005) and in the study of novel plasticity mechanisms in cultured neural networks (Jimbo 1999). Additionally, MEAs have shown great promise for drug screening (Chiappalone 2003), safety pharmacology (Stett 2003; Meyer 2004), and biosensing (Gholmieh 2003) in a wide variety of tissue and culture preparations.

Despite advances in both the design and application of MEAs, the MEA remains a largely underutilized instrument for selective stimulation. With few exceptions (Wagenaar 2005, Jolly 1996), investigators primarily make use of only one or two electrodes simultaneously. The close proximity of dozens of microelectrodes in MEAs, however, enable coordinated multi-site and multipolar stimulus waveforms that could influence the efficacy of stimulation in two critical ways: (1) the creation of highly focused stimuli through *spatial* contouring of the extracellular voltage fields (Jolly 1996), and (2) the modulation of excitation thresholds through *temporal* manipulations of the neural membranes (Grill 1995). Thus, spatial and functional stimulus selectivity could substantially benefit by taking advantage of the full suite of microelectrodes available in MEAs.

Unfortunately, the explicit manipulation of neural networks using commercial MEAs is a difficult task that is confounded by two issues: (1) fixed electrode densities/geometries and (2) mismatches in electrode impedance. The electrode's

geometry, location, and electrical properties play a critical role in shaping the stimulus signal. Thus, efforts are required to exercise explicit control and manipulation of the stimulating electrode.

1.2 Cell Imaging

The use of MEAs, or any instrument, to develop selective stimulus waveforms requires some means to evaluate the efficacy of the stimulus. One technique is to use the stimulating electrode to electrically measure the evoked activity as well. This approach, however, suffers from two shortcomings: (1) the stimulation artifact induced by a post-stimulus charge imbalance blinds the observer to the immediate cellular response (Brown 2008; Blum 2007; Jimbo 2003), and (2) the recording electrode only resolves a few neurons at a time and cannot identify the location of those neurons (Gozani 1994; Thakur 2007). An alternative is to use optical imaging, which provides tremendous spatial resolution for cell localization and allows for the simultaneous monitoring of every cell within the network (Cossart 2003; Göbel 2007). In this section, we present microscopy technology for static and functional imaging as well as signal processing techniques to extract data from the acquired images.

1.2.1 Static Fluorescence Imaging

Fluorescence microscopy makes use of the fact that certain materials, when irradiated with light of a specific frequency, will emit energy as visible light that can be filtered and captured. In biology, fluorescent dyes can be manufactured to bind to cells in very specific ways, which results in a high contrast label that illuminates only the elements of interest. Dye labeling in conjunction with sophisticated microscopes can generate high-

resolution images with higher contrast and more information than could be generated with traditional optical microscopy (Stosiek 2003; Yuste 2005). For example, confocal microscopy produces three dimensional optical recordings of fluorescently labeled neurons. The 3D image, reconstructed from a cascade of 2D optical slices, is made possible by the confocal principle, in which emitted light outside of the 2D confocal plane is eliminated (Belien 2002). When applied to studies of neural cultures, such techniques generate images of extraordinary detail and clarity.

An important measure of stimulus-evoked activity, however, is not only the location of the cells but also the active response of the cells. Although static imaging can identify the location of the cell with respect to the stimulating electrode, it cannot provide a measure of the cells activity. For dynamically monitoring the cellular response, functional imaging is required.

1.2.2 Functional Fluorescence Imaging

There are many techniques for optically monitoring cellular activity. Among them, fluorometric Ca^{2+} imaging is a sensitive method for monitoring neural activity that makes use of the fact that, in living cells, most depolarizing electrical signals are associated with Ca^{2+} influx (Stosiek 2003). There are several properties of Ca^{2+} signaling that make it particularly useful for studying the evoked responses of stimulated neurons: (1) Ca^{2+} signals are often amplified by the intracellular release of Ca^{2+} stores (Tsien 1990, Berridge 2000), (2) the slow time constants of Ca^{2+} signaling enable further signal boosting through Ca^{2+} accumulation, (3) the slow time constants accommodate the relatively slow acquisition speeds of imaging systems, and (4) individual action potentials (up to 100 hz) can be discerned from the calcium waveforms (Yuste 2005).

There are several calcium indicators whose fluorescence changes significantly (several percent of the resting fluorescence level, or $\Delta F/F$) as intracellular calcium concentration changes due to neural activity. The acetoxymethyl (AM) esters of these are cell permeant, allowing them to become concentrated in living neurons where they are trapped by the action of esterases. Optimized protocols for bulk loading of AM Ca-indicators into neural tissue (Stosiek 2003; Yuste 2005) allow the simultaneous imaging of calcium transients in hundreds of neurons (Cossart 2003; Göbel 2007). At present, there are very few studies that combine functional imaging with MEA recording (Wong 1998; Jimbo 1993; Robinson 1993). One challenge that may limit the coupling of these two technologies is that sophisticated signal processing techniques must be put into place to acquire and manage the massive and highly-complex data that results.

1.2.3 Image Processing

In order to rapidly extract meaningful data from images acquired through microscopy, some signal processing algorithms must be put into place. In particular, automated *segmentation* algorithms provide a means for high throughput mapping of complex morphological and functional interactions. Although many segmentation routines can accurately quantify nuclear (i.e., spherical) labeling in 2-D or 3-D, nuclear stains alone are inherently limiting as they omit information pertaining to such important measures as cell morphology, neurite outgrowth, and cell-cell interactions (e.g. receptor-mediated or synaptic). Therefore, there is a need for segmentation algorithms that can identify cellular features from images acquired using whole-cell staining techniques.

When labeling whole-cell stained neuronal somata, commercial software is error-prone in the quantification of 2-D neural images as large caliber processes are routinely

counted as cells. Furthermore, commercial systems fall into one of two different camps: (1) user-driven systems (e.g. Neurolucida), which have excellent reconstruction capabilities, but are extremely time-consuming, or (2) completely automated systems, (e.g. ImageJ routines, Image Pro Plus), which may be fast, but offer little user control and are inaccurate given irregular (e.g., non-spherical), process-bearing neural cell morphologies. Likewise, neural-specific image processing techniques presented in the literature tend to be along one of two different applications: (1) cell population characterization, in which the algorithms segment *nuclei* of medium to high density neural constructs (Chawla 2004; Sarti 2000; Solorzano 1999), or (2) single cell (or low density) reconstruction, with highly detailed traces of individual cell processes (Al-Kofahi 2003; Koh 2002; Meijering 2004; Zhang 2007, Wearne 2005).

In light of the shortcomings for current image processing techniques, it would be of significant benefit to develop algorithms that bridge this gap to offer researchers tunable, automated image analysis techniques with user-controlled corrections that are optimized to deal with issues specific to functional and spatial analysis of 2-D and 3-D neural systems. This is especially true in the context of quantifying stimulus-evoked activity in functional images, as experimental inquiries will easily generate *hundreds of thousands* of complex neural images. The ability to quantify and track the evoked activity of individual cells to extracellular stimuli is critical for the development of selective stimulus waveforms and therapeutic medical devices.

1.3 Selective Stimulation

The use of electricity for therapeutic benefit has been explored extensively over the past century. From electroconvulsive therapy (i.e shock therapy) to cochlear implants, the

medical field has applied extracellular stimulus strategies to restore human function (e.g. vision and bladder control) or relieve neurological disease and injury symptoms (e.g. spinal cord injury or epilepsy). Despite the tremendous advances that have been made with stimulus therapies, the exact mechanisms for therapeutic benefits are poorly understood. Further, present day deep brain stimulators (DBS) use large ‘paddle’ electrodes to blindly flood brain tissue with open-loop, high-frequency stimulation. Today, much research is underway to develop more intelligent therapeutic stimulation devices as well as to understand the mechanisms of extracellular stimulation and the functional benefits and consequences of its use. The goal of our research is to enable the exploration of these mechanisms, providing an avenue for the development of spatially targeted stimulation.

1.3.1 Limitations in Spatiotemporal Stimulation

Selective stimulation requires spatial and temporal coordination of voltage fields in conductive cellular media. Some control over the *spatial* contour of the fields is afforded by the shape of the current-induced voltage fields, where the spatial decay of the field is given by the resistivity of the solution, ρ , and the electrode shape and material (McIntyre 2001). Unfortunately, *temporal* control over the *propagation* of signals in cellular media is virtually impossible to achieve. While the mobility of ions in conductive neural media is 6 to 7 orders of magnitude slower than charge carriers in silicon (Kovacs 1994), velocity is related to the square root of mobility. Accordingly, the speed of propagation in conductive media is in the gigahertz range; thus, with respect to cellular time scales, the distribution of an applied stimulus is instantaneous everywhere in the dish. However, the response times of neural membranes and ion channels introduces a

time-sensitive component in a scale that is easily achieved by electronics. Therefore, while it is not feasible to temporally sum signals at the neuron, the temporal component of voltage fields in the dish are still very relevant.

1.3.2 Temporal Manipulations

The sodium channel plays a critical role in determining the neural response to extracellular voltage fields (Grill 1995). By taking advantage of the time course of the inactivation gate in the sodium channel, Grill and Mortimer demonstrated that one could shape the stimulus with a hyperpolarizing pre pulse (HPP) or depolarizing pre pulse (DPP) to excite or inhibit stimulation respectively. McIntyre and Grill used this phenomena in modeling studies to develop waveforms that selectively activated cell bodies over fibers (and vice versa) (McIntyre 2000). This modeling study also demonstrated the robustness of selectivity over a broad range of neural modeling parameters; selectivity showed the greatest dependency on the distribution of sodium ion channels.

1.3.3 Spatial Manipulations

Recent work relates the influence of the physical properties of the electrode (shape, material, surface roughness, etc.) to the formulation of electric fields in neural tissue. McIntyre and Grill have shown that more uniform current densities are attained with larger and relatively blunt 3D electrode tips; additionally they demonstrated that 3D electrode tips behave identically to theoretical point source electrodes within 50 μm of the electrode (McIntyre 2001). This finding, coupled with studies that demonstrate that the electrical characteristics of the medium are unaffected by the presence of neurons

(Rattay 1999), holds promise for using simple point source models to elucidate strategies for extracellular stimulation. As a result, it may be possible to use computationally inexpensive algorithms, and even closed form expressions, to determine the affects of applied fields on neural responses (Plonsey 1989).

Field steering, the art of spatially manipulating voltage fields, has been investigated by research groups in the functional electrical stimulation (FES), retina prosthesis, and cochlear implant communities. In the retina community, Hornig and Eckmiller used finite element models (FEMs) to demonstrate that control of the maximum voltage field increases with the orthogonal distance to the electrode (z-direction) (Hornig 2001). Hornig modeled layers of retina neurons and used a training algorithm to selectively stimulate individual model cells distal to a flat simulating grid. With this approach, Hornig was able to discriminate between two adjacent model cells: one cell was set into a sub-threshold refractory period while the other was stimulated. In the FES community, Veraart et. al, have shown that subtle variations in the transverse and longitudinal currents of a tri-polar nerve-cuff electrode can be used to tune the output force of a *selectively* activated muscle (Veraart 1993). Thus, field steering allows FES investigators to take advantage of the fascicular organization of the nerve to somewhat selectively activate and tune the force output of a targeted muscle.

In the cochlear implant community, Spelman and others have provided a solid foundation for field steering in one dimension. Jolly has shown with modeling and with experiments performed in saline and guinea pig cochleas that a quadrupolar electrode configuration provides much greater focus than bipolar and monopolar configurations (Jolly 1996). Rodenhiser et al. have presented a simple method for determining the drive

currents necessary to produce focused stimuli (Rodenhiser 1995), by first creating a matrix of complex transfer impedances that relate output voltages to input currents and then using a least squares technique to solve for the currents necessary to generate the desired voltage pattern.

1.4 An Experimental Platform for Selective Stimulation

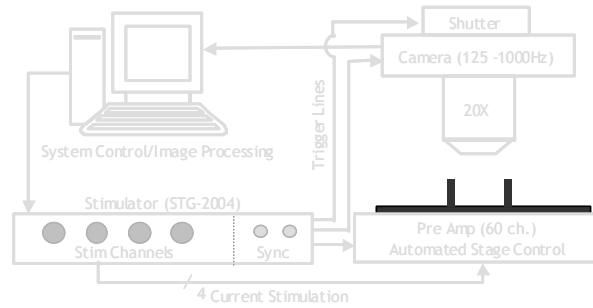
Among the many challenges in designing spatially and functionally selective stimulus waveforms, is the inability to *experimentally* validate stimulation strategies. In fact, the most recent advances in stimulation technology have been made with computational *models*, which—despite providing a great deal of insight into the mechanisms, techniques, and strategies for selective stimulus waveforms (Grill 1995; McIntyre 2000; Rattay 1999; Greenberg 1999; Hornig 2001)—are seldom experimentally validated. Thus, it would be beneficial to develop an experimental system that approaches the throughput (and insight) of these models.

The design and testing of stimulus protocols using both multi-polar field shaping and temporal ion-channel manipulation requires an experimental platform that can (1) deliver arbitrary current waveforms to multiple electrodes and (2) monitor the cellular activity of every neuron within a specified area. Combining an optical imaging system with multielectrode arrays (MEAs) creates an ideal platform for tracking neural responses to extracellular stimuli. Specifically, optical imaging systems can record individual action potentials by measuring the changes in internal concentrations of calcium in somata using Ca^{2+} -sensitive dyes (Smetters 1999). Additionally, the tightly spaced grid of electrodes in MEAs can be simultaneously activated to sculpt the contours of voltage fields that surround neural tissue.

In this thesis we build an automated, high-throughput stimulus tracking system. The goal of this work is to create a flexible system that can address many of the issues critical to the study of structured neural stimulation, such as the MEA electrodes, stimulating waveforms, and stimulus-evoked responses. In chapter 2, we present microfabrication technologies for arbitrarily specifying the geometry, packing density, and electrical properties of MEA microelectrodes. In chapter 3, we present automated signal processing techniques for statically and dynamically tracking optical neural data. In chapter 4, we combine the engineering tools of chapters 2 and 3 with novel signal processing techniques to enable the high-throughput evaluation of selective stimulation waveforms. Finally, in chapter 5, we discuss the advantages and shortcomings of the developed technology and outline the future directions necessary for exercising electrical mastery over neural tissue.

CHAPTER 2

MICROELECTRODE TECHNOLOGIES: INTERFACING NEURAL CELLS



The multipolar stimulation of cells and tissue requires specialized interfacing devices to garner control over the neural environment. Multielectrode arrays (MEAs) have emerged as a leading technology for extracellular, electrophysiological investigations of neuronal networks. Unfortunately, the explicit manipulation of neural networks using commercial MEAs is a difficult task that is confounded by two issues: (1) fixed electrode densities/geometries and (2) mismatches in electrode impedance. The electrode's geometry, location, and electrical properties play a critical role in shaping the stimulus signal. In this chapter, we present two novel electrode fabrication technologies to produce electrode arrays with customized geometries and high channel counts/densities. Additionally, we present a closed loop electroplating approach to precisely regulate the electrical properties of the microelectrodes. Taken together, these advances in fabrication enable the development of highly controlled neural interfaces with the potential for spatially controlled stimulation.

2.1 Microfabrication of MEAs

There are several ways in which the MEA design influences the efficacy of stimulation, including electrode size, location, and density. Apart from charge density constraints, a smaller electrode enables a more localized region of influence (e.g. consider the spatial selectivity of a ‘dish-sized’ electrode versus a ‘cell-sized’ electrode.) Likewise, the location of the electrode with respect the region of interest greatly influences how likely an applied stimulus reaches its target. Finally, the electrode count and density not only determines how much coverage is provided, but also how much control can be exerted over the dish-wide voltage fields. For example, electrodes which are simultaneously stimulated but are far apart will appear as a grid of monopoles; in contrast, electrodes which are close together, will generate complex voltage field patterns.

Modern microfabrication technologies make it relatively straightforward to produce electrodes of virtually any size, density, and conformation. However, apart from material and cytocompatibility issues, one of the most significant challenges in MEA fabrication arises from the difficulties incurred in connecting micron-sized electrodes to millimeter-sized sockets and pads (i.e., the ‘packaging problem’). This problem is exacerbated when the electrode count and density are increased to improve spatial selectivity. Unfortunately, brute-force packaging techniques (e.g. conductive epoxies or manual pin/wire placement) are time and cost prohibitive, making it difficult to generate the number of samples needed for stimulation experiments. In this section, we present two scalable fabrication technologies that address a critical problem in customizing electrode size/placement and increasing electrode density: (1) Glass MEAs with integrated electronics, and (2) Kapton MEAs on manufactured substrates

2.1.1 Glass MEAs with Integrated Electronics

The difficulty in achieving high-density, high-count electrodes is in routing the electrodes to the stimulating and recording electronics. The problem is in the relative differences in scale; interfacing sockets and pads are in the millimeter range, while the electrodes are in the micron-range. One approach to solving this problem is to avoid temporary socketing altogether, by permanently affixing the electronics directly onto the MEA substrate.

There are several technologies for this approach, including wire bonding, which enables sub-millimeter interconnects, and bump-bonding, which enables deep sub-millimeter connections. In this study, we elected to explore the feasibility of direct electronics integration using the more widely accessible wire-bonding technology.

The fabrication of the glass MEAs employed two masks and used conventional surface micromachining technology. To prepare the substrate, a 49×49 mm sheet of Pyrex glass (Esco Products, Oak Ridge, NJ) was cleaned by sequentially rinsing the glass in trichloroethylene, acetone, methanol and de-ionized water. Next, 6–8 μm of negative photoresist (NR9-8000) was applied by spin coating; the resist was exposed through a positive image mask of the wiring traces with a UV mask aligner (Karl Suss MA-6). During this process, care was taken to ensure that the sample was slightly overexposed such that, after postbake and development, the slope of the resist profile would facilitate metal liftoff. After development, 300° Å of Ti was deposited followed by 2500 °Å of Au (Figure 2.1A). E-beam evaporation was the preferred method of metal deposition, as the perpendicular orientation of the metal with respect to the planar MEA facilitated metal lift-off in the next step. Following deposition, the device was submerged in acetone to lift-off portions of the metal layer that corresponded to the negative image of the mask

(Figure 2.1B). Next, 3.2 μm of SU8-5 was spun on to form the insulation layer for the wiring traces and the electroplating mold (profilometer data not shown). To define the electrode vias and contact pad openings, the SU-8 was UV exposed through a positive image mask and developed (Figure 2.1C). The sample was then flood exposed to UV light to ensure maximal photopolymer crosslinkage and to facilitate removal of toxic solvents during the curing process.

Following development, the MEA was post-processed to prepare the instrument for cellular studies. The electrode vias were electroplated with platinum black to form the electrodes (Figure 2.1D). Following electrode formation, the custom ICs were wire bonded onto the glass substrate (Figure 2.1E) and encapsulated in Sylgard 184 (Dow Corning, Midland, MI). (Figure 2.1F) The MEA was then cured in an oven at 90°C for 24 h. Subsequently, the device was submerged in de-ionized water for at least 48 h in order to rid the cell-contacting surfaces of any toxic residue from the manufacturing process. Lastly, custom-cut polycarbonate rings were attached to the MEA surface using Sylgard 184 and served as cell culture containment (Fig 2.1I). The thick SU-8 insulator (3.4 dielectric constant), coupled with the low impedance of the platinum electrodes (20 K Ω at 1 khz), improved the signal to noise ratio of the device (as compared with MEAs with 0.5 μm of high dielectric SiN insulator and 100 K Ω impedances). Specifically, the coupling capacitance between the wiring traces and cell media as well as the thermal noise of the electrodes was reduced. Prior to cell seeding, the MEAs were rinsed with de-ionized water for an additional 24 h, briefly rinsed with 70% ethanol and allowed to dry in a sterile environment. The MEAs were then briefly flamed or plasma treated and allowed to return to room temperature. Figure 2.1G shows the completed system.

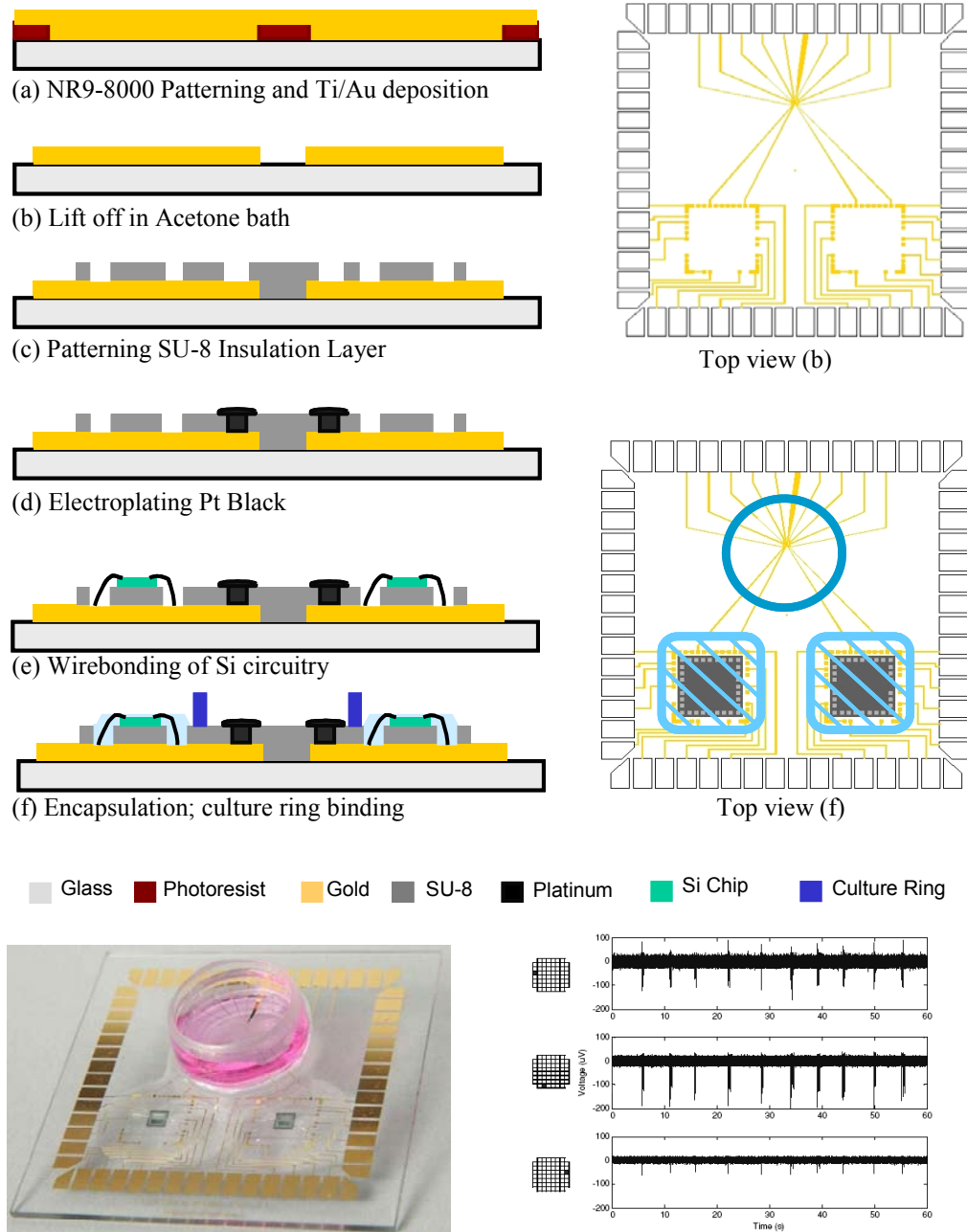


Figure 2.1: Fabrication and testing of glass MEAs. (A-F) Custom microfabrication steps for producing MEAs with electronics designed by (Harrison 2003) directly integrated onto the substrate. This integration strategy enables high channel count MEAs by shrinking the spring-pin pad sizes (2x3 mm) to wire-bond pad sizes (100 x 100 μm). Note the differences in scale between the wire-bonding pads (surrounding the chip) and the spring-pin pads (surrounding the MEA). Integrated circuits with on-board analog or digital multiplexers would significantly reduce the amount of output pins required to interface the device. (G) Photograph of the completed MEA. (H) Recordings performed on the MEA (note: shown signals were not routed through the wire-bonded chip; sample signals from the chip may be found in (Blum 2003)).

The MEAs were designed so that signals could be routed simultaneously to both the integrated ICs as well as to a pad layout that was compatible with Multichannel Systems pre-amplifier. To test the system, primary cortical cells were cultured onto the MEAs (density = $1.25\text{--}2.0 \times 10^5$ cells/cm²) using Neurobasal medium (Prado 2005). This culture method resulted in 90–95% neurons (confirmed by immunostaining for tau-5, a neuronal-specific cytoskeletal marker), with the remaining cells exhibiting morphological characteristics of glial cells (verified by glial fibrillary acidic protein immunostaining.) Figure. 2.1H shows biological activity recorded with this system at 10 days in-vitro (DIV).

2.1.2 Kapton MEAs on Manufactured Substrates

In the previous section, we demonstrated an approach to increasing the channel count by directly integrating electronics onto the MEA substrate. While this technique is effective, it presents a number of disadvantages: (1) unless bottom-side integration is employed, which requires vias through the substrate, the MEA substrate area is large, and (2) unless the chips are made in very large volumes, the chips required to service semi-disposable MEAs are very expensive. An alternative approach is to process the MEAs directly onto bulk-manufacturable substrates. In this section, we explore the feasibility of fabricating the MEAs directly onto the package itself—printed circuit boards.

Printed circuit boards (PCB), flex circuits, and flex-rigid kapton (a hybrid of flex circuits and PCBs) are commercially manufactured multi-layer epoxy/metal substrates. Multi-layer PCBs have been used in the electronics industry for decades and can typically produce wiring traces with a resolution of approximately 200 μm . Flex circuits, which use polyimide or kapton as the layering structure, are a more recent addition to the

industry and have an improved feature resolution, approx 50-80 μm . Besides their role in the consumer electronics market, flex circuits are becoming increasingly common in the medical industry with products such as thermofilm heaters and inductive coils. Flex-rigid substrates combine the advantages of rigid PCBs with flex circuits by adding a rigid supporting frame to the flexible and high-resolution kapton layer. The advantages of these processes are: (1) cost-effectiveness, (2) vias for backside electrical connection, and (3), in the case of flex circuits, biocompatibility (Giovannardi 2006), and (4) substrate transparency (for thin kapton). The major problem in performing post-processing on these substrates is surface non-uniformities but approaches reported in literature like (Ghodsian 2005) can be used to overcome this problem.

Unfortunately, cytocompatibility can be a difficult challenge for fabrication processes that commonly involve very cytotoxic chemicals. Commercial PCB fabrication incorporates epoxies, copper, tin, lead (or silver) into the final product, as well as a variety of other chemicals that are not amenable to cellular life. This necessitates that any possible toxic materials be encapsulated from the cellular cultures. Additionally, microfabrication on PCB substrates imposes its own set of requirements: (1) a reduction in the surface roughness of the PCB and its surface metal layers (i.e., surface planarization), (2) interfacing to the relatively thick low-resolution top metal layer, and (3) MEMS processes that are low temperature compatible (lower than 220°C).

We addressed the challenges of post-processing on PCB substrates with the following fabrication process: A custom-designed flex-rigid kapton board, containing the necessary wire traces, was fabricated through a commercial vendor (Cirrex). An open area of the board was reserved for MEA post-processing. The MEA traces and recording

sites were defined using NR9-8000 (which also accounted for the planarization of the metal on the flex circuit) and UV lithography. A biocompatible metal stack (titanium for adhesion and gold for the electrode) was deposited using e-beam evaporation and the metal was lifted off to define the finer metal lines. In order to passivate the MEA and define the recording sites we used a thin layer of photo-patterned SU-8. This process is depicted schematically in Figure 2.2.

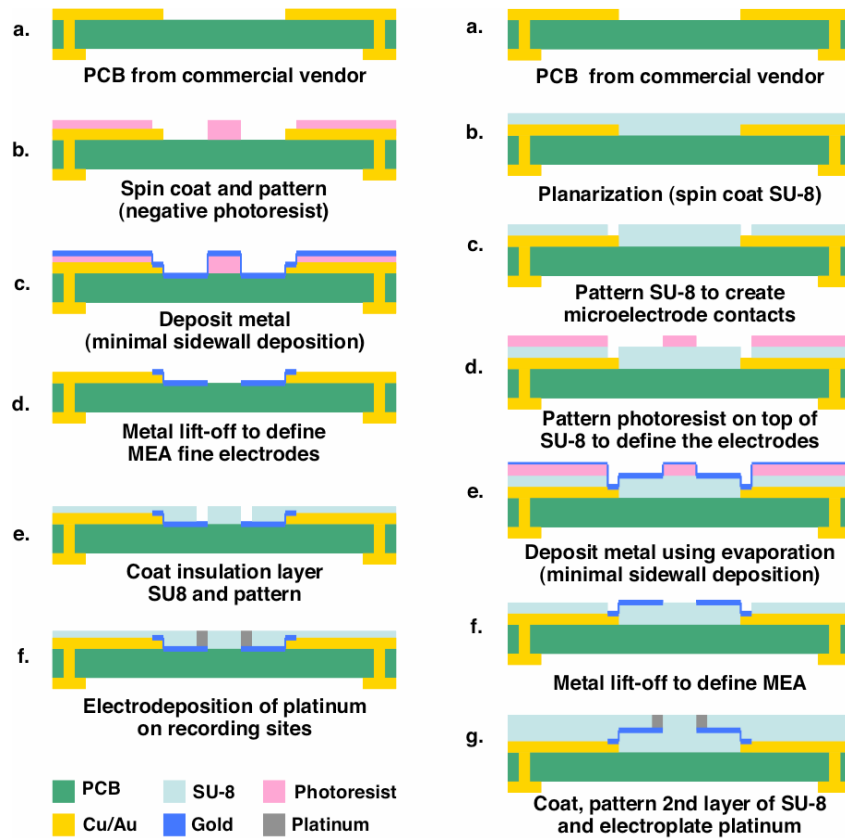


Figure 2.2: Fabrication process for post-processing on manufactured PCB substrates. (Left) The minimum required processing steps for high channel count MEAs on interconnecting substrates. Note that PCB vias enable simple back side connections to the MEAs. (Right) An alternative strategy that enables multi-layer wiring for higher-density electrode configurations and also provides additional encapsulation from cytotoxic materials. NR9-8000 is represented by the pink photoresist.

The kapton arrays were developed using the single, SU-8 layer process (in collaboration with Mr. Swami Rajaraman.) We tested the functional viability of this process by measuring the impedance of the electrodes and the surface irregularities of the insulation layer. Figure 2.3 illustrates electrically viable MEA units. The combination of inexpensive manufactured printed kapton circuit boards and post-processed microelectrodes present the opportunity to scale MEA technology from 1 well per sample to a multiwell format containing dozens of such MEAs.

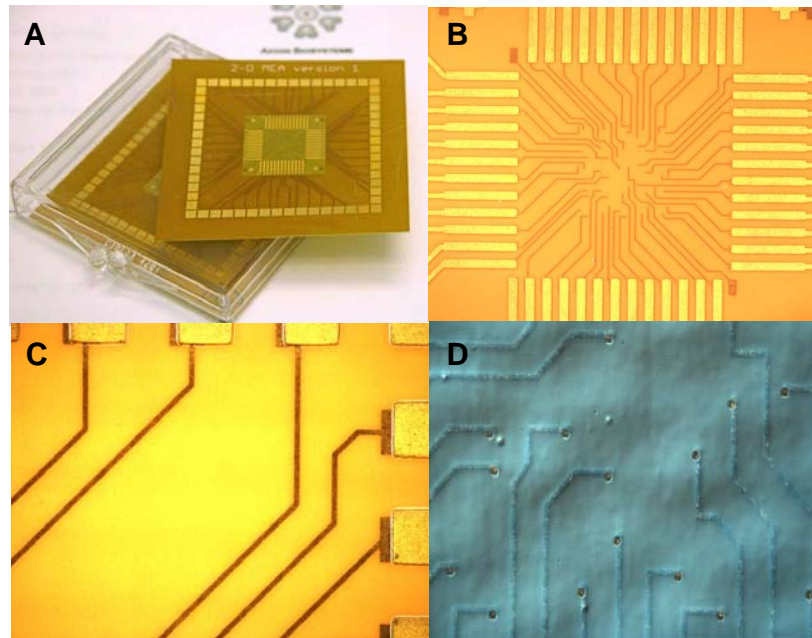


Figure 2.3: Post-processing of PCB substrates for the development of test MEAs. (Two layer method outlined in Sec. 4.2.2.) (A) Custom Kapton FlexBoard™ PCB substrates with patterned wiring traces and microelectrodes. (B) Close-up of the micro-electrode area of a processed substrate. (C) Micro-photograph of the area in which the microfabricated traces contact the PCB traces (gold traces in the PCB are 25 μm thick 200 μm wide, microfabricated traces are 0.5 μm thick 30 μm wide). (D) Differential interference contrast microphotograph focused on the SU-8 top surface in a section of the electrode area. Lighter and darker areas are a result of constructive and destructive light interference; this highlights surface features in the sub-micron scale. The planarizing effect of thin (3.4 μm) SU-8 smooths the surface roughness of the PCB from its original 5 μm variations down < 200 nm variations (profilometer data not shown). Impedance measurements show that the gold electrodes are viable with a mean impedance magnitude of 191 K Ω at 1 KHz.

2.1.3 Design Tradeoffs: Choosing a Process

In section (2.1), we demonstrated two novel microfabrication schemes to explicitly specify the location and size of the electrodes as well as the density and channel count. Each strategy presents its own set of advantages, and the choice of strategy depends entirely upon the design constraints and the intended application. For applications that involve thousands of stimulation channels in a disposable platform, the kapton approach (2.1.2) may be preferred. For applications that require longer-term interfacing or close proximity of the electronics to the electrodes, the glass MEA approach (2.1.1) may be favored. Ultimately, both approaches provide reliable methods to addressing several critical variables for stimulating interfaces: electrode size, location, and, perhaps most importantly, density and count.

2.2 Electrode Conditioning

In addition to geometry and location, the electrodes' electrical properties play a critical role in influencing cellular excitation. For example, in common ground stimulation schemes, the impedances of the grounded electrodes explicitly shape the voltage fields that are applied to the neural tissue. Additionally, for voltage stimulation applications, it is not possible to model current densities and voltage fields without explicit knowledge of the electrode impedance (Jolly 1996). Likewise, for current stimulation applications, it is difficult to predict the electrode safety limits without measuring the electrode impedance (Wagenaar 2004). Furthermore, studies have shown that removal of stimulation artifacts is highly sensitive to the electrode properties (Brown 2008; Bakkum 2007). Therefore, it is beneficial to not only measure the electrical properties of the electrode but also to specify these properties.

The need for low impedances must be balanced against other design tradeoffs. One method to reduce the electrode impedance is by increasing its cross-sectional or base area. Unfortunately, as a larger electrode makes contact with a larger section of the media, this choice reduces the electrode specificity. That is, once the electrode exceeds the dimensions of the cells under study, further increases in size will attenuate individual cell signals by averaging a larger portion of tissue activity up to a point that it becomes impossible to observe individual cell signals. This link between electrode impedance and size has produced the common misconception that a low impedance electrode cannot be as specific as high impedance electrode. If increasing electrode base-area was the only means to reduce impedance this would be true; however, modification to the electrode surface roughness or material can reduce electrode impedance by increasing the surface area without modifying the physical dimensions.

Given the very small sizes of electrodes required for electrophysiological experiments, even when electrode shape, dimension, and materials are constrained, fabrication tolerances and imperfections will generate electrodes with large variability. In particular, platinum black is notorious for producing electrodes with highly variable impedances (Franks 2005). For arrays of electrodes such variability is very undesirable, as it introduces a source of randomness into the experiment that is a product of the instrumentation itself, and not of the tissue under study. For recording applications, equalizing the noise across electrodes will make the effective range of the electrodes similar to one another. For stimulation applications, electrodes that are well matched and specified will enable consistent voltage-controlled stimulation as well as known safety limits for current-controlled stimulation. Finally, removal of stimulation artifacts is

strongly dependent on electrode characteristics (Brown 2007; Bakkum 2007), which requires specialized or adaptive protocols for each individual electrode. Thus, it is desirable to provide a means to specify electrode impedances and to precisely match these with high precision.

We developed an automated, closed-loop, electroplating approach that monitors and controls the morphology of surface coatings, such as platinum black, during deposition. This process ensures that all electrodes have specified and matched electrical properties, and it is applicable to a broad range of materials, including metals and conductive biopolymers. Electrode uniformity is achieved by measuring electrode impedance simultaneously during the electroplating process. In addition to automated impedance control, we implemented pulse-plating as a means to produce very robust, resilient low-impedance electrodes that can withstand rigorous handling and harsh environments.

2.2.1 Linear Electrode Models

The material and physical properties of the electrode shape the electrical signals presented to the cellular media and have a profound influence on the stimulation and recording of neural tissue. Thus, explicit shaping of the microelectrode impedance spectrum requires an understanding of how the physical parameters of the system (electrode material, cross-sectional area, etc.) relate to the electrical properties of the electrode. In this section, we use basic electrode theory to illustrate both the opportunity and limitations for precise manipulation of the microelectrode impedance spectrum.

Over the past century, the electrode-electrolyte interface has been extensively studied; present day models can account for many of the non-linear dependencies on the

electrode's electrical and geometrical properties (Borkholder 1998, Kovacs 1994).

Remarkably, most of the complex behavior of electrodes can be described with a simple lumped circuit (Figure 2.4A): an *interface capacitance*, C_I , shunted by a *charge transfer resistance*, R_T , in series with a *spreading resistance*, R_S . Each of these circuit elements have been uniquely ascribed to physical electrochemical processes and electrode geometry, which are described briefly below. (*Note: Please see Appendix A for a discussion on non-linear electrode theory and its application to stimulation artifact modeling*).

A metal electrode in an ionically conducting solution generates chemical reactions that induce a field at the electrode-electrolyte interface (Kovacs 1994). This electric field, generated by electron-transfer reactions, produces the *hydration sheath*, in which water dipoles orient themselves at the metal surface. Solvated ions accumulate just beyond the hydration sheath, forming what is known as the *outer Helmholtz plane* (OHP). In turn, the charges at the metal layer and ions at the OHP form the *Helmholtz capacitance*, which is given by:

$$C_H = \frac{\epsilon_o \epsilon_r}{d_{OHP}} A_S, \quad (2.1)$$

where d_{OHP} is the distance from the OHP to the metal electrode, ϵ_r is the relative permittivity of the electrolyte, ϵ_o is the permittivity of free space, and A_S is the surface area. In addition to the bound ions at the OHP, it has been shown experimentally that capacity at the interface also depends on voltage (Borkholder 1998). The Gouy-Chapman capacitance model, which accounts for this dependency by considering the electrical and thermal effects on the time-averaged ionic distribution (Borkholder 1998), can be added

in series with the Helmholtz capacitance to form the full *interfacial capacitance*, C_I . For our application, the representative equation for the Helmholtz capacitance will sufficiently characterize the interfacial capacitance as it adequately captures the dominating electrode behavior.

In addition to the interfacial capacitance, a parallel resistive element is modeled to account for the current that flows across the electrode with the application of a DC voltage. This resistance is primarily given by the *charge transfer resistance*:

$$R_T = \frac{V_t}{z J_o} \quad (2.2)$$

where J_o is the exchange current density, z is the valence of the ion involved in the charge transfer reaction, and V_t is the thermal voltage (~ 26 mV). The exchange current density, J_o , is a function the surface area, A_s , of the electrode as well as the electrode material, electrolyte composition, and electrochemical potential.

Finally, to account for the spreading of current from the localized electrode to a distant ground electrode in the solution, the spreading resistance is added in series to the above circuit elements (Kovacs 1994):

$$R_S = \frac{\rho\sqrt{\pi}}{4\sqrt{A_B}}, \quad (2.3)$$

where A_B is the base area (or drawn area) for a circular electrode, and ρ is media resistivity. It is important to note the distinction between the *base area*, A_B , which is given by the cross sectional area of the electrode (or the drawn area of a 3-D electrode), and *surface area*, A_s , which, though related to the base area, may be independently adjusted by modifications to the texture and surface features of the electrode.

Equivalent circuit models, tuned to match experimental microelectrode data, provide an excellent fit. Specifically, Franks et. al have demonstrated that simple models (which employ a constant phase element for the interfacial capacitance), can capture the full impedance spectrum, including the phase behavior, with remarkable precision (Franks 2005). Here, in Fig. 2.4B, the Nelder-Mead regression was used to fit the model of Figure. 2.4A to the measured impedance magnitude of a 10 μm Au electrode in physiologic saline, showing that the simple lumped circuit model very accurately captures the impedance magnitude.

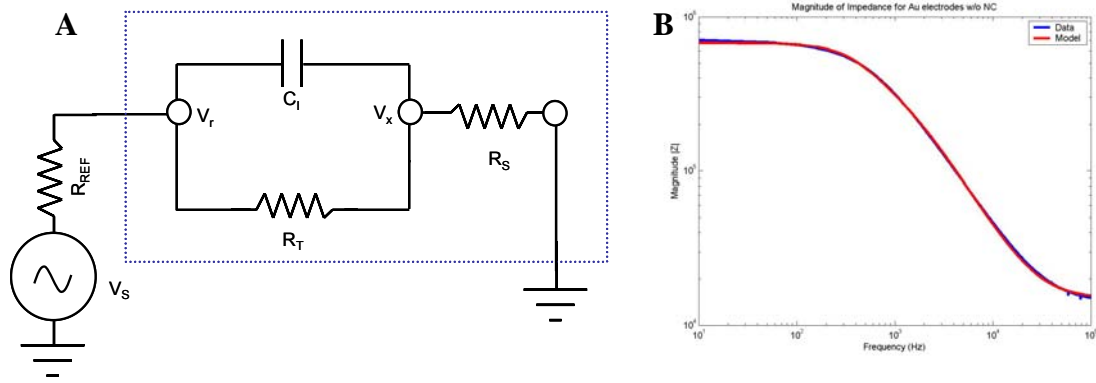


Figure 2.4: Electrode Modeling. (A) The impedance magnitude of microelectrodes is represented by an interface capacitance, C_i , shunted by a charge transfer resistance, R_T , in series with the spreading resistance, R_s . (B) Demonstration of model accuracy: The model in (A) was tuned to match the impedance magnitude of a 10 μm diameter Au electrode using a multidimensional unconstrained nonlinear minimization method (i.e. the Nelder-Mead method).

2.2.2 Impedance Manipulations

From the electrode model it becomes apparent that, with systematic design choices and novel processing techniques, it is possible to shape the impedance spectrum of an electrode. For example, the capacitance, C_i , is determined by the surface area of the electrode, which may be tuned by varying the plating density in electroplating processes (de Haro et al., 2002) or the gas concentrations in sputtering systems (Janders et al.,

1997). The charge transfer resistance, R_T , is affected by both the electrode material and surface area, and the spreading resistance, R_S , is a function of the base area (or drawn area) of the electrode. As shown in Table 2.1, by specifically targeting physical parameters (identified as control mechanisms), one can explicitly manipulate the impedance properties of microelectrodes. Figure 2.5 illustrates an example of such impedance sculpting for various elements of the electrode model.

Table 2.1: Reference table for electrode shaping

Element	Control Mechanism	Imp. Region	Equation	Fig. Value*
R_T	Electrode Material (J_o) & Surface Area (A_s)	Low-band	$R_T = \frac{V_t}{zJ_o/A}$	150 M Ω
C_H	Surface Area (A_s)	Mid-band	$C_H = \frac{\epsilon_o \epsilon_r}{d_{OHP}} A_s$	300 pf
R_S	Base Area (A_b)	High-band	$R_S = \frac{\rho \ln(4)}{\pi A_B}$	10 K Ω

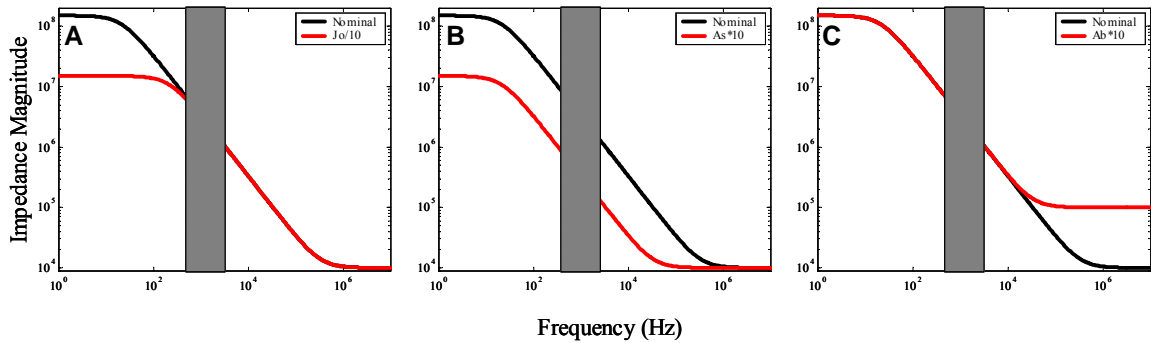


Figure 2.5: Shaping the impedance spectrum of modeled microelectrodes. By careful manipulation of the electrode's physical elements—electrode material, base area, and surface area—one can control individual model parameters (Gray band indicates the area of interest for recording neural action potentials). (A) Changes in the electrode material or electrolyte composition, J_o , modifies the charge transfer resistance and the impedance magnitude at low frequencies. (B) Likewise, changes in the electrode surface area, A_s , modify both the charge transfer resistance and interfacial capacitance to alter low- and mid-band impedances. (C) Finally, changes in the base area, A_B , of the electrode directly influence the spreading resistance or impedance magnitude at high frequencies.

2.2.3 Closed-Loop Electrode Deposition

The frequency range of interest for recording neural activity centers around the spectral components of action potentials (for non field-potential applications). In this mid-band range (approx. 1Khz, the de facto standard for extracellular electrophysiology), the electrode impedance is most sensitive to the structure and volume of deposited materials. However, despite excellent control afforded by modern deposition technologies (e.g., sputtering systems and chemical vapor deposition), electrodes inevitably have tremendous variability in their impedance spectrum (platinum black electrodes have been reported to vary over 600%; Franks 2005). One method to reduce such variability would involve the use feedback mechanisms to regulate and control the physical parameters of the electrode during microfabrication. Because of the ready availability of electrical data during deposition, electroplating potentially provides the most direct mechanisms for real-time measurement and control during the deposition process.

2.2.3.1 Electroplating Feedback Strategies

Although electroplating provides an avenue for explicit electrode shaping, it is not without its complications, and the potential for adhesion problems with materials such as platinum black has been widely reported (Borkholder 1998). To address problems associated with electrode degradation, well characterized electroplating recipes have been documented that include adhesion promoting ingredients and optimized current densities (Gesteland 1959). Additionally, ultrasonic agitation applied during the plating process has been shown to insure long-lasting adhesion (Gesteland 1959). Although *pulsed plating*, which applies electroplating currents in discontinuous intervals, has been used in electrochemistry and microfabrication communities to reduce stress and improve

uniformity (Xin 2005; Gladstein 2005; Gladstein 2001), we have found that pulse plating can also promote adhesion in neural interfacing microelectrodes (Byers 1986).

It has been hypothesized that plating under ultrasonic conditions promotes adhesion by introducing a ‘survival of the fittest’ evolutionary strategy to electrode formation (Marrese 1986). That is, the electroplated material that is loosely bound will detach due to the mechanical agitation, allowing only the persistence of robust formations. Pulse plating, by locally subjecting ions to alternating electrical forces on the surface of the electrodes, could have a similar role. Because pulse-plating may be easier to control than DC plating techniques, one of the objectives of this study is to compare the robustness of pulsed-plated electrodes with traditional DC-plated electrodes.

Unfortunately, the number of viable strategies in achieving mid-band electrode impedance control by closed-loop algorithms during electroplating is inherently limited. Specifically, in the case of platinum plating, there are two electrochemical phenomena that constrain the choices for control algorithms: (1) modulating the current density changes the electrode surface area, and (2) reversing the current fails to remove platinum deposits (inert platinum anodes do not replenish the platinum ions in solution). Therefore, we elected to monitor the impedance while applying electroplating currents until the electrode reached a desired impedance. In order to evaluate pulse-plating, we implemented this approach in two different ways: (1) In the control study, we simultaneously monitored the impedance during DC plating (i.e., the continuous method), and (2) As a test study, we monitored the impedance intermittently between briefs periods of pulsed electroplating current (i.e., the discontinuous method). Figure 2.6 illustrates these two approaches.

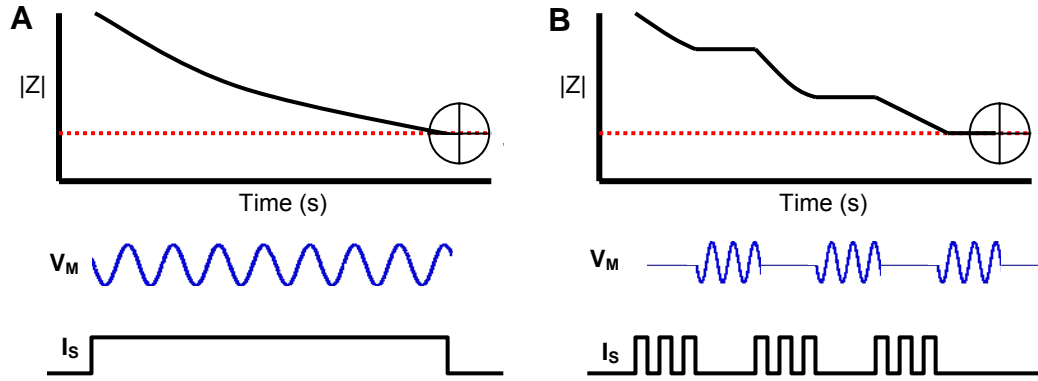


Figure 2.6: Impedance controlled electroplating strategies. (A) A sinusoidal, single-frequency voltage source, V_m , is capacitively coupled onto a DC electroplating current, I_s . The impedance magnitude is sampled continuously until the impedance of the electrode reaches the target level (It is important to note that the lumped circuit model of section 2.1 does not capture the non-linear dependencies of impedance on electrode voltage; thus the applied electroplating current will place the electrode into a different measurement regime than under zero-current conditions). (B) A potentially more robust alternative to DC plating is to sample the impedance between brief bursts of pulsed electroplating current.

2.2.3.2 Electroplating Device

In order to facilitate precise tuning of low-impedance microelectrodes, we designed an automated, closed-loop electroplating device to monitor the electrode properties during deposition. The basic operation of this device is described as follows: When plating current is supplied at the electrode, electrons supplied by the current source reduce the platinum ions to platinum metal at the surface of the electrode. As the platinum deposits accumulate, the impedance of the electrode decreases due to an increase in the surface area, A_s , which induces an increase in the capacitance, C_l , and a decrease in the charge transfer resistance, R_T , of the electrode. The system monitors this change in impedance by applying a 1 KHz relatively low-amplitude (10 mV or less i.e., approximately 2 orders of magnitude below the electroplating voltage), voltage signal across both the electrode and a reference resistor. The waveforms across the electrode and reference resistor are

continuously sampled with analog-to-digital converters and analyzed by real-time software to calculate the impedance magnitude:

$$|Z_{\text{elec}}| = R_{\text{REF}} \frac{|V_{\text{elec}}|}{|V_{\text{R}}|} \quad (2.4)$$

where R_{REF} equals the reference resistor, $|V_{\text{elec}}|$ is the magnitude of the voltage across the electrode, and $|V_{\text{R}}|$ is the magnitude of the voltage across the reference resistor. The error for this measurement is given by the following:

$$Z_{\text{err}} = \epsilon_{V_{\text{elec}}} \frac{R_{\text{REF}} + Z}{V_{\text{in}}} + \epsilon_{V_{\text{R}}} \frac{(R_{\text{REF}} + Z)Z}{R_{\text{REF}} V_{\text{in}}} \quad (2.5)$$

where z is the impedance of the electrode and ϵ is the measurement error. The impedance measurement error is minimized when the electrode impedance is equal to the reference resistor, which indicates that the reference resistor should be chosen to match the target electrode impedance.

The automated electroplating device was constructed by integrating a custom designed circuit board with a current source (Keithly 2400), function generator (HP 33102A), microcontroller (PIC 16F73) and laptop computer (Fig. 2.7). Electroplating current was switched onto one electrode at a time using two daisy-chained, 8-channel analog switches (MAX335). Although the device allows for up to 16 channels to be plated simultaneously, only one channel was plated at time to maximize individual electrode precision (Closing the loop around multiple electrodes at one time would insure that the *collective* impedance reached the target value rather than *individual* electrodes). The low amplitude voltage waveforms across the electrode and reference resistor were amplified for sampling using two instrumentation amplifiers (INA129P, Gain = 500x).

For DC electroplating, a constant electroplating current (I_{DC}) was applied while the impedance was continuously sampled (2 Hz , 8-bit ADC, PIC 16F73). For pulsed-plating applications, the impedance was sampled between discrete packets of pulsed-electroplating current with an I_{PLS} magnitude, T_{PLS} period, 50% duty cycle, and C_{PLS} pulse count. Real-time Matlab software (Mathworks) controlled deposition timing and coordinated activities among the electronic instrumentation (It can be beneficial to electroplate the electrode more than once, beginning first with a ‘primer’ or high-pulse count and subsequently electroplating with a lower pulse count). The measured impedance magnitude is a reflection of the full-electrode-electrolyte interface, thus it is important to remember that the electrolyte itself will influence the measurements. Calibration curves, which relate impedance in platinum plating solution to the impedance in the target environment (i.e., physiologic saline, in-vivo tissue, etc.), will facilitate accurate electrode tuning (though the electrodes will always be well matched). Fig. 2.8 shows a photograph of the completed device.

In addition to the electronic circuitry, an important consideration for the system is the physical interface to the MEA and electroplating solution. The mechanical package for the device (developed in collaboration with Mr. Shawn O’Connor) is composed of two main polycarbonate sections, a base, and lever, which interact via a hinge mechanism. This hinge is preloaded with two torsional springs such that the device behaves in a clip-board fashion. The base contains recesses that hold the MEA on one end and the main printed circuit board (PCB) on the other. An array of spring pin

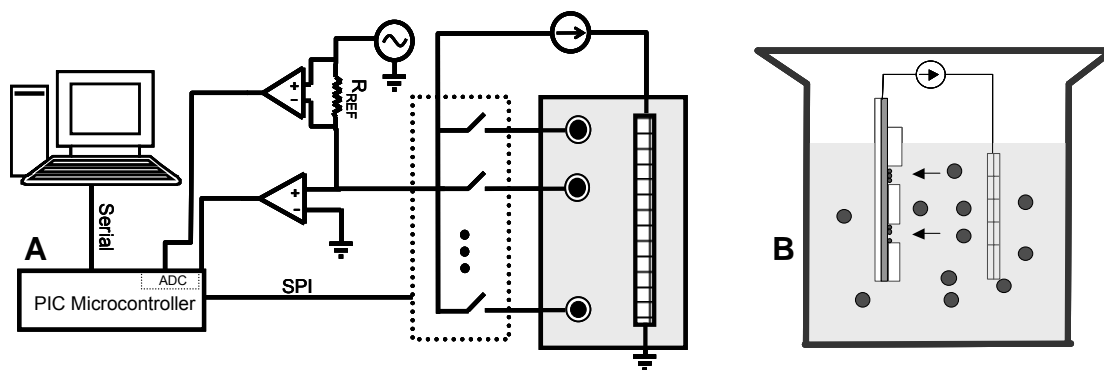


Figure 2.7: High level schematic and illustration of the closed loop electroplating system. (A) System level schematic of electroplating circuitry. A computer, via a serial connection to a PIC 16F73 microcontroller and custom circuitry, switches electroplating current onto individual electrodes. A 1 KHz sine wave is capacitively coupled (not shown) across the reference resistor and plating bath; the waveforms across the reference resistor and bath are sampled with the PIC A/Ds and communicated back to the computer for processing. (B) Illustration of electroplating. During electroplating, the MEA electrode surface becomes negatively charged and attracts positive platinum ions.

contacts is mounted on an interface board on the lever and provides the key electrical interface to the MEA pads. The interface board is then connected to the main PCB with a ribbon cable. The lateral positioning of the spring pins relative to the MEA surface is adjusted by rotating the hinge pin, which uses a screw to move the lever back and forth.

Figure 2.8 shows a photograph of the device.

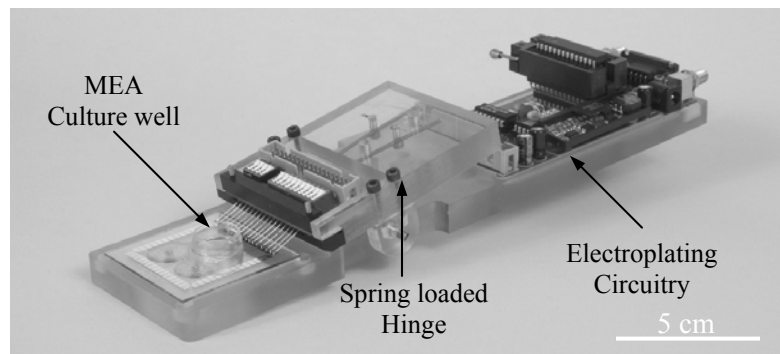


Figure 2.8: System integration of the electroplating device. The switching circuitry and impedance measuring electronics are physically separate from the electrode array (a ribbon cable, not shown, connects the two sections). Electroplating solution is introduced into the culture well of the MEA and a Pt-wire anode is inserted into the solution.

2.2.4 Results

We evaluated the performance of the electroplating device as well as the suitability of various plating techniques for proper adhesion and impedance tuning. Specifically, these techniques included monitoring the impedance during DC current plating and between timed bursts of pulsed plating currents. Additionally, we investigated the role of electrode impedance in evoking action potentials during the stimulation of dissociated cortical cultures.

The primary metric for evaluating device performance was the full spectrum measurement of the electrode impedance magnitude. In order to facilitate such measurements, a custom device was developed (in collaboration with Mr. Scott Buscemi) (Figure 2.9). This device enabled virtually any conformation of electrode selection, including multipolar configurations, through 206 digitally controlled switching and multiplexing elements (MAX335, MAX306). A desktop computer, via a custom MATLAB interface, coordinated all communication between a dynamic signal analyzer (Stanford Research SR725, through GPIB) and the custom switching board (PIC 18F442, through RS-232). For full-spectrum impedance measurements, the signal analyzer was configured to source a small (≤ 100 mV), sweeping sinusoidal voltage. For evaluating the performance of the electroplating device, the automated switching and measuring system was configured to apply the voltage source across an individual electrode, reference resistor, and a distant platinum wire ground. Specifically, the spectrum analyzer measured the voltage across the electrode and a 100 K Ω reference resistor using two instrumentation amplifiers (INA129P), and Matlab software calculated the impedance magnitude according to (4). As a result of this implementation, we could measure the

full-spectrum impedance magnitude of 60 individual microelectrodes within a few minutes.

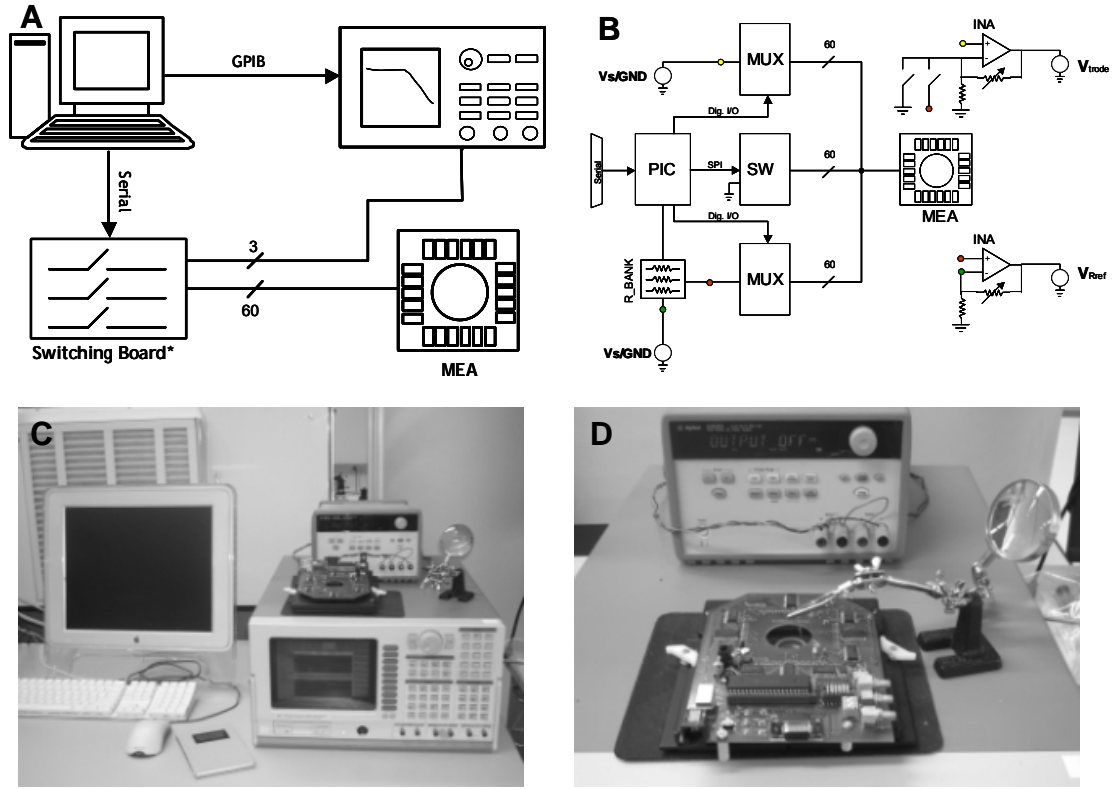


Figure 2.9: Automated Impedance Measurement tool. (A): System level schematic of Impedance diagnostic tool. Over 206 switching elements enable impedance measures of virtually any conformation, including common ground and intra-electrode schemes. (B) High level schematic of the switching and impedance measurement circuit. (C&D) Photograph of the impedance measuring system.

2.2.4.1 Device Performance

The primary goal for closed-loop electroplating was twofold: (1) lower the electrode impedance from its initial value to a relatively low target level and (2) minimize inter-electrode variability. In order to test the electroplating device against these two goals, we electroplated platinum black onto 30 μm diameter Au electrodes in an Ayanda Biosystems MEA (MEAv5Au) to a target impedance of 75 $\text{K}\Omega$ ($I_{\text{PLS}} = 2\mu\text{A}$, $C_{\text{PLS}} = 35$, $T_{\text{PLS}} = 10 \text{ ms}$) (See Appendix B for more details). Figure 2.10 demonstrates the

successful reduction of impedance by nearly 15-fold as well as reduction in inter-electrode variability, with a coefficient of variation (Standard Deviation/ Mean) of 3% at 1Khz. Additionally, the results in Fig 2.10B indicate that the electroplated electrodes were better matched across a full range of frequencies, demonstrating that 1Khz impedance matching is useful for reducing variability across the entire frequency spectrum.

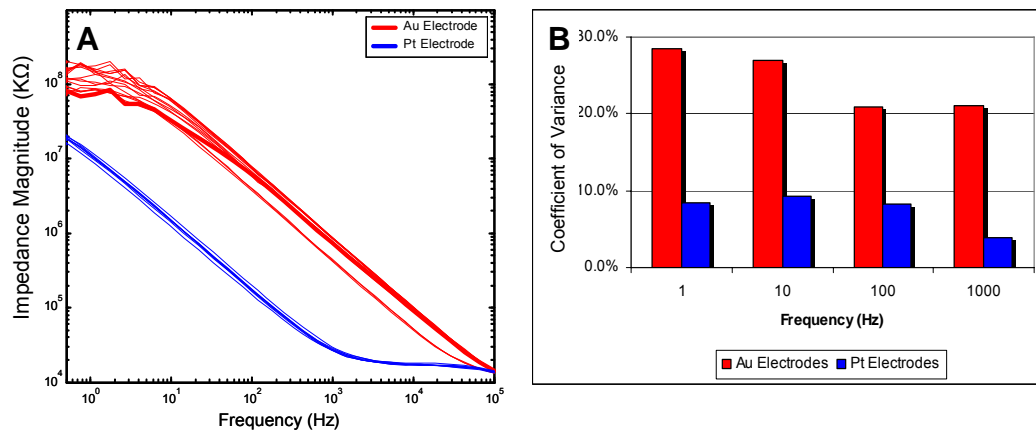


Figure 2.10: Reduction in electrode impedance variability. (A) Impedance Magnitude for (1) untreated 30 μm diameter Au electrodes in an Ayanda Biosystems MEA (MEAv5), and (2) platinized electrodes with a target impedance of 75 K Ω at 1Khz. (B) Coefficient of variation (Standard Deviation divided by the mean) for a set of 10 electrodes after electroplating (blue traces). Electroplated platinum black electrodes traditionally have substantial variation in their impedance magnitudes. For example, (Franks 2005) report variations of 600%.

Given the automated features of the device, it is also possible to customize individual electrodes within a multielectrode array. Fig 2.11A illustrates the targeted variation achieved by modifying the plating density between quadrants of the MEA. Additionally, Fig 2.11B demonstrates the accuracy achieved when targeting various impedance magnitudes at 1Khz. The independent control enables the investigation of the role of microelectrode impedance in a variety of neural interfacing applications (e.g., biosensing, electrophysiology, neural prostheses). In particular, one benefit to varying

target levels within a single MEA is that it allows for more controlled biological inquiry by removing variability that inevitably exists between experimental preps. Thus the same culture or target tissue can be investigated with a variety of matched electrodes.

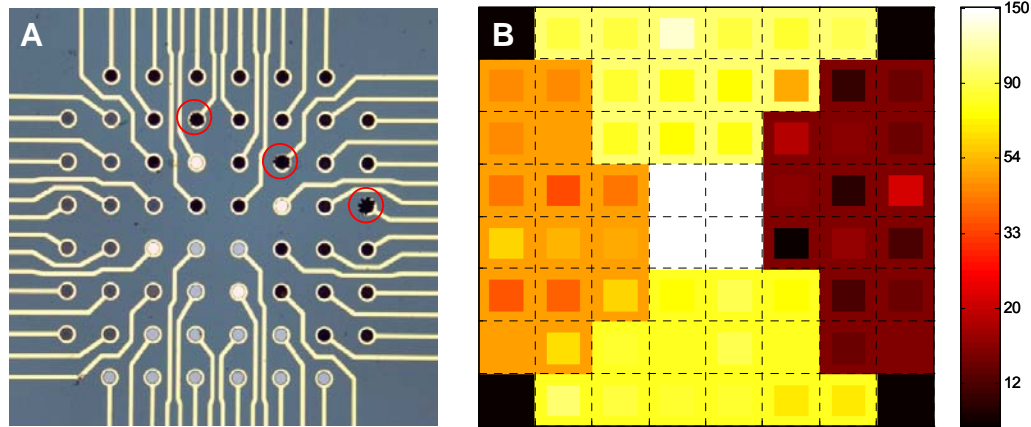


Fig. 2.11: Independent electrode control. (A) Optical micrograph of an electroplated Ayanda Biosystems MEA (MEA60Au). Each 30 μm Au electrode within a quadrant of the planar MEA was electroplated with platinum to match impedances. Various plating densities (clockwise from left: w, x, y, and z $\mu\text{A}/\text{cm}^2$) produced different surface morphologies corresponding to different colors). The red circles indicate three electrodes that were electroplated without feedback (B) In a separate study on a different MEA, each square (dashed line) represents an individual electrode in an 8X8 MEA. The outer perimeter of each square indicates the targeted impedance magnitude at 1Khz (K Ω), and the inner square represents the actual impedance value achieved by the device (clockwise from left, target impedance values of 50 K Ω , 100 K Ω , 15 K Ω , and 75 K Ω respectively).

2.2.4.2 Pulsed Plating Performance

Impedance matching is only useful if the microelectrodes can maintain a tight distribution near the target level during practical use. Unfortunately, normal MEA handling and use can introduce mechanical and electrochemical perturbations to the physical electrode that cause the electrode impedance to drift or shift from its original level. In order to test the robustness of electroplated electrodes as well as the suitability for pulse-plating to improve adhesion, we evaluated the resistance to mechanical wear of 30 μm diameter Au electrodes electroplated under two different conditions: (1) DC plating ($I_{\text{DC}}=1 \mu\text{A}$ or 0.35

nA/ μm^2) and (2) Pulsed-plating ($I_{\text{PLS}} = 2 \mu\text{A}$ or $0.70 \text{ nA}/\mu\text{m}^2$, $T_{\text{PLS}} = 10\text{ms}$, $C_{\text{PLS}} = 35$.) To account for the fact that the current density directly influences the electrodes' porosity and mechanical brittleness, we set the average current density of the pulse-plating trial equal to the current density of the DC trial (larger current densities produce more porous electrodes). Mechanical wear was applied to the MEA by immersing the unit in an ultrasonic bath for 30 seconds. Fig. 2.12 reports the mean relative shift in electrode impedance following ultrasonic agitation for both DC and pulsed-current methods. This figure demonstrates that pulsed-plated electrodes were much more mechanically robust than DC-plated electrodes. Further, despite a 40% shift in mean electrode impedance, the distribution remains relatively narrow (Coefficient of variance 15%).

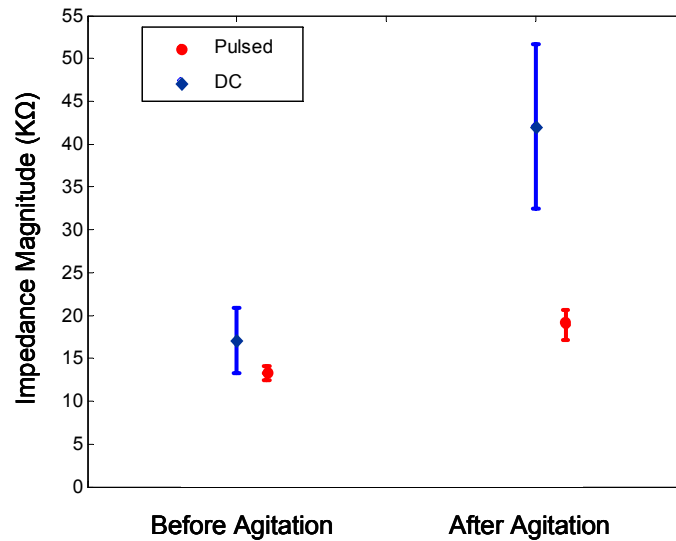


Figure 2.12: Electrode Robustness. Electrodes were subjected to 30 seconds of ultrasonic agitation to emulate mechanical wear on the MEA devices. Shown is the shift in mean impedance for both DC and pulsed plating methods. When normalized for the mean relative shift, the data indicates that DC plated electrodes shifted 3.5 times more than pulsed-plated electrodes.

2.3 Applications to Neural Stimulation

In sections 2.1 – 2.2, we presented technologies that explicitly control the size, location, density, and electrical properties of microelectrodes. Control over these electrode

variables presents many opportunities for improved stimulation, including (1) modeling *voltage* stimulation induced electric fields, (2) modeling common-ground induced voltage fields (*current* stimulation), (3) garnering spatial control over the stimulus input (4) sculpting dish-wide voltage field contours, (5) simplifying stimulus artifact elimination, and (6) imposing voltage safety constraints. In this section, among the many possibilities for exploring electrode-induced stimulation behavior, we present applications for voltage stimulation and for improved control over the voltage fields.

Voltage stimulation, though highly effective in eliciting cellular responses, is directly scaled by the electrode impedance. Thus, without explicit knowledge of the electrode impedance, it is not possible to model the electric fields in the dish or to derive charge-balanced stimuli (for artifact suppression). As a result, the same stimulus protocol, when applied to mismatched electrodes, will produce entirely different electric fields. Despite these disadvantages, positive-then-negative biphasic voltage stimulation has been shown to be one of the most effective methods for eliciting a broad response from cultured neural networks (Waganaar 2004). Further, it has been shown that cellular responses are nearly perfectly time locked to the downward voltage transition between phases (Bakkum 2007), allowing for the possibility of precisely timing cellular excitation. In this section, we illustrate how this effective stimulus strategy can be made even more potent by reducing and matching the electrode impedance, in essence making the use of voltage stimuli much more reliable and predictable.

In order to experimentally investigate the relationship between the electrode impedance properties and the biphasic voltage stimulus applied, the electrode model in Fig. 2.1A was used to derive a closed form expression that relates the electrode circuit

parameters to the induced voltage fields in a culture dish. As a first order approximation, which ignores the non-linear variation of the electrode elements as a function of voltage, the maximum voltage produced in the media from a biphasic pulse can be shown to be:

$$-V_{\max} \approx \frac{-R_{s2}}{R_{s1} + R_{s2}} \Delta V \left(1 - \frac{\Delta t}{2C_l(R_{s1} + R_{s2})} \right) \quad (2.6)$$

where ΔV equals the maximum change in stimulus voltage, and Δt represents the transition time between stimulus phases. For this analysis, we divided the spreading resistance into two components, R_{s1} (the proximal resistance from the electrode to a theoretical iso-potential shell that stimulates a cell) and R_{s2} (the resistance of such shell to the rest of the media and the distant reference electrode) such that $R_s = R_{s1} + R_{s2}$.

In (2.6), decreasing the impedance has the effect of increasing capacitance, C_l , which allows for a reduction in ΔV without compromising the magnitude of V_{\max} . Thus, a greater number of cells can be stimulated with a lower amplitude stimulus (Figure 2.13A). This theoretical analysis is experimentally demonstrated in Fig. 2.13B, in which dissociated cortical neurons in an MEA were consistently stimulated at lower magnitudes using electrodes with lower impedance values (culture methods are presented in (Potter 2001)). An alternative (and equally valid) method to interpreting the results is to consider that for a given voltage, a lower impedance electrode will deliver more current to the dish. Thus, low impedance electrodes provide a great deal more ‘head-room’ to apply larger, more effective stimuli without exceeding the electrochemical safety limits. Additionally Figure 2.13B, also shows the importance of minimizing electrode variability for voltage stimulation, as impedance clearly plays a role in determining the scope of an evoked response.

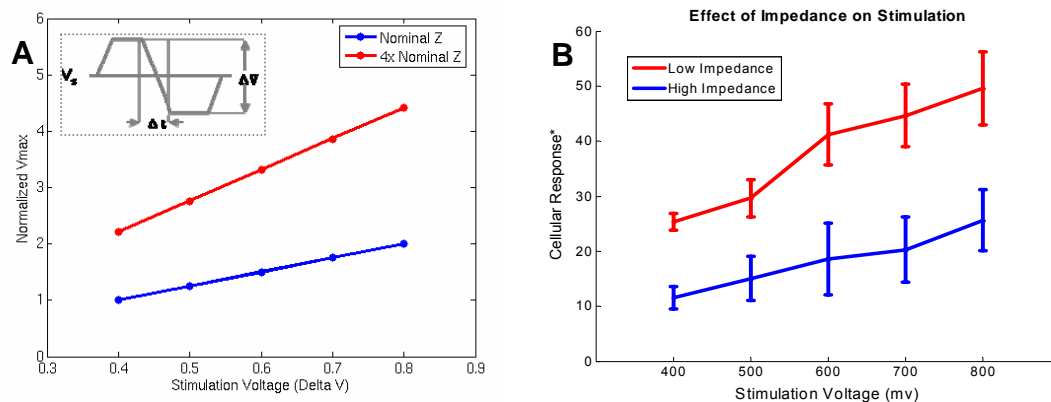


Figure 2.13: The effect of impedance on the cellular response to stimulation.

(A) Theoretical normalized Vmax as a function of the stimulus voltage and electrode impedance using the model depicted in Fig 1A. For a given stimulus input, the nominal impedance electrode (blue trace: $R_s = 10\text{K}\Omega$, $R_M = 1\text{K}\Omega$, $C_I = 3\text{pF}$, $\Delta t = 10\text{ ns}$) presents a lower Vmax to the culture dish than the lower impedance electrode ($C_{I,2} = 4 \times C_I = 12\text{ pF}$) (Inset) Shows the parameters of the applied voltage waveform. (B) The actual cellular response (as a function of stimulus magnitude) of a low impedance electrodes ($15\text{ K}\Omega \pm 4$) is compared to a high impedance electrodes ($75\text{ K}\Omega \pm 12$). Cellular Response is defined as the total number of spikes, recorded across the entire dish, that occur within 50 ms of a stimulus. Biphasic pulses with random inter stimulus intervals and random order of magnitudes were applied to the electrodes. Low impedance electrodes were able to elicit a greater cellular response for a given stimulus magnitude.

2.4 Discussion

In this chapter we presented microfabrication technologies for precisely controlling key electrode parameters including size, location, density, and impedance. Additionally, we used models and experimental results to illustrate the importance of these parameters to influencing the efficacy of stimulation. To facilitate increases in electrode density and count, two microfabrication techniques were developed that will ultimately enable greater control over dish-wide voltage fields. Further, we demonstrated that PCB surface irregularities could be overcome to permit the use of a very inexpensive platform for fabricating high-density arrays. Finally, we developed a closed-loop electroplating approach and pulsed plating protocol that performed according to theory and was able to

match all electrodes with uniformly low impedance magnitudes. The applications for low, matched impedances were demonstrated in experiments with dissociated cortical cultures.

In the present device, we elected to do all of the impedance computation using MATLAB, delegating only switching and sampling functions to the PIC microcontroller. While this was simpler to implement, this strategy suffered from having long communication delays between the laptop computer and microcontroller, which significantly limited the rate at which we could sample the electrode impedance (2 Hz). Using a nominal electroplating density ($0.12 \text{ nA}/\mu\text{m}^2$), the platinum black electroplating process usually takes on the order of 10 seconds to coat the electrode; thus, this sample rate is too slow for very tightly controlled systems. Lowering the current density to decrease the plating rate is unfavorable, as it would also decrease the surface area of the electrode. Intermittent polling (between bursts of electroplating current) solved this problem and presented adhesion advantages, but, in the future, real-time computation at the microcontroller would speed up the application significantly.

To simplify computations, our device only uses the magnitude of the AC response at the electrode. Although this choice performed adequately for our experiments, a more robust method that can reduce sampling noise and provide additional information could be preferable and provide better results. By finding the projections of the AC response onto the space of the test signal, that is, finding the in-phase and quadrature (I&Q) components of the response, it is possible to extract precise magnitude and phase information and to monitor the impedance at different frequencies simultaneously. This

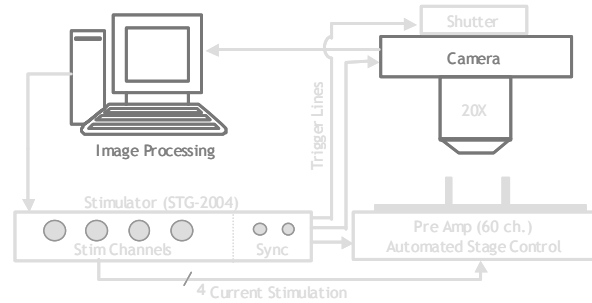
extra information can be used to automate other aspects of the process, such as variations in plating density, to obtain better-matched electrodes.

In addition to implementing I&Q methods for rapid automated plating, future improvements will include further characterization of pulse-plating as well as implementation of alternative control strategies. Specifically, coupling a theoretical analysis of pulse-plating with experimental exploration of the pulse-plating parameter space (period, duty cycle, etc.) could generate optimum electroplating protocols for generating robust electrodes. Additionally, in the current device, the electroplating parameters were fixed and only the duration of the electroplating process was allowed to vary; future versions will explore more sophisticated control strategies, such as a proportional controller that varies the number of pulses applied based on the proximity of the electrode impedance to the target value.

For this work, we monitored the mid-band of the impedance magnitude because this frequency range was the most important to electrophysiologists interested in action potential studies. However, an alternative approach for MEMs applications may be to monitor the impedance at higher frequencies. Our own preliminary results, as well as the electrode models presented in section 2, indicate that this measurement is almost exclusively dominated by the spreading resistance, which is related to two variables: (1) the resistivity ρ of the solution (which is unlikely to change during electroplating) and (2) the base area, A_B . This suggests that for micromolding applications, monitoring the high-band impedance during electroplating may allow for precise device construction, as the impedance in the high-band does not change until the electroplated material completely fills the mold.

CHAPTER 3

IMAGE PROCESSING TECHNOLOGIES: OBSERVING NEURAL CELLS



Although the customized electrodes of chapter 2 are critical for stimulating neural tissue, these extracellular electrodes may not be well suited for high-resolution, single-cell observation (i.e. recording) of the stimulus response. Optical imaging and image analysis techniques, however, provide a powerful means to rapidly and accurately assess the geometry, location, and evoked activity of *individual* cells. In this chapter, we present novel image processing methods that permit functional and spatial analysis of populations of neuronal somata possessing rich morphological detail and dense neurite arborization throughout 2-D and 3-D constructs in vitro. This image analysis system incorporates several automated features for the discrimination of neurites and somata by initially classifying features in 2-D and subsequently merging these 2-D classifications into 3-D objects, thus utilizing 3-D reconstructions to automatically identify and correct segmentation errors. Additionally, we present algorithms for the automated functional tracking of individual neurons within 2-D cortical cultures.

As image acquisition techniques and cell culture technology advance to permit utilization of complex 2-D and 3-D environments, there is an increasing need for analysis tools to facilitate the investigation of cell morphology and function within this

framework. Specifically, automated image analysis routines for rapid and accurate segmentation of fluorescently labeled neural cells and/or their processes would facilitate such studies. Of particular interest to this work is the ability to automatically identify the locations of individual cell bodies with respect to the electrode and to rapidly track stimulus evoked activity. Unfortunately, problems typically associated with automated image analysis are exacerbated in neural systems, where issues such as diverse cellular morphologies, process outgrowth, and high cell densities confound typical analyses.

Automated segmentation algorithms provide a means for high throughput mapping of complex morphological and functional interactions. Although many routines can accurately quantify nuclear (i.e., spherical) labeling in 2-D or 3-D, nuclear stains alone are inherently limiting as they omit information pertaining to such important measures as cell morphology, neurite outgrowth, and cell-cell interactions (e.g. receptor-mediated or synaptic). The goal of this work was to bridge the analysis gap presented in (1.2.3) and offer researchers tunable, automated image analysis techniques with user-controlled corrections that were optimized to deal with issues specific to functional and spatial analysis of 2-D and 3-D neural systems.

Previous studies have addressed 2-D and 3-D *nuclear* segmentation techniques (Irinopoulou 1997; Lin 2005). One particular algorithm repeatedly employed is the highly efficient watershed algorithm (Lin 2003; Adiga 2001). Despite the widespread use of this algorithm for delineating cellular objects, this technique is notorious for over-segmentation, an error that occurs when distinct nuclei are broken down into multiple components. Other investigators have reduced this problem by using *a priori* knowledge to skillfully sculpt image contours that guide object segmentation. For example, one

technique used a hybrid of gradient cues and geometric distance transforms, to shape the image based on both geometric and intensity features (Lin 2003). Another technique avoided region based segmentation algorithms altogether and drew lines between coupled indentations or ‘necklines’ to split overlapping nuclei (Belien 2002). While these processing methods improved segmentation results, they could not entirely prevent over-segmentation. For the remaining errors, post-processing has proven to be very effective. In particular, Lin and Adiga have demonstrated excellent results by using geometric measures (e.g, area, convexity, and texture) to define merging criteria for neighboring segmented objects (Adiga 2001; Lin 2003; Lin 2005).

Among the challenges in neural image processing are to develop algorithms that rapidly distinguish somata from neurites and that provide automated compensation for over- and under-segmentation errors. For this application, in which the intention is to extract the boundaries of somata from images with dense neurites, the watershed ‘over segmentation’ of neurites becomes an asset. The spiny and dimpled projections (or recessions) of the neurites ‘misdirect’ the watershed routine and produce heavily splintered and fractured elements. Cell bodies, on the other hand, tend to have rounder, smoother morphologies. In this regard, the segmentation of cells and neurites take on entirely different shapes and sizes, and, it is on the basis of these differences, that an algorithm could classify and thus remove unwanted features from the image. However, while fractured segmentation is intended for neurites, it is undesirable when it occurs in somata. In the case of 3-D images, software routines could remedy cell body over-segmentation by using 3-D context clues to identify problem areas. Specifically, one

could first segment cells in each 2-D frame, and use information from overlapping cells in adjacent frames to identify errors.

In this chapter, we present methods that rapidly distinguish cell bodies from neurites in three different applications: (1) 2-D somata segmentation, (2) 3-D somata segmentation, and (3) 2-D functional segmentation. First, we develop novel techniques for rapidly distinguishing somata from neurites, artifacts, and other features. Second, we build on this platform to segment somata from 3-D images and to automatically identify and correct both over- and under-segmentation errors. Next, we again build on the 2-D segmentation platform to enable the automated functional tracking of network activity, which greatly assists our ultimate goal of tracking stimulated activity. This analysis platform provides valuable tools for unbiased measurements of neural cells within a 2-D or 3-D context.

3.1 Automated 2-D Somata Segmentation

Among the many variables that influence the neural response to extracellular stimuli, is the location of the neuron with respect the stimulating electrode(s). Thus, the ability to identify the precise locations of neurons within images possessing complex morphologies is of critical importance. In this section, as a first step towards functional tracking of 2-D network activity, we present algorithms that rapidly and automatically identify the boundaries of neural cell bodies. This work lays the foundation for automated 3-D segmentation and 2-D functional tracking presented in (3.2) and (3.3) respectively.

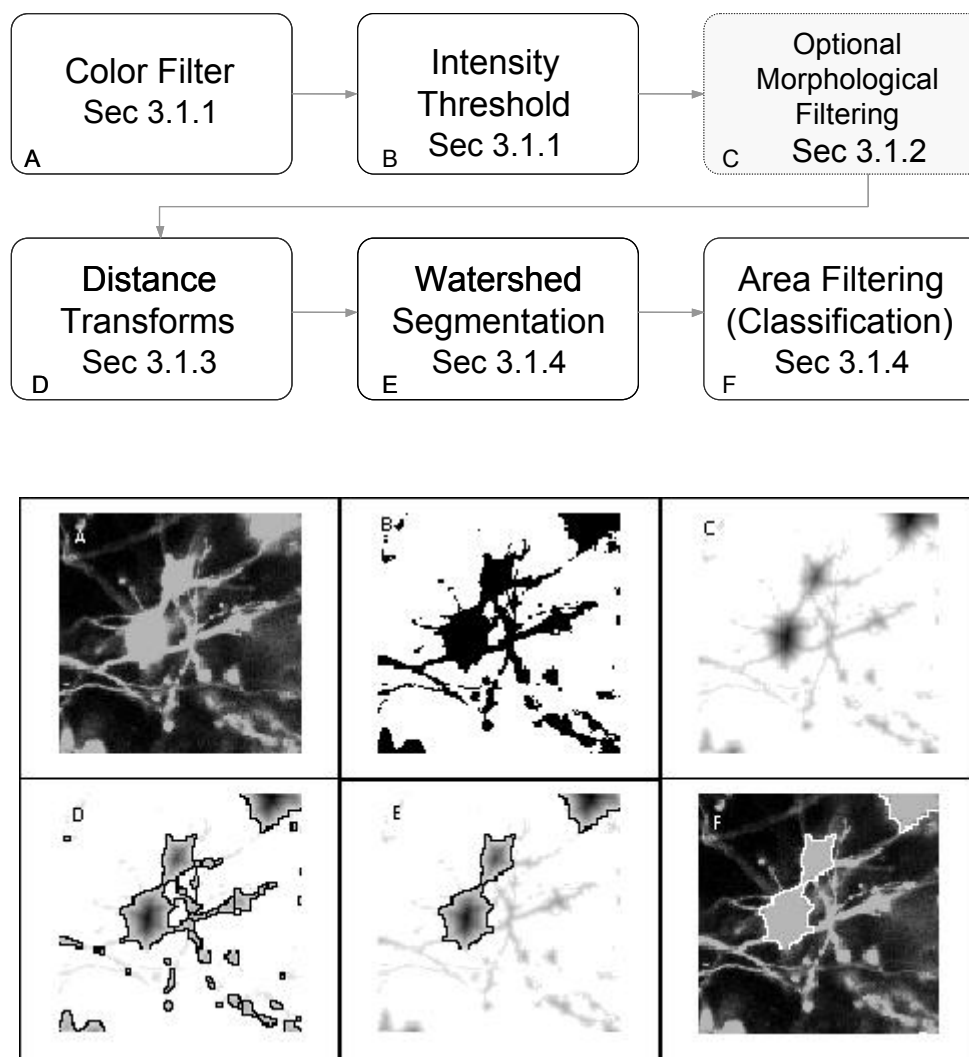


Figure 3.1 Flow diagram for the 2-D segmentation of cell bodies. (Top) Flow diagram for 2-D segmentation. Graphic representation of 2-D segmentation process: (A) The color component for the fluorescent dye of interest was extracted to form an achromatic intensity image; (B) A global threshold was applied for each 2-D frame in the z-stack, separating pixels into foreground (regions of interest) and background; (C) The regional minima were defined by applying the Euclidean distance transform (or alternatively the chebyshev transform) to the ‘thesholded’ image; (D) The watershed algorithm was applied to the transformed image: the mottled contours of the neurites produced very fractured segmentation boundaries, while the rounder, smoother morphologies of the soma produced accurate segmentation boundaries; (E) Objects were classified as either soma or neurite fragments according the area enclosed by the watershed lines, and neurite fragments were removed from consideration. (F) Picture of the cell body boundaries projected back onto the original image.

3.1.1 Color Filtering and Global Thresholding

As a first step toward identifying somata, we used color and intensity cues to separate the image into foreground and background regions. Through a Matlab routine, the user could examine color-specific intensity histograms for each 2-D frame in the z-stack. For a specified dye, the color component was extracted, and each frame was transformed into a grayscale image (Figure 3.1A), whereupon a global intensity-based threshold, T , was applied to separate the image pixels into foreground and background (Figure 3.1B). Pixels with an intensity value above the threshold were identified as potentially belonging to somata, and were assigned a value of 1. Pixels below the threshold were assigned a 0 or background value:

$$I(x, y) = \begin{cases} 1 & I \geq T \\ 0 & \text{Else} \end{cases} \quad (3.1)$$

where x and y represent the pixel indices within a 2-D image frame. Following the application of the threshold, the remaining objects in the binary image consisted of somata, neurites, and image artifacts.

3.1.2 Optional Morphological Filtering

After separating images into foreground and background regions, morphological operators can be applied to remove holes inside remaining objects (and to separate overlapping objects that are connected with very narrow regions). In our test images, there was very little intensity variation among the pixels that represented somata; therefore, the application of a global threshold did not produce holes in the foreground objects. (In order to capture images with rich morphological detail, we used a high

intensity light source during image acquisition, and, as a result, many of the soma and neurite pixels were at or near saturation.) Thus, for most images, we did not require morphological filtering to reshape the binary images; however, in some images, where cell clustering was rampant and neurite outgrowth pervasive, we used a ‘small’ diamond shaping-element to mildly erode the post-threshold, binary images:

$$I(x, y) = k \circ I(x, y), \text{ where } k = \begin{array}{|c|c|c|} \hline 0 & 1 & 0 \\ \hline 1 & 1 & 1 \\ \hline 0 & 1 & 0 \\ \hline \end{array} \quad (3.2)$$

In general, there may be advantages to avoiding morphological filtering, as the resulting smoothing can remove spatial cues that naturally indicate overlapping objects (Crespo & Maoio 1999; Kumar & Shunmugam 2006). Given the lack of intensity variation within the soma of our images, it was important that ‘necklines’ and other inflection points were preserved to help properly define the regional minima that guide object segmentation. So, while the successive use of dilation and erosion operators may help remove some neurite features, such measures may also remove critical boundary indicators.

3.1.3 Distance Transforms

The successful application of the watershed algorithm requires that each object is marked by a regional minimum and that the image contours more or less follow the object boundaries. Unfortunately, natural intensity gradients are not sufficient to define the regional minima for each object (Lin et al 2003). This was particularly true of our test images, where nearly saturated pixels presented very little texture in the soma region. To derive the regional minima and object contours, the Euclidean distance transform was applied to the stack of binary images (Fig. 3.1C):

$$I(x, y) = \sqrt{(x - x_b)^2 + (y - y_b)^2} \quad (3.3)$$

where x_b and y_b represent the coordinates of the nearest background pixel. The local minima were assigned to pixels with the maximum distance value to the nearest background pixel. For most test images, the Euclidean transform produced satisfactory results. However, some images with a high degree of clustering and dense neurite outgrowth, the chebyshev or ‘chessboard’ transform was used to minimize over-segmentation errors:

$$I(x, y) = \max(|x - x_b|, |y - y_b|) \quad (3.4)$$

The Euclidean distance transform accounts for the projection along both the x and y axes between a given pixel and its geodesic distance to background. Because the chebyshev transform defines values based on the maximum projection along the x - or y -axis, the determination of the local minima may be more immune to erratic variations along one axis. Thus images with extremely rich and complex morphologies appear to be less susceptible to segmentation errors.

3.2.4 2-D Watershed Segmentation and Object Classification

After the regional minima were defined by the transformed images, we applied a 2-D watershed algorithm to segment the objects (Fig. 2D). The watershed algorithm involves interpreting the image as a surface in which points of the same intensity value are at the same height, and classifying points according to the direction of the gradient at their respective locations: (1) regional minimum, points that reside at a local minimum of the surface, (2) ‘catchment basins’, points whose gradients point in the direction of the same minimum, and (3) ‘watershed lines’, points that reside at a local maximum, and thus

could belong to any adjacent minima. A common analogy for describing the watershed algorithm involves punching a hole in each regional minima and then flooding the entire image from the bottom. Watershed lines or segmentation boundaries are then constructed to prevent distinct flooding regions from overlapping. Many details on 2-D and 3-D watershed implementations have been previously described (Adiga & Chaudhuri 2001; Gonzalez & Woods 2002).

The watershed algorithm produced segmentation boundaries that were related to the image contours. Whereas the mottled contours of the neurites resulted in highly fractured objects, the relatively smooth morphologies of cells produced larger and rounder objects. It was on the basis of these differences that we easily distinguished between object types. Figure 3.2 demonstrates a typical bi-modal distribution for segmented objects binned by pixel area. Objects less than the area threshold, α , were labeled neurite fragments, and objects greater than α were labeled cellular objects. Subsequently, all segmentation boundaries corresponding to objects with areas lower than α were dismissed from consideration (Fig. 3.1E). The populations were not perfectly distinct, so there was a small probability that some neurite fragments remained; likewise, a few small cell bodies could have been removed.

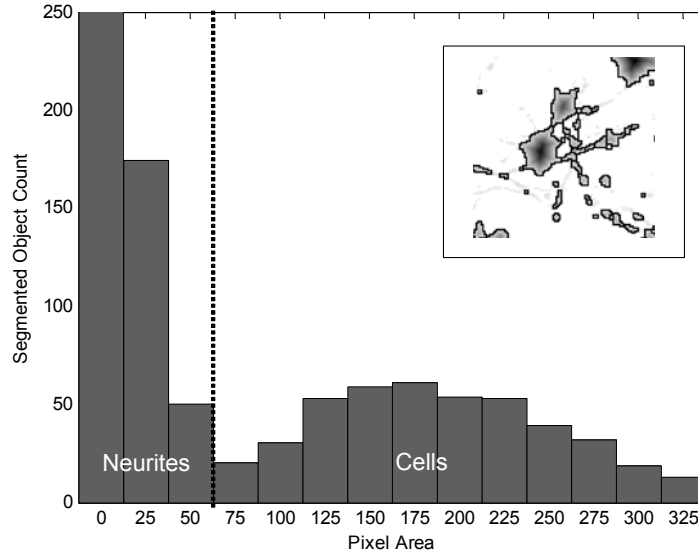


Figure 3.2 Distribution of segmented objects binned according to pixel area. The morphological differences between neurites and somata produce watershed segmentation boundaries that, when binned according to pixel area, fall into two distinct populations. The threshold, α (vertical, dashed line), is used to separate objects into neurites and cell-bodies. Objects with a pixel count or area $\geq \alpha$ are labeled ‘cells’; objects with an area $< \alpha$ are labeled ‘neurite fragments’. (Inset) Watershed boundaries for somata and neurite fragments.

3.2 Automated segmentation of 3-D somata

In the previous section, we demonstrated an approach to automatically identify soma boundaries in 2-D cultures. While these algorithms make strides towards our goal of automatically tracking stimulus evoked activity, they lack the ability to analyze cells in a more natural, 3-D environment. In this section, we build on the 2-D algorithms from the previous section to develop routines that segment somata in three dimensions.

3.2.1 Algorithm Overview

In order to segment 3-D cellular objects in a confocal stack of 2-D images (z-stack), we considered two different strategies: (1) segmenting cells in 2-D slices and

merging overlapping cellular objects (Belien 2002; Irinopoulou 1997; Tekola 1996), and (2) segmenting cells in 3-D volumes (Adiga 2001; Chawla 2004; Sarti 2000). We choose the former because an analysis of this type easily lends itself to visual feedback and rapid error correction, and the merging of 2-D ‘blobs’ into 3-D cellular objects provides an opportunity for error identification and correction. Furthermore, 2-D segmentation with 3-D ‘stitching’ can be computationally much less expensive than 3-D segmentation and may enable more rapid processing. Undoubtedly, some of these advantages are not exclusive to this strategy, but they do more naturally fall out from this approach (and clearly build on our work from section 3.1).

3.2.2 3-D Merging and Error Identification

Following the watershed segmentation and object classification of (section 3.1.4, Fig 3.1D), each 2-D frame contained segmented objects that fell into one of three categories: (1) correctly segmented somata, (2) false positives (neurites, artifacts, and over-segmented cells), and (3) false negatives (under-segmented somata and unidentified cell bodies). To identify the cellular boundaries in three dimensions, we merged 2-D objects into 3-D cell bodies, and we used conflicts that arose during merging to identify and, in most cases, automatically correct segmentation errors (Fig. 3.3). The algorithm for merging 2-D ‘blobs’ into 3-D cells involved assessing the merger from two vantage points: (1) the *forward projection* of a 2-D cellular object onto overlapping objects in the adjacent frame and (2) the *reverse projection* of overlapping objects back into the original frame. These two vantage points insured that only cells with maximum *mutual* overlap were merged. (A scenario, which we refer to as ‘unrequited overlap’, can arise where an object, C_1 , in Frame F_i maximally overlaps with another object, C_2 , in Frame

F_{i+1} which shares the greatest maximum, mutual overlap with yet another object, C_3 , in Frame F_i .)

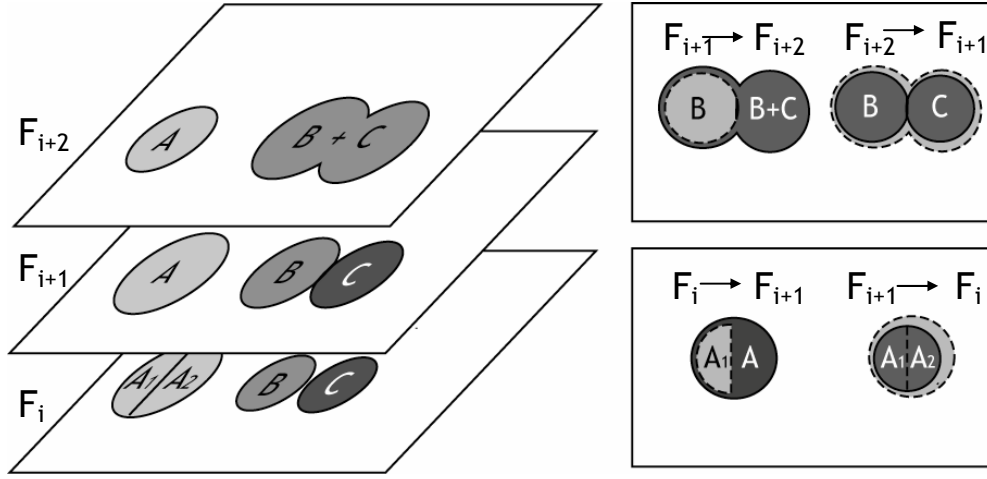


Figure 3.3 Illustration of 3-D merging and error identification. (Left) This figure exemplifies segmentation results for three cells—A, B, and C—which appear in frames F_i , F_{i+1} , and F_{i+2} . In Frame F_{i+1} , we show three correctly segmented somata. In Frames F_i and Frames F_{i+2} we illustrate over-and under-segmentation errors respectively. 2-D objects are merged into 3-D cell bodies if the percentage overlap between the objects is $\geq \beta$, where β can be any number between 0 (no overlap) and 1 (100% overlap). The merging algorithm considers two frames at a time, and segmentation errors are identified when multiple objects in a single frame exceed β . (Top Right) For example, cell B from frame F_{i+1} was projected into F_{i+2} . All object(s) in F_{i+2} that overlapped with B’s projection (dashed cell boundary) were considered as merging candidates; in this case, the object $B+C$ satisfied the percentage overlap criteria. However, the reverse projection of B’s best merging candidate, $B+C$, back onto the previous frame identified two objects that satisfied the merging criteria: B and C. Because three objects—B, C, and $B+C$ —were eligible for merging, the under-segmentation error was identified (gray box). (Bottom Right) In a similar fashion, the forward projection of A_1 into F_{i+1} overlapped best with A; however, the reverse projection of A_1 ’s best merging candidate significantly overlapped with two objects: A_1 and A_2 , thus identifying a 2-D segmentation error.

In addition to the mutuality criteria for merging 2-D objects into 3-D cell bodies, we required that the percentage of object overlap between 2-D objects exceed an empirically defined threshold, β - defined as the proportion of the intersecting pixels, $\text{Area}(c_i \cap c_{i+1})$, to an object’s pixel count, $\text{Area}(c_i)$. If *multiple* objects from either vantage point exceeded β , then a segmentation error likely occurred. Any number of

actions could then be taken to resolve the conflict, such as merging over-segmented objects, splitting under-segmented objects, or flagging the offending object pixels for manual user validation (at the conclusion of all automated routines). For our application, we choose a simple mode of action: for all errors identified in the forward projection, we merged objects *and* set flags for user validation; for errors identified in the reverse projection, we only flagged the offending objects for user validation. (Empirically, it was determined that most identified errors required merging but that under-segmentation, which requires splitting, was more likely to be identified in the reverse projection.) The threshold, β , took on any value between 0 (no overlap) and 1 (complete overlap), where the smaller the parameter implemented, the more sensitive the algorithm was to potential errors. In any frame, if a 2-D cellular object was not connected to pixels in the adjacent frame(s) it was assumed to be an artifact or neurite and was removed. The algorithm is summarized in pseudo-code form below:

```

Procedure 3Dmerge_ErrorCheck

Fi = Frame in z-stack
CFi = {Set of 2-D objects in Frame, Fi}
CFij = 2-D object in CFi
Initialize: EFi = {∅}; Set of objects marked for error
Initialize: CeFi = CFi ∨ Fi; Set of objects eligible for 3-D merging

For each Frame in the z-stack, Fi
  For each eligible cell, CeFij, in the current Frame, Fi
    Fk = Fi
    Repeat
      1. Project CeFkj onto Fk+1
         Co ← CeFkj ∩ CFk+1; Co is the set of overlapping objects in CFk+1
         If objects in Co exceeding  $\beta$ , Cb, are greater in number than 1
           A. Merge Cb in 2-D
           B. Flag objects for error check; EFk+1 ← EFk+1 ∪ Cb ∪ CeFkj
      2. Project Cb onto Fk
         Co ← Cb ∩ CFk; Where Co is set of overlapping objects in CFk

```

```

        If objects in  $C_o$  exceeding  $\beta$ ,  $C_r$ , are greater in number than 1
        A. Flag objects for error check;  $E_{Fk} \leftarrow E_{Fk} \cup C_r$ 
3. If  $Ce_{Fk}^j$  AND  $C_b$  share the greatest mutual overlap
    A. Merge  $Ce_{Fk}^j$  and  $C_b$  in 3-D
    B. Remove  $C_b$  from the eligibility set,  $Ce_{Fk+1}$ 
    C. Increment  $F_k$ 
Until  $Ce_{Fk}^j$  is NOT attached to a new object in 3-D (Step 3A)

```

3.2.3 Software Assisted Manual Validation

During the 3-D merging routine, a database was constructed to catalog information about each cell, including its geometric properties (such as eccentricity and concavity) and pixel coordinates. The benefits of the database were twofold: (1) it provided valuable statistics and information about the segmented cells, and (2) it was useful for rapid visual feedback and user-guided corrections. The indices that corresponded to the boundaries of segmented objects were projected onto the original 2-D images in the z-stack. The user validated the images by scrolling through each 2-D frame to observe the segmentation boundaries. To expedite manual edits, conflicts identified during 3-D merging were flagged (with red pixels) to draw attention to the most probable areas that required user input (Figure 3.4). The mouse was used to display statistics about a suspicious or flagged cell (such as cell ID number, area, equivalent diameter) to help assess the accuracy of a particular cell boundary. Following a decision about the accuracy of the automated boundary, the following mouse commands were used to manually edit the image:

```

Left click: add/delete cell in current 2-D frame
Middle click: merge over-segmented 2-D cells
Right click (and hold): manually draw cell boundary

```

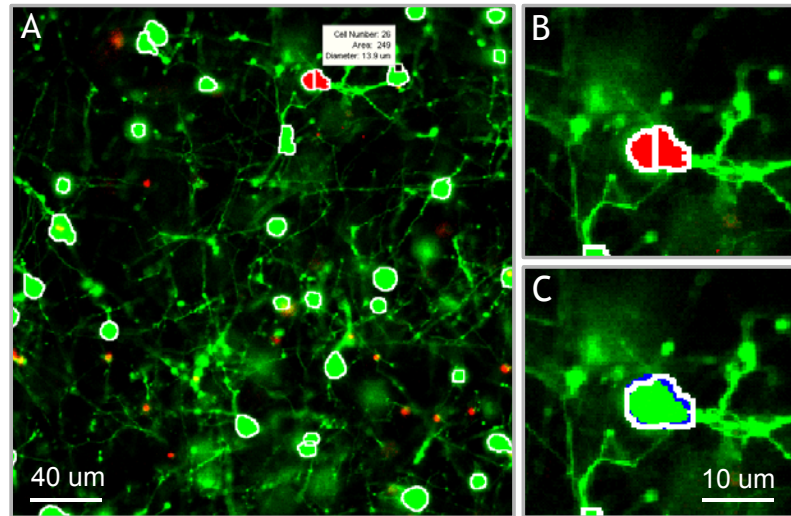


Figure 3.4: Illustration of software tools. The segmentation algorithms were integrated into a graphical user interface (GUI) to facilitate visual feedback, parameter selection, and software-assisted error correction. (A) Segmentation boundaries (white) are projected onto individual frames in the z-stack (a scroll bar, not shown, is used to switch between frames.) Segmentation data, including cell ID number, area, and diameter (white box), are displayed for a selected cell. (B) Potential segmentation errors are automatically flagged in red. (C) A user-applied mouse command instructs the software to perform a merge operation. Blue pixels outline the object in the forward adjacent frame that is connected to the merged cell. (Gray pixels, not shown, indicate connected objects in the previous frame.)

Each correction, addition, or deletion of a cell in a 2-*D* frame evoked a cascade of procedures that managed the creation, deletion, merging, and splitting of 3-*D* cells. Cells were automatically merged in 3-*D* if they satisfied the maximum overlap criteria (as defined in section 3.2.2). Segmentation lines for 2-*D* cells in adjacent frames that were merged to a user-selected cell were color-coded and displayed in the current frame. These methods allowed the user to confidently produce near 100% accuracy in very little time. This is especially useful in applications where highly accurate on-line cell segmentation and identification is required for optical tracking of network activity.

3.2.4 Algorithm Performance

The segmentation routines were rigorously tested against a variety of image and culture conditions. These results indicate that in practical implementation, segmentation accuracy could approach 100%. (Dr. Kacy Cullen developed the cultures, acquired the images and assisted in testing the 3-D segmentation algorithms)

3.2.4.1 Test Cultures

The cultures for image testing were prepared with the following protocol: Neurons were derived from embryonic day 17-18 rat fetuses by isolating the cerebral cortices, which were dissociated using trypsin (0.25%) + 1mM EDTA (10 minutes at 37 °C) followed by DNase (0.15 mg/mL). Neurons were entrapped in 3-D culture matrices of Matrigel (7.5 mg/mL; BD Biosciences) or SeaPrep agarose (1.5%; Cambrex) with or without collagen IV covalently crosslinked (0.3-0.6 mg/mL), as previously described (Cullen & LaPlaca 2006b). The cultures were 500 - 1000 μm thick at a final cell density of 3750 – 5000 cells/ mm^3 , were fed neuronal medium (Neurobasal medium + 2 % B-27 + 500 μM L-glutamine) and maintained in a tissue culture incubator (37 °C, 5% CO_2 , 95% humidified air).

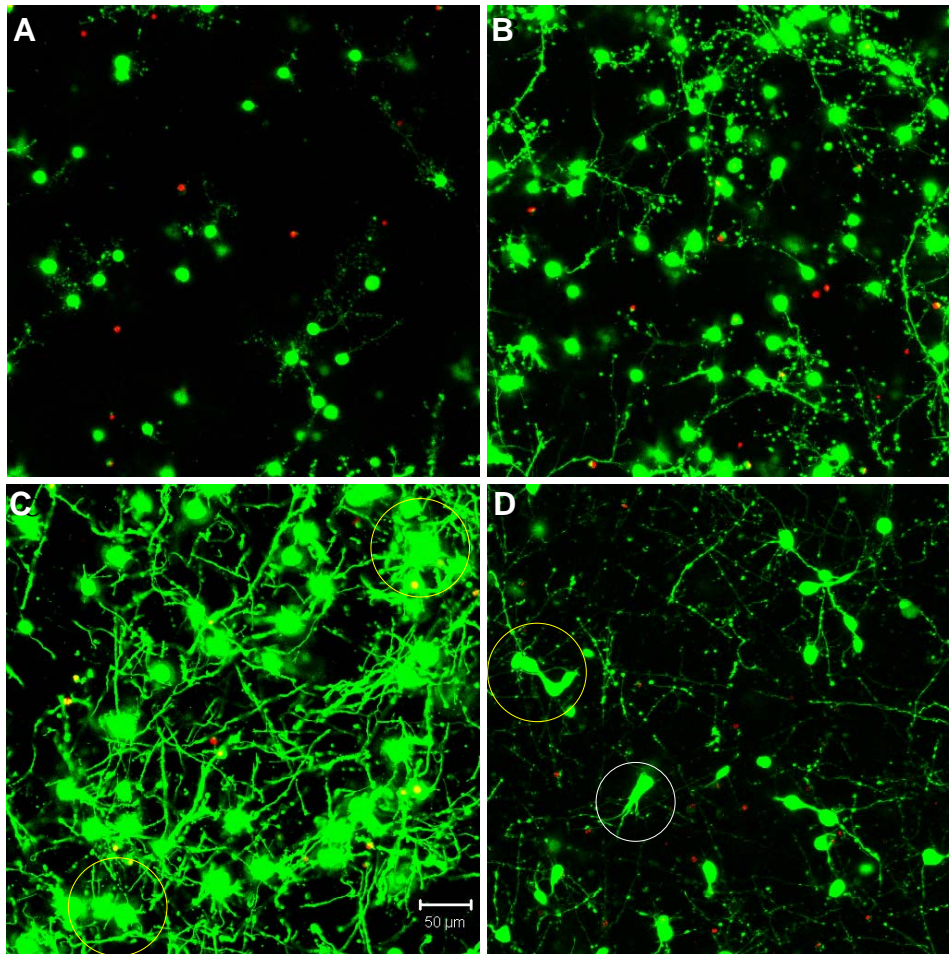


Figure 3.5: Image testing categories. Variation in testing conditions was achieved by dividing cultures into four categories based on culture complexity. Levels one through three consisted of mainly spherical neurons with increasing amounts of neurite outgrowth. Specifically, (A) level one had spherical neurons with few neurites and no cell clustering; (B) level two had mainly spherical neurons with increased neurite outgrowth and little clustering; (C) level three had robust neurite outgrowth with increased cell clustering (yellow circles). Finally, (D) level four had increased complexity due to more diverse, non-spherical neuronal morphologies (white circle), cell clustering (yellow circle), and significant neurite outgrowth. Images are 2-D reconstructions of confocal z-stacks (100 μm total thickness); scale bar = 50 μm .

Cells were labeled using fluorescent probes for distinguishing live and dead cells (LIVE/DEAD Viability/Cytotoxicity Kit; Molecular Probes, Eugene, OR). Cell cultures were rinsed in buffer and incubated with 2 μM calcein AM and 4 μM ethidium homodimer-1 at 37 $^{\circ}\text{C}$ for 30 min and rinsed in PBS. After viability/cytotoxicity

staining, cells were viewed using a Laser Scanning Confocal Microscope (Zeiss 510, Oberkochen, Germany, 1 photon mode). Multiple z-stacks (5 - 20 μm plane-to-plane separation) were acquired from the different culture conditions, and were exported as AVI files with 512x512 pixels (per frame) and 24-bit color depth.

3.2.4.2 *Defining the 'Gold Standard'*

The automated segmentation routines were tested on sixteen confocal z-stacks that were divided into four categories of culture complexity, based on the assumption that increasing complexity in neuronal morphology and neurite outgrowth (network formation) would correspond with increased difficulty in accurate image processing and hence require more complex algorithms to minimize error. All levels utilized 3-D cultures of primary cortical neurons homogeneously distributed throughout thick ($>500\ \mu\text{m}$) matrices. The variables distinguishing the culture parameters were matrix type (ranging from bioactive collagen-laminin to relatively bio-inert agarose; influencing neuronal morphology), cell density/clustering (causing overlapping somata), and amount of neurite outgrowth (a function of matrix permissiveness; influencing amount of signal not related to cell soma counts) (Figure 3.5). The first three categories (of four) utilized agarose as the matrix material, and resulted in the maintenance of a spherical or near-spherical neuronal morphology. The difference in levels 1, 2, and 3 are due to the amount of neurite outgrowth and resulting cell clustering. Specifically, level 1 represented a baseline with spherical neuronal morphology throughout culture, relatively low cell density (i.e., little clustering), and demonstrate a paucity of neurite outgrowth. Level 2 cultures had a moderate increase in neurite outgrowth, with similar cell density and spherical morphology as level 1. Level 3 cultures demonstrated extensive neurite

outgrowth with an associated increase in cell density. Alternatively, level 4 cultures were developed within a bioactive collagen-laminin matrix, which neurons were able to actively remodel and thus may assume a variety of complex *in vivo*-like (e.g., non-spherical) morphologies. Level 4 cultures also demonstrated significant neurite outgrowth, and although these cultures had a moderate cell density, there was cell clustering in some cases. These descriptions are summarized in Table 3.1.

Table 3.1: Description of 3-D neuronal culture parameters by category number

	Soma Morphology	Neurite Outgrowth	Cell Clustering
Level 1	Spherical	Low	Low
Level 2	Spherical	Medium	Low
Level 3	Spherical	High	Medium
Level 4	Complex	High	Medium

The same set of software tools that enabled automated segmentation with click-and-correct edits were used for an altogether different method of cell segmentation: software-assisted *manual* segmentation. For this application, the 2-D automated segmentation routines were executed (without 3-D merging routines) to record the indices of *potential* cells. In order to prevent biasing the user, visual feedback was suppressed, and the user clicked on individual cells in each 2-D frame to indicate which objects were cells. The index of the user's click was compared against a 2-D database of potential cells; if a match was found, the automated segmentation boundaries of the potential cell were displayed. Click commands selected or de-selected the cell, provided an alternative (non-watershed based) segmentation boundary, or allowed the user to manually segment the cell. As the user moved between frames, 3-D merge and split

operations were automatically performed, and visual feedback was provided to indicate the relationships of cells between frames. This method of software-assisted segmentation allowed us to manually build a collection of test images with which to evaluate our automated routines. For each image evaluated, skilled technicians carefully identified each cellular object in both 2-D and 3-D.

3.2.4.3 Validation Methodology and Statistical Analysis

For validation of software performance, the total cell count, number of false positive cells, and the number of false negative cells were recorded at various stages in the routine. The accuracy and error percentage were calculated in comparison to manual counts attained by experienced technicians. We chose a conservative validation approach to analyze the total error present at various stages of the algorithm. Specifically, the error analysis was based on the total error percentage, defined as the percentage error based on the sum of the number of false positives plus the number of false negatives (calculating accuracy based purely on count output may artificially raise performance since false positives and false negatives can potentially cancel out). Two-way repeated measures general linear model ANOVA was performed with culture complexity (i.e., level 1-4) as an independent variable, sub-routine point as the repeated variable, and count accuracy, false positive (%), false negative (%), and total error (%) as dependent variables. When significant differences existed between groups, Tukey's pair-wise comparisons were performed. For all statistical tests, $p < 0.05$ was required for significance. Data are presented as mean \pm standard deviation.

3.2.4.4 *Validation Results*

In order to assess the fidelity of the algorithms, automated software segmentation boundaries were compared to the software-assisted manual segmentation. Specifically, the results of the automated routines were evaluated without 3-D error correction, with 3-D error correction, and following manual correction of software-defined probable errors (manual correction was only allowed if the software flagged a potential error; in other words, errors that were not flagged by the software, but were otherwise obvious to the tester, were ignored). At each of these stages, the following parameters were attained: (1) cell count, (2) over-counted cells (i.e., number of false positive cells), and (3) missed cells (i.e., number of false negative cells). Software defined probable error points were then manually assessed by experienced technicians and the appropriate action was taken (i.e., correction or no correction - although the vast majority of flagged errors required correction). The software quantification parameters (e.g., area threshold (α) and percent 3-D overlap (β)) were empirically optimized for only one image-stack in each level, thus the same settings were maintained within each level to demonstrate robustness of the system. This multi-level analysis permitted assessment of the value of 3-D error identification and user-driven correction in reducing error and enhancing the accuracy of the routine output.

Table 3.2: Results

Level	Sample Number	Actual Number of Cells	Cell count before automated error correction			Cell count after automated error correction			Cell count after correction of software identified probable errors		
			count	false+	false-	count	false+	false-	count	false+	false-
1	01	26	27	2	1	25	0	1	25	0	1
	02	29	29	0	0	29	0	0	29	0	0
	03	28	26	0	2	26	0	2	26	0	2
	04	37	39	3	1	37	1	1	36	0	1
			mean error (%) =	4.0	3.4	mean error (%) =	0.7	3.4	mean error (%) =	0.0	3.4
			stand. dev. (%) =	4.6	3.0	stand. dev. (%) =	1.4	3.0	stand. dev. (%) =	0.0	3.0
2	01	42	42	0	0	42	0	0	42	0	0
	02	66	68	2	0	68	2	0	66	0	0
	03	65	71	6	0	68	3	0	65	0	0
	04	52	54	4	1	51	1	1	51	0	1
	05	135	144	9	0	140	5	0	137	2	0
			mean error (%) =	5.3	0.4	mean error (%) =	2.7	0.4	mean error (%) =	0.3	0.4
			stand. dev. (%) =	3.8	0.9	stand. dev. (%) =	1.8	0.9	stand. dev. (%) =	0.7	0.9
3	01	36	39	3	0	37	1	0	37	1	0
	02	54	50	0	4	50	0	4	51	0	3
	03	86	96	10	0	96	10	0	88	2	0
	04	87	86	2	3	85	1	3	86	1	2
			mean error (%) =	5.6	2.7	mean error (%) =	3.9	2.7	mean error (%) =	1.6	2.0
			stand. dev. (%) =	5.4	3.5	stand. dev. (%) =	5.3	3.5	stand. dev. (%) =	1.2	2.6
4	01	36	39	5	2	35	1	2	34	0	2
	02	27	28	3	2	27	2	2	25	0	2
	03	48	49	3	2	46	0	2	47	0	1
			mean error (%) =	10.4	5.7	mean error (%) =	3.4	5.7	mean error (%) =	0.0	5.0
			stand. dev. (%) =	3.9	1.6	stand. dev. (%) =	3.7	1.6	stand. dev. (%) =	0.0	2.7

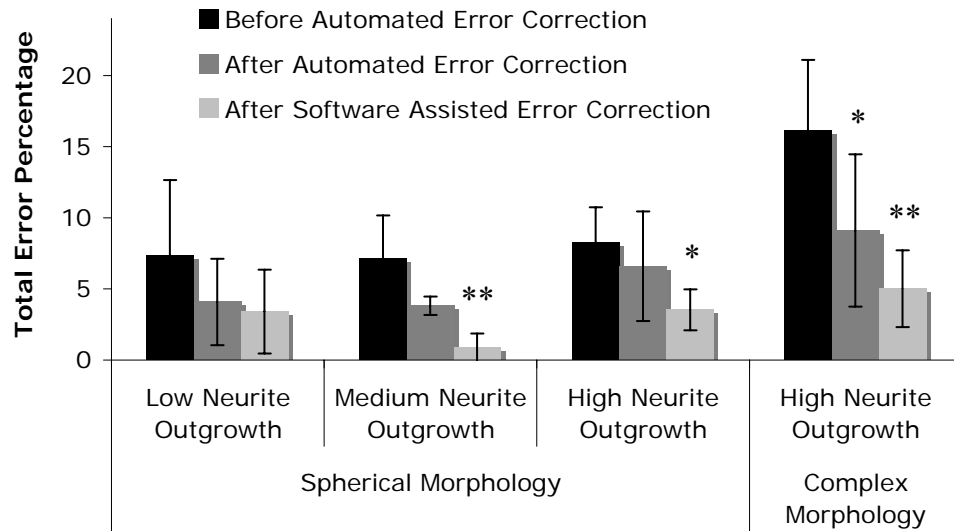


Figure 3.6: The total error percentage, defined as the number of false positives counts plus the number of false negative counts in comparison to the actual number of cells, was calculated for levels one through three (spherical morphology with increasing levels of neurite outgrowth) and level four (complex morphology with high neurite outgrowth). Two-way repeated measures ANOVA revealed that the total error was reduced by the presence of automated error correction ($p < 0.001$), and was further reduced by correction of software-identified probable error points ($p < 0.05$). Tukey's post-hoc pair-wise comparisons revealed significant error reduction within levels two through four; asterisks denote significant reduction in total error percentage versus "Before Automated Error Correction" within each level (* $p < 0.05$; ** $p < 0.01$; *** $p < 0.001$).

Fully automated and user-corrected quantification were compared to manually-attained cell counts in order to assess the overall accuracy and error sources of the software. The results are tabulated in Table 3.2, depicting the raw counts for the different points of the sub-routine in addition to the false positive and false negative counts (including error percentages). Analysis of the total error percentage (based on false positive cells plus false negative cells) was found to be a sensitive measure of software performance. The total error percentage was found to depend significantly on level/category assigned to the cell culture ($p < 0.05$), sub-routine point ($p < 0.001$), with no interaction between these factors. Overall, the application of 3-D error correction significantly reduced the total error percentage ($p < 0.001$ for each) (Figure 3.6). Additionally, there was a significant reduction in the total error percentage when software-assisted error correction was applied following automated 3-D error correction ($p < 0.05$). Pair-wise comparisons within the four cell culture levels clearly demonstrated the importance of 3-D segmentation and error correction as culture complexity increases. However, such analysis techniques did not significantly improve performance in relatively simple samples (level 1) where somata assume spherical morphologies and bear few or no processes, thus underscoring the niche application of these software algorithms in complex 3-D neurobiological applications.

3.3.4.5 Sensitivity to User-Defined Parameters

To investigate the influence of parameter selection on the accuracy of the segmentation routines, we examined cell count errors as a function of the area classification criteria, α , and intensity threshold, T , for a level 2 test image. The area threshold was normalized to one standard deviation less than the mean of the cell bodies

(i.e. $100\% = \text{Mean}(\text{cell bodies}) - \text{StdDev}(\text{cell bodies})$), and the parameter was swept from 15% to 100%. The intensity threshold was swept from 35% to 100% of the maximum pixel intensity. Error was defined as the percent deviation of the automated cell count from the ‘gold standard’ cell count, and was tabulated for the segmentation algorithms run both with and without automated 3-D error correction.

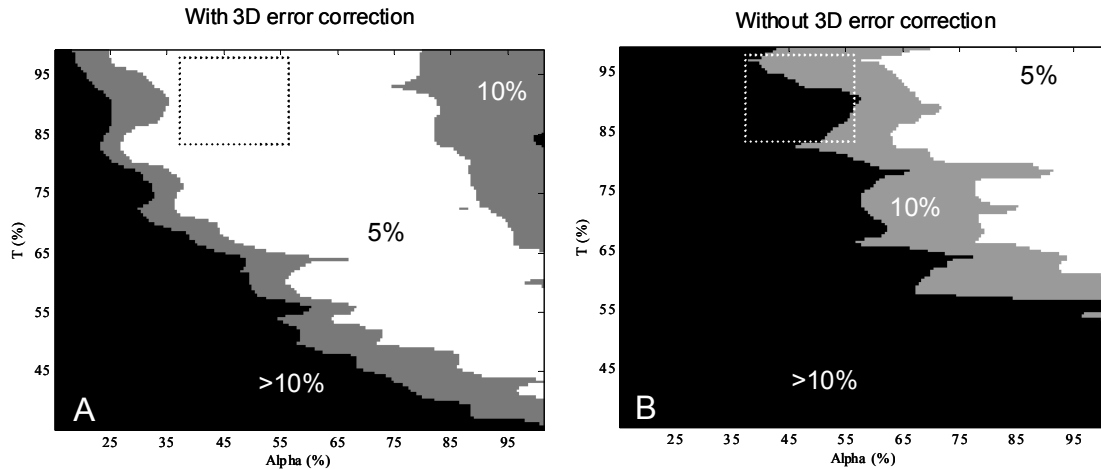


Figure 3.7: Sensitivity to user-defined parameters. Cell count error as a function of α and T both with (A) and without (B) 3-D error correction. The dashed box indicates the region of parameters an operator would likely select based on histogram data from the software. In (A) the 5% error region occupies 44% of the shown parameter space; in contrast, the same error region occupies only 18% of (B). In (A), the removal of neurite segments and the merging of over-segmented somata accounts for the reduced sensitivity to user defined parameters.

Figure 3.7 depicts error as a function of the user-defined parameters, α and T (the dashed-box indicates parameters that were most likely to be manually selected based on histogram feedback provided by the software, for example, refer to Figure 3.2). In general, the automated cell count decreased as the thresholds were increased. Therefore, without 3-D error correction, the cell count was artificially raised by the inclusion of over-segmented somata and neurite fragments. Figure 3.7 demonstrates that using 3-D context clues to identify and correct segmentation errors generates a much more robust

parameter space with which to achieve accurate cell-count results; thus, future versions of the software may be able to automate parameter selection.

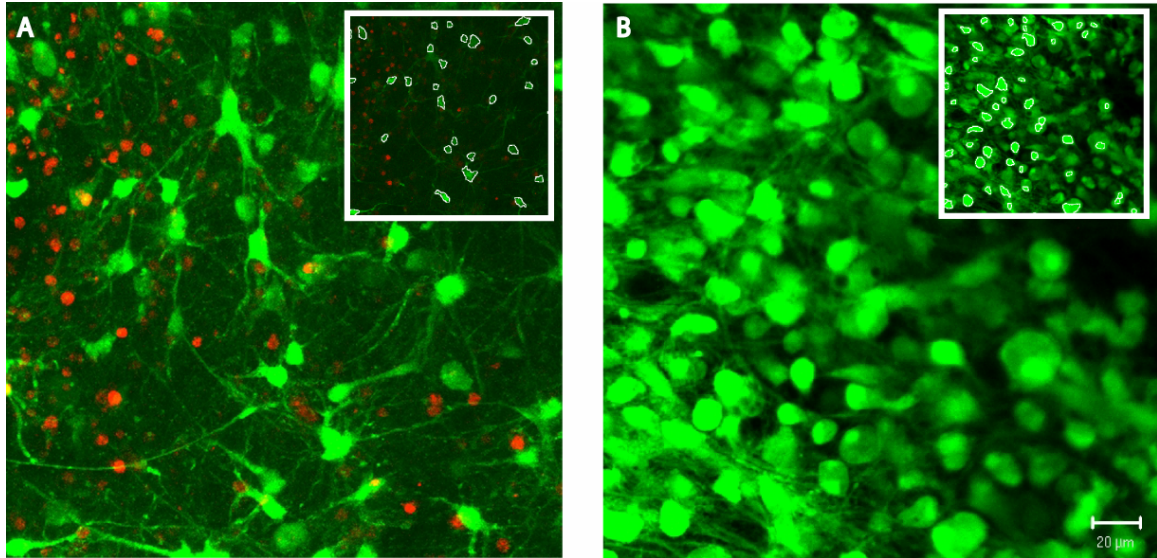


Figure 3.8 Demonstration of system robustness: soma segmentation in ex vivo brain tissue. Custom 3-D segmentation algorithms were applied to z-stacks attained from confocal imaging of brain slices from cerebral cortex. The z-stacks tested varied based on the density of viable cells, ranging from relatively low (A) to high (B) densities. Following the same protocol of the in vitro testing, the algorithms achieved accuracies of 93% (A) and 97% (B) ($\alpha = 50$, $\beta = 0.15$, $T_A = 80\%$, $T_B = 95\%$).

3.3.4.6 Performance Validation in Brain Slices

In addition to 3-D *in vitro* cultures, the image processing algorithms can also be applied to 3-D *ex vivo* brain slices. As a demonstration of system robustness, the algorithms were tested on confocal z-stacks acquired from cerebral cortical brain slice cultures. We choose samples with varied densities of viable cells, ranging from relatively low to high densities (Figure 3.8). The z-stacks tested also varied based on range of morphologies and the contrast in cell features (e.g., cell pixels ranged from relatively faint, low intensity, to saturated, high intensity). Apart from the global intensity threshold, T , the user-defined parameters were identical for these two image stacks ($\alpha = 50$, $\beta = 0.15$, $T_A =$

60%, $T_B = 95\%$). Following the same protocols defined for the *in vitro* cultures, the software achieved 93% and 97% accuracies for the low and high cell density z-stacks, respectively.

3.3 Automated Tracking of Functional Activity

Although 3-D tissues and cultures would comprise the ideal platform for investigating stimulation waveforms, the tracking of functional activity in four dimensions (3 spatial dimensions and time) would require developments in image acquisition speed that are beyond the scope of this work. Therefore, in this section, we compromise by building on the 2-D segmentation algorithms of section 3.1 to enable semi-automated, high fidelity and high-speed tracking of 2-D cellular activity.

In the previous sections, we presented algorithms that were successful in identifying the location of individual cells using static fluorescence signals. Here, we examine optical movies in which changes in fluorescence intensity are correlated to specific cellular processes (e.g. ion uptake, channel dynamics, etc.). In order to evaluate these ‘movies’, we developed signal-processing tools that made it possible to examine both the location and behavior of the cells under observation. Although there are many signal processing algorithms for tracking global changes in fluorescence activity, few if any routines can identify and evaluate every cell within a complex, high-density culture.

Tracking the activity of thousands of individual neurons, however, is a computationally demanding problem. Fortunately, this problem becomes manageable for studies in which the signals of interest are tied to an externally induced event. In this case, a priori knowledge of when a change is expected can be applied to significantly reduce the computation required for the analysis. For example, if the peak response time

to external stimulus is known, it becomes possible to rapidly (1) identify the location of stimulated cells and (2) measure the dynamics of the individual responses. Figure 3.9 illustrates the application of difference imaging to the automated identification stimulated cells.

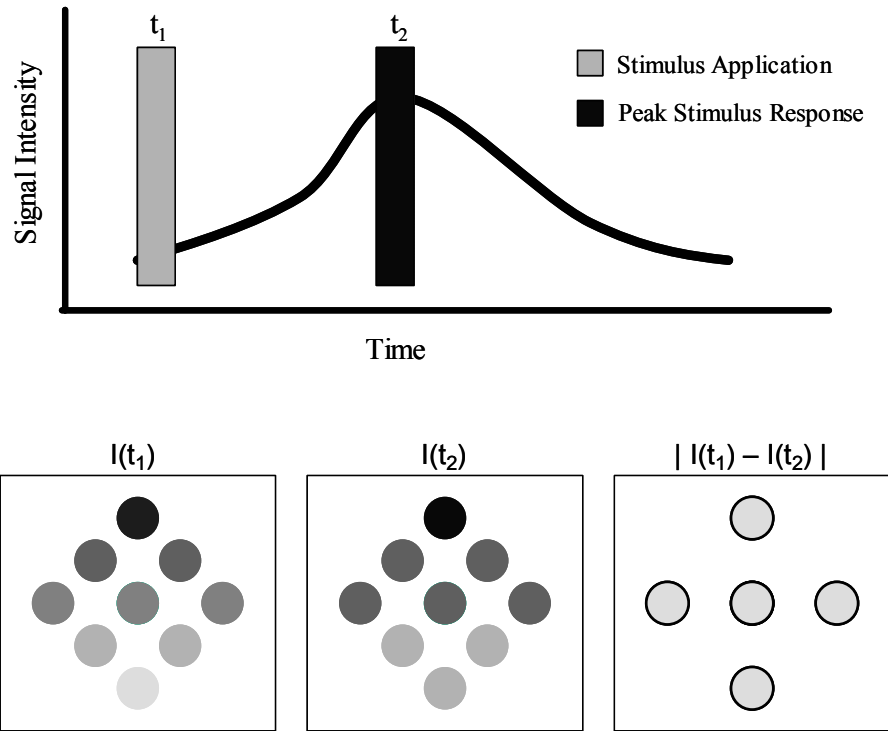


Figure 3.9 Tracking evoked behavior. A priori knowledge about the cellular response to an externally applied stimulus can be used to rapidly identify stimulated cells. (A) An image captured before the application of the stimulus (t_1) can be subtracted from an image captured during the peak response (t_2). This so-called difference image is illustrated in (B). Images captured at two points in time, t_1 and t_2 , look very similar. However, subtracting the two images clearly identifies the objects that changed. Image segmentation routines can be applied to the difference image to automatically identify the boundaries of changed/stimulated objects (black outlines).

With the concept of difference imaging in mind, we can use the same algorithms of section 3.2 to identify stimulated neurons with only two additional preprocessing steps: (1) formulating the difference image, and (2) applying non-linear intensity transforms to enhance contrast. Following the *identification* of excited cells, it becomes

relatively straightforward to *track* the full fluorescence waveform corresponding to the stimulus event. Figure 3.10 summarizes the process used to identify and track externally stimulated tissue.

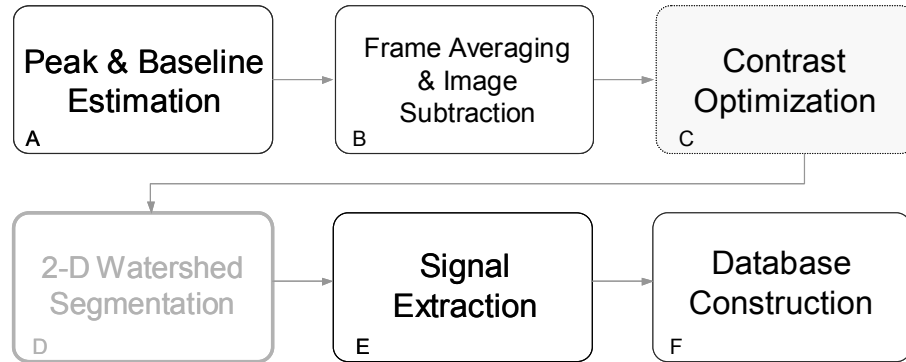


Figure 3.10: Process flow for tracking evoked in 2-D cultures. (A) Estimations for peak and base-line activity are used to identify the frames used in image subtraction in (B). Simple optimizations can be used to determine the true peak response. (C) Optional: Non-linear intensity transforms are applied to the difference-image to enhance contrast in preparation for object segmentation. (D) The 2-D segmentation and classification algorithms of section 3.1 are used to distinguish somata from ‘illuminated’ neurites. (E) Following the identification of stimulated cells from the difference image, the full fluorescence waveforms are extracted and stored in a database (F) that relates the response to the stimulus parameters.

The processing steps schematically represented in Figure 3.11 were integrated into a MATLAB graphical user interface (GUI). Additionally, a myriad of software features including the click-and-correct algorithms of section 3.2.3 were implemented to facilitate the rapid and accurate assessment of stimulated cells and tissue. Figure 3.10A-C demonstrates the application of difference imaging and watershed segmentation to extracellularly stimulated 2-D cortical cultures loaded with Fluo-5F calcium dyes. The cultures were stimulated successively to elevate signal intensity through calcium accumulation (see section 4.1.2.4 for more details). Figure 3.11A illustrates difference imaging in practice, and Fig. 3.11B shows a screen shot of the final program. The blue trace shows the relative changes in fluorescent intensity for a selected cell outlined in red.

The full set of algorithms is capable of extracting functional waveforms from hundreds of cells in hundreds of movies in a few minutes. This greatly facilitates high-resolution investigations into evoked responses to extracellular stimuli.

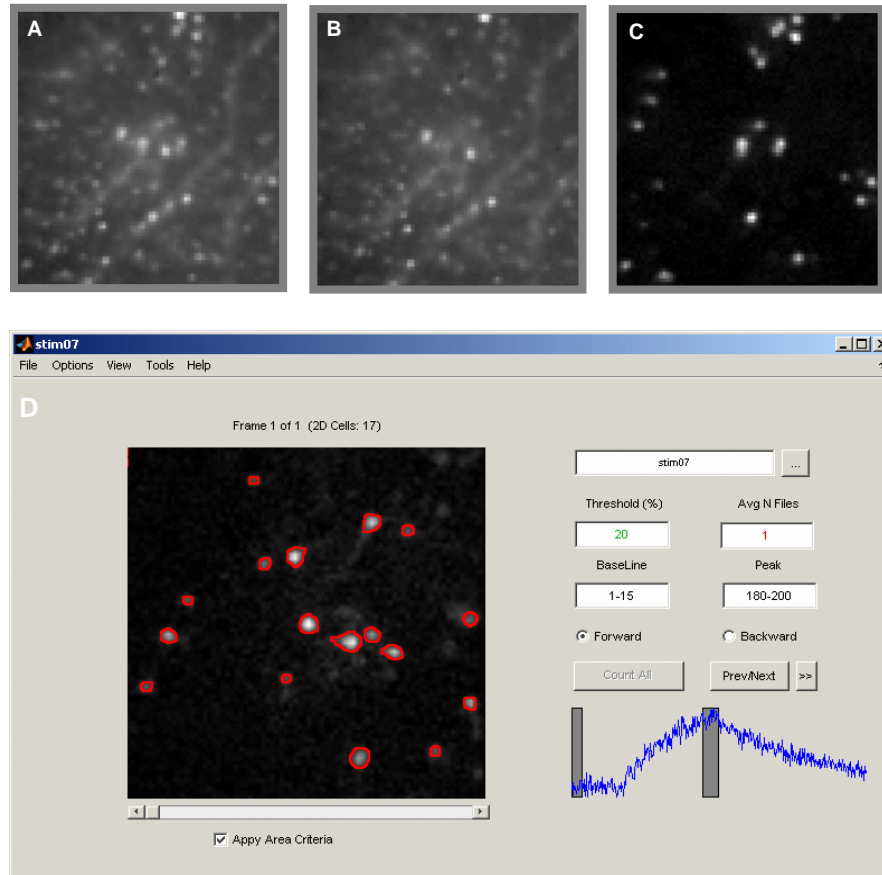


Figure 3.11: Functional image processing. (A) The image from the average of 15 frames measured before the stimulus event. (B) The image from the average of 15 frames at the anticipated peak of the response. (C) The difference image. (C) The image processing algorithms were written in Matlab (Mathworks, version 7.01) and integrated into a graphical user interface (GUI) that was designed to facilitate parameter selection, visual feedback, and user-guided edits. Shown in the figure is a difference image of 15 averaged frames measured at the peak of the response subtracted by 15 averaged frames at the base-line response (gray bars on the blue $\Delta f/f$ trace) The following features were incorporated into the GUI: (1) databases for maintaining cell coordinates and boundary information, (2) histograms and segmentation statistics for assisting parameter selection, (3) saving and reloading options for revisiting and revising image-movies, (4) computer assisted manual segmentation for error correction, (5) morphological operator and process selection for preprocessing, (6) idealized graphic reconstructions of segmented cultures, and (7) automated signal extraction for individual cells.

3.4 Discussion

We have demonstrated novel methodologies for the systematic and unbiased identification of neural cells distributed throughout 2-D and 3-D tissue or *in vitro* constructs. We utilized novel features, including neurite/soma classification, 3-D merging & segmentation error identification, and software assisted manual corrections, to attain highly accurate cell boundary identification over a wide range of morphological culture complexities. Further, we utilized the boundary identification algorithms to automatically identify and track dynamic cellular signaling. This toolset addresses a gap between automated segmentation routines for multi-cell *nuclear* images (with no neural processes present) and *single-cell* (or low density) images with rich morphological detail. Additionally, this toolset allows users to make rapid, computer-assisted manual corrections to the automated segmentation database, which is particularly attractive when highly accurate assessments of cell body locations must be made during a live experiment (e.g., optical tracking of network activity using Ca^{2+} -sensitive dyes). Moreover, we demonstrated that our algorithms leverage the increased complexity inherent in 3-D systems as an extremely effective means of minimizing quantification errors by applying the rich set of spatial data to automatically correct segmentation errors. This novel image analysis platform offers experimental neurobiologists and neuroengineers a valuable set of tools for the analysis of neural tissue or tissue surrogates, appropriate for the study of cell-cell and cell-extracellular matrix interactions.

We have validated these tools in the specific application of automated segmentation of neuronal somata with dense neurite arborization within 2-D and 3-D constructs. Despite a conservative validation scheme, the algorithms performed very

well for a variety of 3-D test images (which inherently involves 2-D processing), with an accuracy $\geq 95\%$ over a wide range of morphological culture complexities. During the validation process, users were not allowed to correct unmarked errors that were otherwise obvious to the investigator. Thus, the accuracy of the presented algorithms is expected to approach 100% in practical applications.

We have addressed the challenge of parameter selection by taking measures to insure that the process parameters were relatively easy to tune. The empirically derived operator variables that influenced the performance of the segmentation routines included (1) the pixel intensity threshold, T , (2) the soma/neurite area threshold, α , and (3) the 3-D merging overlap percentage, β . The area and intensity parameters, α and T respectively, were assigned based on histograms generated by the software. The overlap percentage, β , was used primarily to specify the sensitivity of the software to segmentation errors. Although careful tuning of the parameters certainly improved performance, the accuracy of the software was relatively robust to changes in these parameters (as indicated in Figure 3.8), which indicates that automated parameter tuning may be feasible in future work.

One of the challenges in image segmentation is to define a metric for object classification. In order to optimize performance (speed and accuracy), we chose to distinguish between neurite fragments and somata using very simple criteria - object pixel area. Although area thresholds have been reported in the past to separate *nuclei* from *artifacts* (Adiga 2000), we have shown that watershed segmentation produces boundary areas with remarkably distinct populations for *neurites* and *somata*. Despite the efficacy of this method, inevitably some cell body objects were excluded while some neurite

fragments were included. The 3-D merging algorithms all but eliminated this problem. For example, objects which only appeared in a single frame were assumed to be artifacts or neurite fragments and were removed. Furthermore, the exclusion of cell bodies (false negatives) usually occurred near the soma edge in the z-axis where the soma cross-section possessed a very small 2-D diameter; in this case, the cell was usually represented in neighboring frames, where confocal slices captured a larger 2-D perspective of the cell (a typical cell occupied 3 to 6 frames in our application, although this will be a function of confocal microscopy parameters). In the absence of 3-D context cues, 2-D studies still benefit from highly accurate boundary identification (typically > 90%) and from semi-automated click-and-correct software tools.

We have developed novel techniques for merging 2-D objects into 3-D *somata* and identifying 2-D segmentation errors. These techniques improve on methods by (Belien 2002; Irinopoulou 1997) to merge 2-D objects into 3-D *nuclei*. Specifically, we introduced (1) criteria to evaluate cell mergers from multiple vantage points and (2) methods to identify potential segmentation errors. Previous techniques only considered the forward projection of 2-D nuclei into neighboring frames and could not recognize 2-D segmentation errors, thus opening up the possibility for more errors with no means to identify them. One novel feature of our 2-D to 3-D merging strategy is that it identifies both false positives (over-segmented objects) and false negatives (under segmented objects).

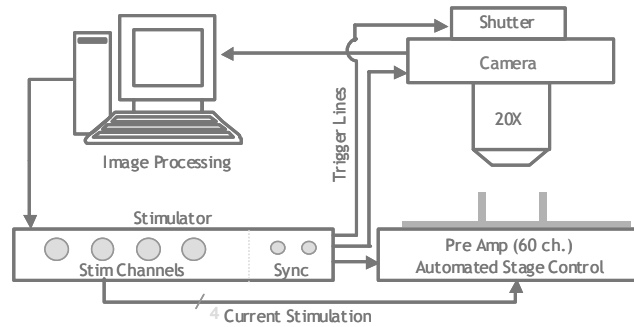
In the future, we plan to implement improvements to the merging algorithm. While our algorithm identifies both false positives and false negatives, we have no method in place to distinguish between these error types, nor do we have routines to

‘split’ under-segmented cells. Additionally, we only used two adjacent frames to determine if and how adjacent 2-D objects should be merged. In the future, it would be beneficial to use information from all overlapping 2-D objects (that typically traverse 3 or more frames) to arbitrate decisions about the error type (false positive, false negative) and the appropriate action (merge, split). One approach could use geometric statistics from local (only overlapping objects) and global (all 2-D objects) segmentation boundaries, along with an empirically derived cost function, to facilitate merging and splitting decisions. The method of applying a cost function to arbitrate merging decisions was demonstrated with great success (Lin 2003). By integrating this approach into our merging routines, we could automatically correct over- *and* under-segmented somata, thereby requiring less software assisted manual input.

Future applications of this software will include systems with increased densities of labeled cells (e.g., dense cortical regions in brain tissue or dense *in vitro* neural constructs) and the assessment of 3-D co-localization of multiple fluorescent labels. Although the presented methods were used exclusively to catalog information regarding somata, it is interesting to note that an investigator could use the knowledge of cell body boundaries to facilitate additional morphological analyses, such as quantifying the spatial extent and volume of neurite outgrowth. These algorithms are building towards automated four-dimensional analyses including temporal components over three spatial dimensions, such as 3-D cell migration. Ultimately, these tools may lead to 4-D real-time analysis of ensemble electrophysiological network behavior in neural tissue or constructs analyzed by tracing relative fluorescent intensity and/or signal propagation using voltage or ion-sensitive dyes.

CHAPTER 4

AUTOMATED CELLULAR TRACKING: ELECTRICAL STIMULATION AND OPTICAL MONITORING



In this chapter, the engineering tools of chapters 2 and 3 are combined with novel signal processing techniques to enable the high-throughput evaluation of selective stimulation waveforms. Willfully controlling the focus of an extracellular stimulus (i.e. selective stimulation) remains a significant challenge in neural engineering. In part, this is due to the fact that experimental validation of the evoked response to stimuli is an arduous and time-consuming task. The development of a high-throughput data acquisition and analysis tool greatly facilitates the design and testing of spatially selective stimulation protocols. Here, we present an automated imaging system that optically tracks and identifies the action potentials of individual neurons evoked by coordinated stimulus waveforms applied at multiple electrodes. This system can simultaneously provide arbitrary current waveforms to MEA electrodes and it is capable of automatically monitoring the cellular responses of *every* neuron in a cultured network within a $3 \times 3 \text{ mm}$ area. The purpose of this platform is to facilitate development of stimulus protocols that exploit the benefits of multi-polar field shaping and temporal ion-channel/membrane manipulation to explicitly control cellular excitation. Analyses of monopolar excitatory

and inhibitory waveforms are presented as well as performance data for the automated stimulus tracking system.

4.1 High Throughput Stimulus Tracking

Among the many challenges in designing spatially and functionally selective stimulus waveforms, is the inability to *experimentally* validate stimulation strategies. Although many advances in stimulation technology have been made with computational *models*, which despite providing a great deal of insight into the mechanisms, techniques, and strategies for selective stimulus waveforms, are seldom experimentally validated. Thus, it would be beneficial to develop an experimental system that approaches the throughput (and insight) of models.

Combining a functional imaging system with multielectrode arrays (MEAs), stimulating electronics, and live cultures creates an ideal platform for the high-resolution tracking of neural responses to extracellular stimuli (Tsien 2006). For example, optical imaging systems can record the action potentials of individual cells by monitoring the changes in internal cellular concentrations of fluorescent dyes (Smetters 1999).

Additionally, the tightly spaced grid of electrodes in MEAs can be simultaneously activated to sculpt the contours of voltage fields that surround neural tissue. Developing this platform, however, requires the integration of two very different components: (1) a biological component, which includes the cell culture, fluorescent dyes and pharmacological blockers, and (2) a hardware component, which includes the MEMs, optics, and electronics. In this section, we present the development and integration of these components for high-throughput optical monitoring of stimulus-evoked activity.

4.1.1 Biological Design

The primary, long-term objective of this study is to develop selective stimulation protocols for diagnosing and treating human nervous system disorders. Although in-vitro cultures are vastly less complex than the in-vivo human environment, in-vitro constructs capture virtually all of the behavior relevant to neural excitation and provide tremendous access/control over the neural environment (e.g. pharmacological manipulation, electrophysiological recording and stimulation, and high-resolution microscopic analysis, etc. (Potter 2001)). Therefore, as a first step towards stimulating human neural tissue in-vivo, we elected to use dissociated primary neuron cultures. In this section, we outline the biological methods used to evaluate in-vitro, extracellular stimulation, including neural culturing, dye labeling, and pharmacological conditioning (Dr. Potter and his research group significantly contributed to the biological design, specifically the neural culture techniques and synaptic blockers. Please see appendix C for more details on the protocols).

4.1.1.1 Neural Cultures

One of the most effective means to perform long-term extracellular electrophysiological investigations is to culture the neurons directly onto the microelectrodes. In this system, the culture conditions were specifically tuned to facilitate optical recordings of neural action potentials. For example, MEAs (Multi-Channel Systems, 30 μm diameter, TiN electrodes with 200 μm center-to-center spacing) were plated with high densities (approx. 3000 cells/ mm^2 diameter) to better emulate neural tissue and to increase the number of evoked responses in the dish. Although cortical cultures provide an excellent model for

neural stimulation studies, it is important to note that such cultures do not produce myelinated axons, which influence axonal excitation.

4.1.1.2 Fluorescent Ca^{2+} Dyes

Fluorometric Ca^{2+} imaging is a sensitive method for monitoring neural activity that makes use of the fact that, in living cells, most depolarizing electrical signals are associated with Ca^{2+} influx (Stosiek 2003). There are several properties of Ca^{2+} signaling that make it particularly useful for studying the evoked responses of stimulated neurons: (1) Ca^{2+} signals are often amplified by the intracellular release of Ca^{2+} stores (Tsien 1990; Berridge 2000), (2) the slow time constants of Ca^{2+} signaling enable further signal boosting through Ca^{2+} accumulation, (3) the slow time constants accommodate the relatively slow acquisition speeds of imaging systems, and (4) individual action potentials (up to 100 Hz) can be discerned from the calcium waveforms (Smetters 1999).

There are several calcium indicators whose fluorescence changes significantly (several percent of the resting fluorescence level, or $\Delta F/F$) as intracellular calcium concentration changes due to neural activity. The acetoxymethyl (AM) esters of these, in particular, are cell permeant, allowing them to become concentrated in living neurons where they are trapped by the action of esterases. Optimized protocols for bulk loading of AM Ca-indicators into neural tissue (Stosiek 2003; Yuste 2005) have enabled the simultaneous imaging of calcium transients in hundreds of neurons (Cossart 2003; Göbel 2007). Care must be taken when selecting a Ca^{2+} dye and stimulus protocol to insure that the binding affinity of the dye to the Ca ions does not influence intrinsic Ca^{2+} dynamics. In this study, optical recordings were accomplished using Fluo-5F, an acetoxymethyl-ester fluorescent calcium dye (Minta 2006), which has a binding affinity of $K_d \sim 2.3 \mu\text{M}$.

Cultures on MEAs were prepared for imaging by bath application with Fluo-5F AM for 35 minutes.

4.1.1.3 Pharmacological Synaptic Blockers

The calcium fluorescent dyes of the previous section enable the optical evaluation of *all* network activity. Rather than evaluating *network* activity, of particular interest to this study is the ability to evaluate *evoked* activity. Given the complexity and volume of spontaneous neural activity that occurs in dense dissociated cortical cultures (Wagenaar 2006), distinguishing evoked and spontaneous activity could be challenging for an automated system.

In order to inhibit network activity and to ensure that any measured activity was the direct consequence of an extracellular stimulus, synaptic blockers were added. Specifically, experiments were conducted in the presence of fast synaptic receptor antagonists at concentrations of 50 μ M BMI, 100 μ M APV, and 10 μ M CNQX (Sigma). At these concentrations, virtually all spontaneous neural activity was eliminated (Bakkum 2007). However, while these pharmacological agents prevent synaptic transmission between neurons, they have no effect on glial calcium signaling. Fortunately, glial and neuronal calcium waveforms are significantly different, so as to be easily distinguished by signal-processing methods.

The application of synaptic blockers to insure that all recorded *neural* activity was evoked, rather than spontaneous, greatly simplified our automated analysis routines. Additionally, the prevention of synaptic plasticity mechanisms insured that changes in cellular excitation were more generally related to the stimulus waveforms and not to inadvertent synaptic manipulations such as long-term potentiation (LTP).

4.1.2 Hardware and Software Design

The design of stimulus protocols for region specific neural excitation using both multipolar field shaping and temporal ion-channel/membrane manipulation requires hardware that can (1) deliver arbitrary current waveforms to multiple electrodes and (2) monitor the cellular activity of every neuron within a specified area. For the first requirement, we use an MEA, which can apply stimuli to multiple electrodes (with 30 to 200 μm spacing), such that field contributions from multiple sources could be summed in a manner that meaningfully alters the field contours. For the second requirement, we use a high-speed fluorescence imaging system (125 Hz to 2 KHz frame rate), which can record changes in intracellular calcium levels. The integration of these components as well as details on the automation of stimulus application, recording acquisition, and image analysis are presented in detail in this section.

4.1.2.1 System Overview

The system hardware, at its core, is comprised of four main elements: (1) a personal computer to control the instrumentation and analyze images, (2) a stimulator to produce arbitrary current waveforms and synchronize instrumentation activity, (3) an MEA system to interface the neurons, and (4) an optical acquisition system to monitor and record cellular activity (Figure 4.1). In order to support these core elements, additional instrumentation and software was required to control the light source, microscope stage, and high-speed camera (Table 4.1 gives an overview of the system specifications). The system was designed to enable a wide range of configurations for simultaneous optical and electrical observation of cells; as a result, many of the system components can be arbitrarily controlled with custom scripts that are executed on the

main computer (Mr. Nakul Reddy contributed substantial effort to the software development integration of the hardware.)

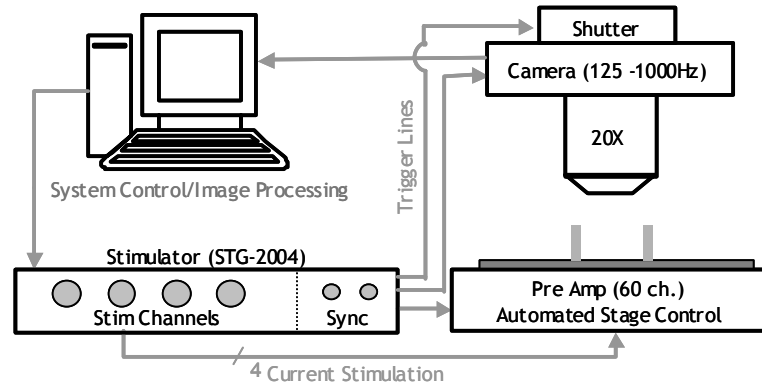


Figure 4.1 System level schematic of stimulus tracking system (Counter clockwise from top left) Matlab scripts specify stimulus sequences and synchronization pulses that are transferred via USB to an arbitrary waveform stimulus generator (Multichannel systems, STG-2004). A software trigger engages the stimulus generator, which applies the current waveforms to electrodes in an MEA docked in a recording preamplifier (Multichannel systems, MEA-1060). In total, four independent trigger pulses can be used to synchronize activities among the shutter, camera, stimulator, and preamplifier. Automated stage positioning (Intelligent Imaging Innovations, MS-2000) enables precise, arbitrary stage positioning. Following optical recording of the evoked response of the stimulus sequence, a new stimulation sequence is transmitted to the stimulus generator and the process is repeated. Although the present system runs open-loop scripts to vary the stimulus input and record evoked responses, automated image processing routines present an opportunity to implement closed loop control in the future.

Table 4.1: System Specifications

Component	Cntrl*	Manufacturer	Specifications
Objective		Zeiss	20x /NA: 0.92
Light Source		SNT	Tungsten, 100W
Shutter	X	Uniblitz	VMM-D1
Camera	X	Red Shirt	80x80 pixel, 125Hz - 2Khz fps
Stage	X	IIS, MS-2000	0.1um x,y resolution
Stimulator	X	MCS STG-2004	4 ch (20μV, 1μA, 10 μs res.), 4 trig
PreAmp	X	MCS 1060-BC	60 ch, 1200x gain, Stim Select (2 ch)
Heater		MCS 10R0X	2 ch, 0.1° Celcius
MEA		MCS 30/200	30 μm TiN Electrode, 200 μm Centers
Computer	X	DELL Inspiron	2 Ghz, Pentium IV
Image analysis	X	MATLAB 7.01	GUI: 250 fps, auto error, Ica extraction
System Control	X	MATLAB 7.01	GUI: Script Interpreter, Auto sync

* Indicates arbitrary control using the custom scripting language

4.1.2.2 Stage Control

A stimulation pulse produces voltage fields that influence cells beyond the 400x 400 μm area of a 20x microscope objective. Therefore, in order to evaluate the full scope of the evoked response, it may be important to record activity beyond the field of view. Unfortunately, the need for a low-resolution, high-speed camera (80x80 pixels) prevents the use of a lower power objective (5x, 10x, etc), so a compromise must be made between the resolution required for image analysis and the area needed for observation. An alternative solution, however, is to use high-resolution stage control to arbitrarily adjust the field-of-view.

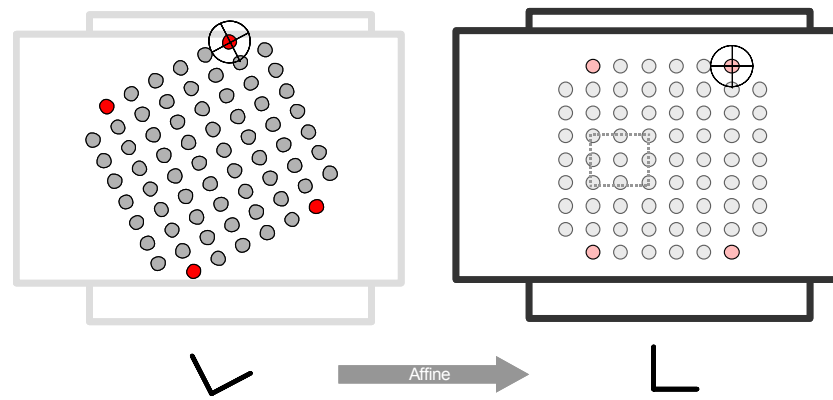


Figure 4.2 Automated stage displacement. Electrode coordinates were mapped to stage displacements by measuring the stage coordinates when the microscope was manually positioned over four corner electrodes. An affine transformation related electrode coordinates into stage displacements. Arbitrary control of the stage (to within 2 μm), enabled observation of the cellular response well outside of the 400 x 400 μm field of view (20x objective).

Automated stage positioning was accomplished by using a coordinate system that was directly related to the electrode coordinates. Stage displacement measurements were recorded in software while the microscope was manually positioned over the center of

four corner electrodes in the MEA. These measurements were used to create an affine transformation that related electrode-centric coordinates into stage displacements, thus compensating for any rotation or scaling due to skewed electrode arrangements or stage positioning. With this method and electrode coordinate system, we were able achieve automated field-of-view positioning to within 2 μm (Figure 4.2).

4.1.2.3 Experimental Sequencing

In order to insure that the optical tracking system was both flexible (i.e. arbitrary control over the system variables) and robust (i.e faithful acquisition of strong fluorescent signals), a sequencing formula was derived to execute the program in three stages: (1) manipulation of the field of view, (2) programming and trigger queuing, and (3) synchronized triggering. Each of these distinct phases can be activated recursively, for example, to apply triggered averaging or to rapidly change the field of view. Figure 4.3 illustrates the sequencing formula.

An example experimental protocol following this sequence could be as follows: The field of view is centered is at electrode 1.5, 1.5 (r,c). For each stimulation sequence, 250 frames are acquired at a frame rate of 125 frames/second (2 seconds total), of which the first 30 frames (240 ms) are used to record pre-stimulus, baseline fluorescence. The system pauses for 4 seconds between stimulus applications to allow accumulated calcium to decay back to baseline and either repeats the triggered sequence or re-programs the instruments for a new sequence. A typical experiment, under these conditions, could last approximately 90 to 120 minutes before dye photo-bleaching significantly diminished the signal-to-noise ratio. As a result, the evoked responses of over 1000 stimulation sequences can be recorded in a single session.

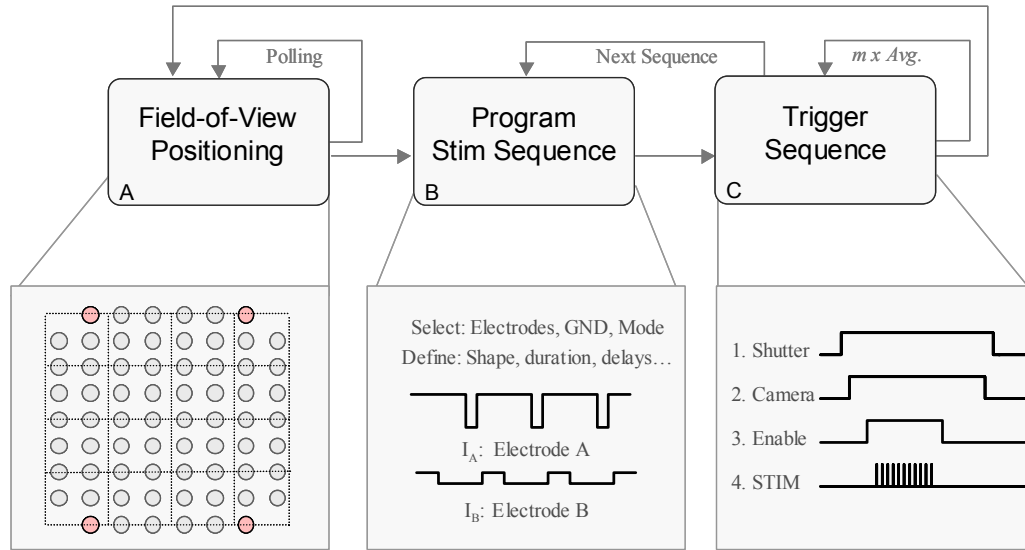


Figure 4.3 Sequencing formula for stimulus application and synchronized optical monitoring of evoked activity. (A) The microscope is positioned over the array using an electrode-based coordinate system. A typical 8x8 array, with 200 μm center-to-center electrodes, could be observed with approximately 16 separate stage displacements (indicated by dashed lines). (B) The stimulation and optical monitoring instruments are programmed and queued for triggering, which includes selecting the electrodes and specifying the arbitrary stimulus waveforms. (C) The shutter, camera, and stimulus system are triggered in sequence (the optional electrical MEA recording system may be triggered as well). The timing is managed such that camera captures both base line and recovery activity.

4.1.2.4 Signal Conditioning and Data Extraction

Because the acquisition and analysis of our experimental data is automated, it is essential that evoked responses be consistently recorded with high signal-to-noise ratios (as strong signals are more reliably detected by software). Therefore, the following steps were taken to enhance the signal: (1) calcium accumulation was induced by repeating stimulation patterns n times with 50 to 100 ms inter-stimulus intervals, (2) n -shot stimulation sequences were repeated m times to allow for triggered averaging, (3) stimulated soma were identified/segmented in an averaged difference image, and (4) fluorescent intensity traces for pixels that corresponded to an individual soma were

spatially averaged. Fig. 4.4 illustrates the steps taken to maximize the fluorescent signals.

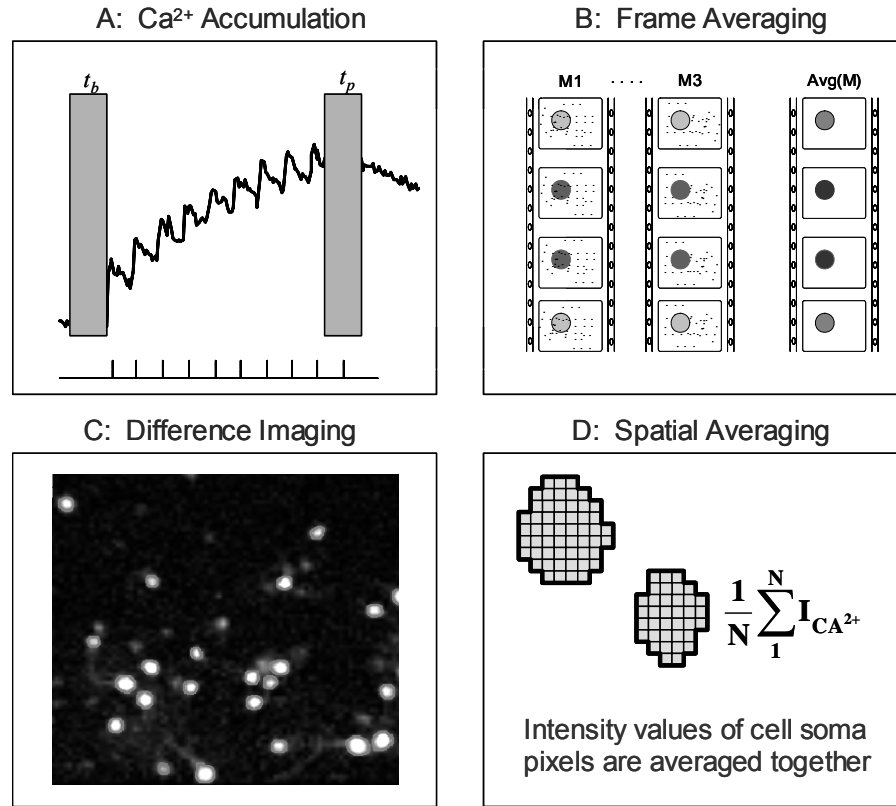


Figure 4.4 Maximizing Signal-to-Noise. Signal processing techniques for evaluating evoked-response patterns. (A) Stimulation waveforms are repeated n times (10 shot illustrated) with 50 - 100 ms inter-stimulus intervals (optimized based on Ca^{2+} signaling decay). (B) This n -shot stimulus sequence is repeated m times to further enhance the signal with triggered averaging. Subtraction of t_b averaged frames of base-line activity from t_p averaged frames at the peak of Ca accumulation (gray bars), produces high contrast images like the one shown in (C). Automated image segmentation routines are used to identify the cellular boundaries of each stimulated soma (gray outlines indicate soma boundaries), which facilitates spatial averaging (D) and quantification of stimulus-induced changes in evoked action potentials.

The identification of individually stimulated somata (Fig. 4.4C) is critical for detailed investigations into stimulus activity. In this system, each stimulated soma is automatically segmented in a difference image formulated by subtracting t_b averaged frames, taken just before stimulation, from t_p averaged frames, taken at the peak of

calcium accumulation (averaged frames are indicated with gray shading in Figure 4.4A). This background subtraction method produces a high contrast image of stimulated somata, which can be automatically segmented. Briefly from section (3.1), automated segmentation of stimulated somata was achieved by: (1) applying a global threshold to convert the gray-scale image into a binary image, (2) applying the Euclidean distance transform to shape the image contours and define the regional minima, (3) applying the watershed algorithm to delineate boundaries between overlapping cell bodies, and, finally, (4) applying an empirically determined threshold to removed segmented artifacts and neurites (note: given the high contrast images and neurite filtering, morphological pre-processing steps are seldom required).

Once the cells are segmented, it becomes possible to extract the full spatially-averaged calcium waveform for each soma (including extracting data from frames in which difference imaging would not provide sufficient contrast to ‘illuminate’ the cell bodies). While this data extraction must be performed for every stimulus condition, it is not necessary to segment somata in every stimulation trial. The pixel indices that correspond to stimulated somata during a control pulse (or a stimulus pattern designed to stimulate all neurons within the field of view, such as a high-amplitude, long duration biphasic voltage pulse), can be projected onto other test conditions to evaluate changes in evoked responses. In this system, software routines were written to quickly scroll between difference images (for a given field-of-view) from varying stimuli to insure that all somata had been accounted for.

In addition to signal conditioning, it is important to account for noise-inducing phenomena such as photo-bleaching, a process in which the fluorescent molecules are

destroyed by the light exposure necessary to stimulate them into fluorescing. As a result, the signal-to-noise ratio decays during the experiment; therefore, it may become necessary to track the signal decay in order to (1) insure the viability of the automated measurements, and (2) compare the calcium signals between stimulus trials. Therefore, for each field-of-view investigated, a large control pulse was applied just before and after a stimulus sweep to record potential changes in the evoked response. Further, base line trends, which include decay, were measured for every cell and every stimulus trial. The decay over short duration is generally linear, and all recorded calcium signals could be scaled accordingly.

These signal boosting and data extraction methods facilitate the translation of hundreds of raw Ca movies into thousands of soma-specific calcium waveforms. Both the generation and manipulation of this data required specialized protocols, which are presented in the following section.

4.1.2.5 Inputs and Outputs: Script generation and data management

The formulaic experimental sequencing of section 4.1.2.3 was developed to enable the use of an all-purpose stimulus script. Therefore, a command interpreter was created to translate user instructions into precisely timed and automated experimental executions. Specifically, the interpreter accepts as inputs an array of user commands that specify the following experimental conditions: (1) stimulus channels/electrodes, (2) stimulus waveform shapes (for each channel), (3) field-of-view coordinates, and (4) triggered averaging count. For each user-specified stimulus trial, the interpreter programs the instrumentation and manages the appropriate sequence of events. Fig 4.5A illustrates how

simple user-commands are translated into automated instrumentation interfacing and sequencing.

The execution of automated stimulus scripts and image segmentation routines generate tens of thousands of calcium waveforms. In order to manage and analyze this information, a database is constructed to catalog data for every field-of-view, stimulated cell, and stimulation sequence. The database includes information about the morphology of each cell, including its geometric properties (such as equivalent diameter and centroid), and pixel-indices as well as the raw and processed calcium waveforms. Additionally, electrode positions and stimulation waveforms are recorded to enable voltage field models and soma-electrode distance calculations. The database structure as well as some example fields are illustrated in Figure 4.5B.

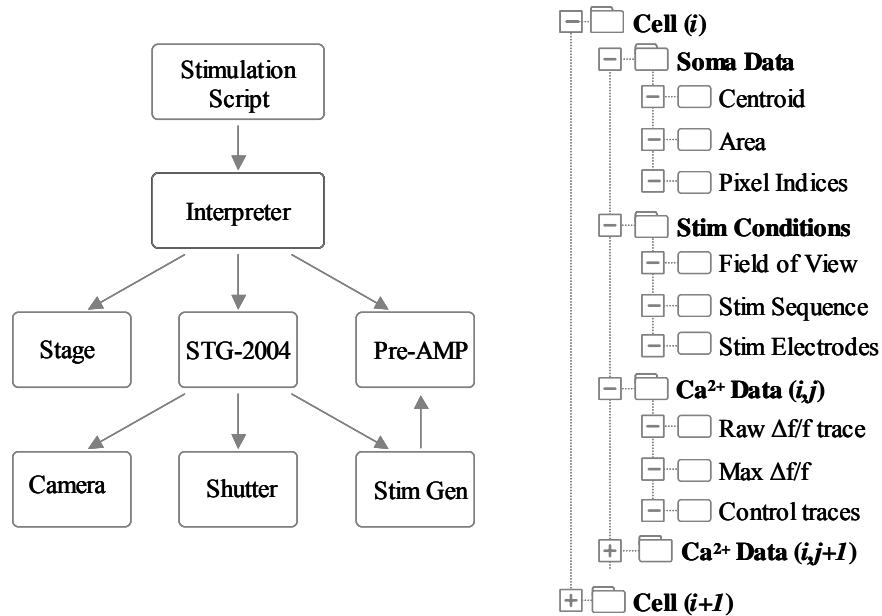


Figure 4.5 Managing the system inputs and outputs. (Left) Illustration of how a simple script is translated into experimental execution. (Right) Illustration of the database structure. Shown is a sample of the data fields for each of the three main data categories (1) Soma image information, (2) Stimulus trial conditions, and (3) Raw calcium data. It is important to note that raw Ca data is recorded in every trial for any segmented cell body, regardless of whether a particular stimulus trial elicited a response. Such data enables direct comparison between stimulus trials.

4.2 Results: Analysis of Evoked Activity

In the previous section, we described an automated stimulus tracking system for the study of region specific neural excitation capable of using both multi-polar field shaping and temporal ion-channel/membrane manipulation. In an effort to build a robust and versatile system, we implemented a platform that could accommodate stimulus waveforms with a broad range of spatiotemporal profiles (multiple electrodes, high resolution arbitrary current waveforms, etc.). Although a vast parameter space creates novel avenues to explore evoked activity, our primary goal was to evaluate evoked responses from the ground up, beginning with very specific inquiries into the excitation patterns elicited by two contrasting waveforms—excitatory and inhibitory. Specifically, in this section, we investigate the threshold responses of hundreds of individual cells to excitatory stimuli; further we investigate the potential to modulate such thresholds with inhibitory waveforms.

4.2.1 System Validation: Tracking Neural Thresholds

Of critical importance to evaluating evoked activity is the ability to not only measure whether or not an excitatory event occurred but also where in space the event occurred and with what probability it could occur again. One of the best measures of such excitation probabilities is the stimulus *threshold*. Unfortunately, traditional techniques to map the stimulus threshold require dozens of serial high-resolution stimulus applications for each individual cell. In this section, we evaluate the potential for our system to extract reliable and meaningful data from hundreds of individual neurons in parallel. Specifically, we demonstrate the following features of this system (1) high throughput

somata. Further, Figure 4.7 demonstrates that the techniques of section 4.1.2.4 can be used to accurately extract calcium signals from individual cells. As a specific example, the calcium waveforms from three of the stimulated cells are displayed for all 25 current pulses (sorted by stimulus charge).

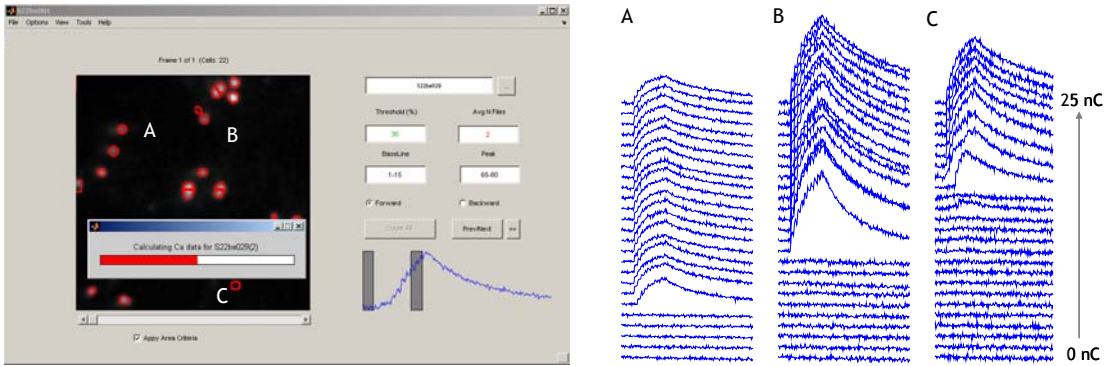


Figure 4.7 Illustration of Ca^{2+} data extraction. Within the graphical user interface, the high contrast image of stimulated somata is depicted with automatically segmented boundaries. Shown, in blue traces, are the calcium signals ($\Delta f/f$ over time) extracted from three of the stimulated cells for all 25 stimulus conditions (sorted by charge). Arrow indicates the direction of increasing stimulus charge (Range: 1 to 25 nC).

Although this experiment applied a two-dimensional sweep of the stimulus parameters (pulse width and amplitude), Figure 4.7 demonstrates that this parameter sweep can be effectively mapped to one dimension—stimulus charge (or pulse-width x current amplitude) (Bostok, 1998). This conclusion may also be logically reached from strength duration curves reported in the literature. It has been shown experimentally, that excitation thresholds follow the chronaxie relationship, which is typically represented by

$$I_T = I_0 + I_0 C/t_T \quad (4.1)$$

where I_T is the threshold current, I_0 is the rheobase (the minimum current required to evoke a response with DC stimulus applications), and C is the chronaxie, which is

classically defined as the duration of the threshold current pulse having an intensity twice that of the rheobase (Nowak 1998). This expression can be re-written to express the threshold in terms of charge:

$$I_T t_T = I_0 t_T + I_0 C \quad (4.2)$$

which clearly indicates that stimulation is a charge phenomenon that is related to a constant and the duration of the stimulus pulse. For short duration stimulation pulses and/or a small rheobase (which is typical for microelectrodes), the $I_0 t_T$ expression can be neglected, and either the stimulus strength or duration may be specified or determined from a constant expression:

$$Q_T = I_T t_T = I_0 C \quad (4.3)$$

In Figure 4.8 the relative change in fluorescent intensity ($\Delta F/F$) is plotted as a function of charge for all 25 stimulus applications for cell (c) in Figure 4.7. For each stimulus waveform, 10 successive applications of the pulse were applied, which accounts for the ten sequential fluorescence steps depicted in many of the intensity traces. Generally, at threshold, a 10-shot stimulus will only evoke 5 action potentials. The inset within figure 4.8 illustrates such a scenario, in which the neuron fired 4 action potentials for a 10-shot stimulus sequence (gray trace). In Figure 4.8, the change in fluorescent intensity between the averaged (15 frames) base-line response and the averaged, *nominal* peak response is plotted as a function of the applied stimulus charge, C_T . The data is fit by a sigmoid curve, demonstrating that the half-maximal of the curve may be a robust measure of the stimulus threshold. These data indicate several important features for cellular behavior and optical tracking: (1) Although stimulus thresholds are often related to current

amplitudes, stimulus charge may be the most important measure of this phenomena (Bostock 1997), (2) Relative changes in intensity ($\Delta f/f$) can be used as a robust measure of excitability, and (3) Based on equation (4.3), charged-based threshold measures may provide a means by which one could calculate the required stimulus amplitude for a given cell and pulse duration.

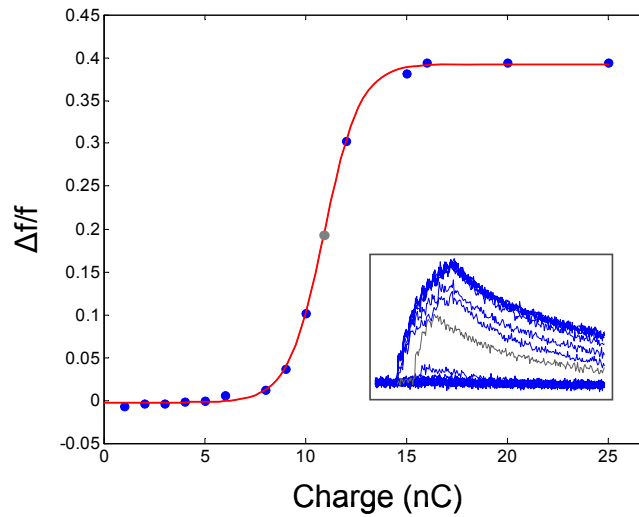


Figure 4.8 Charge-based threshold tracking. The average relative fluorescent intensity at baseline is subtracted from the averaged peak response and plotted as a function of the applied stimulus charge. The red trace depicts a sigmoid curve fit, in which the fit error (sum of squares) was minimized by a Nelder-Mead non-linear regression using the optimization toolbox in Matlab. (Inset) Shown are 25 individual fluorescent intensity traces for cell (c) (Figure 4.7). The gray trace indicates that the neuron only fired four action potentials during the ten shot stimulus. The gray data point on the sigmoid curve fit represents the peak response of this trace. In general, sampling the evoked response in two dimensions (pulse, amplitude) and then mapping to one (charge) may provide a very robust measure for determining the threshold.

In order to assess the reliability of the threshold metric, we used the Nelder-Mead non-linear regression to automatically curve fit normalized threshold curves for each of the 274 cells identified in the experiment. Figure 4.9 illustrates another measure of the stimulus threshold—the slope of the sigmoid, which indicates the degree of confidence that a stimulus above threshold will elicit an action potential. The extracted slopes

spanned approximately two orders of magnitude with an average slope of approximately 3.5 1/nC . For the average cell, the threshold was accurate to $\pm 0.8 \text{ nC}$. At the low and high extremes, the threshold was accurate to $\pm 8 \text{ nC}$ or $\pm 0.1 \text{ nC}$ respectively. Such a wide range in threshold behavior may be related the geometric configuration of the cell.

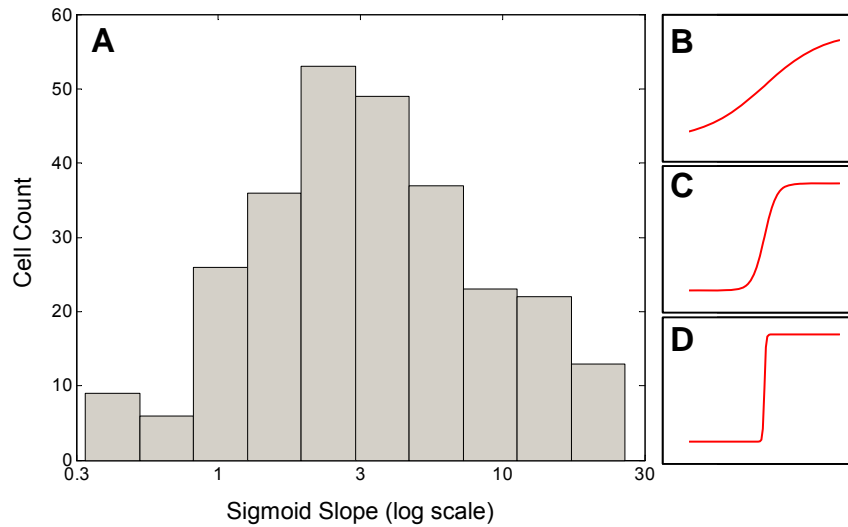


Figure 4.9 Characterization of neural threshold behavior. (A) The slope of the sigmoid describes the probability that a given stimulus will evoke a response (or, alternatively, how well cellular excitation is modeled as a switch). The distribution for the full set of slopes spans approximately two orders of magnitude and is depicted in log scale. The mean slope is approximately 3.5 (1/nC), which indicates that the threshold is an accurate predictor of the cell firing to within $\pm 0.8 \text{ nC}$. At the extremes of the distribution, a slope of 0.3 and 30 would be accurate to within $\pm 8 \text{ nC}$ and $\pm 0.1 \text{ nC}$ respectively. (Inset) Histogram of sigmoid slope on a linear scale. (B-D) traces depict sigmoid curves with slopes of 0.3, 1, and 8. The higher the slope, the more likely the cell is to behave in an off-on, switch-like fashion. The wide range in threshold behavior could potentially be related to the geometry of the cell with respect to the stimulating electrode.

Ultimately, the system is able to measure whether or not a cell fired (0th order), the threshold for which the cell fires (1st order) and the probability that a given stimulus charge will induce cellular excitation (2nd order). These measures were acquired by extracting and processing 6850 calcium waveforms from 274 individual cells identified in 550 calcium movies. It is interesting to note that, from this dataset, the threshold and confidence measures of 274 individual cells across 11 fields of view were acquired from

275 (25 x 11) stimulus shapes, indicating that, on average, approximately one stimulus waveform per cell was required to extract the full probability curve.

4.2.2 Spatial Excitation Patterns

In the previous section, we demonstrated that the system could extract the threshold for extracellular stimulation by charting the relative change in fluorescent intensity as a function of the applied stimulus charge. Further, we fully characterized the degree to which particular cells behave like an on-off switch. We found that, with respect to a single stimulation electrode, individual cells possess tremendous variability in their excitation thresholds and related probabilities. In this section, using the same data set from 4.2.1, we explore the spatial relationship of these cellular parameters. Figure 4.10 depicts the cellular excitation patterns as a function of space. The pixel coordinates from which the data of 4.2.1 was extracted are color-coded according the value of the metric of interest (i.e. threshold, slope, etc.) and projected onto a 2-D picture. Although the projection provides a very accurate measure of how to stimulate individual neurons, it is apparent that, within a 400x400 um field of view, for single-electrode cathodic stimulation, there are virtually no spatial patterns for any of the excitation measures (threshold, slope, etc). Thus more advanced stimulus protocols are required to spatially localize cellular excitation under similar culture and electrode conditions.

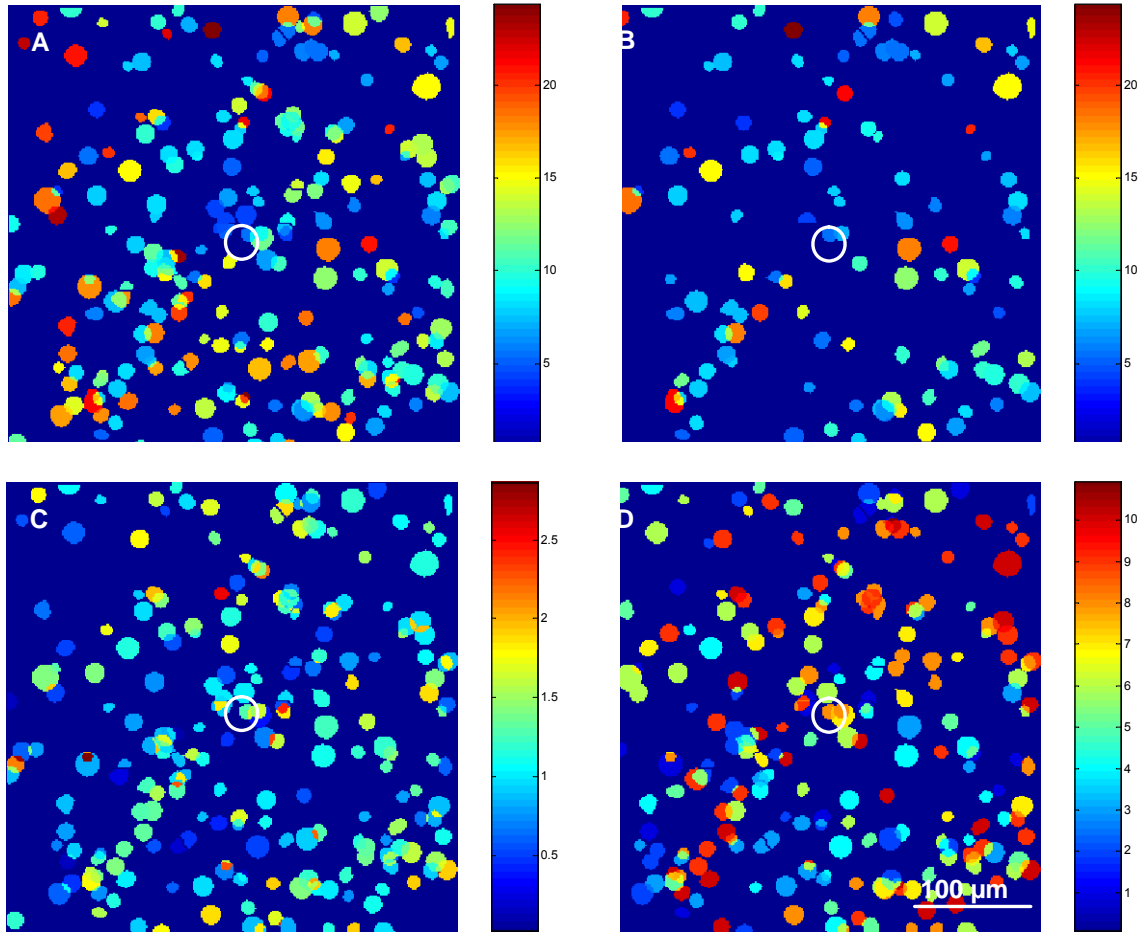


Figure 4.10 Excitation parameters as a function of space. The 30 μm diameter electrode is in the center of the field of view, the results from 11 different electrodes with non-overlapping fields of view are superimposed for one culture. (A) Firing threshold (nC) for each cell. (B) Firing threshold (nC) in which only cells with a 95% probability of firing within $\pm 1\text{ nC}$ of the threshold are depicted. (C) Threshold tolerance (log of slope) or the degree to which a cell behaves like a switch in response to a stimulus charge. ($1/\text{nC}$) (D) Cells are binned according to the electrode that stimulated them, demonstrating that there was very little clustering between trials. The field of view is $400 \times 400 \mu\text{m}$. Scale bar = $100 \mu\text{m}$.

4.2.3 Inhibitory Stimulus waveforms

As demonstrated in the previous section, the region specific excitation of neural tissue and cells is virtually impossible to achieve without invoking an alternative strategy. One such strategy may be excitation's counterpart—inhibition. In fact, one only has to imagine a car without brakes to understand why both excitation and inhibition may be

important for discretionary control over the cellular environment. While extracellular mechanisms for these two modes of observation have been reported, *excitation* overwhelmingly receives the most attention in literature. Therefore, in this section, we briefly, summarize the current work in extracellular *inhibition* before exploring the use of such inhibitory waveforms for exercising control over the evoked response in cortical cultures.

4.2.3.1 Mechanisms for Cellular inhibition

Extracellular neural inhibition is primarily used in motor neuron fiber studies for one of two applications: (1) preventing an action potential from propagating through a nerve (i.e. anodic blocking), and (2) preventing a nerve of certain characteristics (diameter, locale, etc.) from being extracellularly stimulated (i.e. fiber discrimination). The former usually takes advantage of the transmembrane currents induced by strong, DC-like stimuli (10 ms to hours). Such *strong* currents can drive the transmembrane potential to a biologically static regime (e.g. -250 mV hyperpolarization or 100mV overpolarization), where the Na ion channels are effectively locked into a state that prevents firing. In contrast, fiber discrimination applications usually involve relatively fast prepulses (e.g. 0.2 to 1 ms) that manipulate Na ion channels in a manner that does not excite the cell. These *softer* hyperpolarizing pre-pulses (HPPs) or depolarizing prepulses (DPPs) temporarily adjust the state of the Na inactivation channel. Specifically, HPPs and DPPs take advantage of the difference in time constants between activating and inactivating gates. HPPs completely open the inactivation gate with no minimal influence on the activation gate, thus making the cell more ‘excitable’. DPPs, on the other hand, induce a sub-threshold refractory state by closing in the inactivating gate, thus making the cell less ‘excitable’.

Anodic blocking and fiber discrimination techniques, however, demonstrate some drawbacks in actual implementation. Anodic blocking, although very successful in actual experiments, usually involves very long and forceful stimuli. Thus, many stimuli, which make use of this phenomenon, induce a ‘make’ or ‘break’ excitation at the onset or conclusion of the inhibitory pulse. In other words, to prevent AP propagation, the cell is typically driven to an unnatural state that excites the cell. Fiber discrimination, on the other hand, is much gentler and more natural, but requires a degree of precision that may be difficult to achieve with extracellular stimulation. For example, depolarizing prepulses in *patch* models have been shown to be effective in preventing control pulses from causing excitation; however, conditioning prepulse may need to be 90% of the activation-threshold or higher. Thus, it is of interest to evaluate under what conditions inhibitory pulses can effectively be applied to neural tissues and cultures.

4.3.3.2 Characterization of Inhibitory waveforms.

In order to understand the extent to which pre-pulse inhibition can be applied towards selective stimulation, there are two issues of interest: (1) how long does the relative refractory state last, and (2) under what conditions is the pre-pulse effective (i.e. what waveforms reduce membrane excitability, and how difficult is it to apply in practical applications). The former may provide some insight into the mechanisms of inhibition (as the time constant for excitability recovery could be related to a physical cellular mechanism as well as to other published results in the modeling community), and the latter will provide a measure of the efficacy of such pulses. In either case, we examine these relationships by comparing the evoked response of an excitatory control pulse to

evoked responses where the excitatory pulse is preceded by a threshold modulating pre-pulse Figure 4.11.

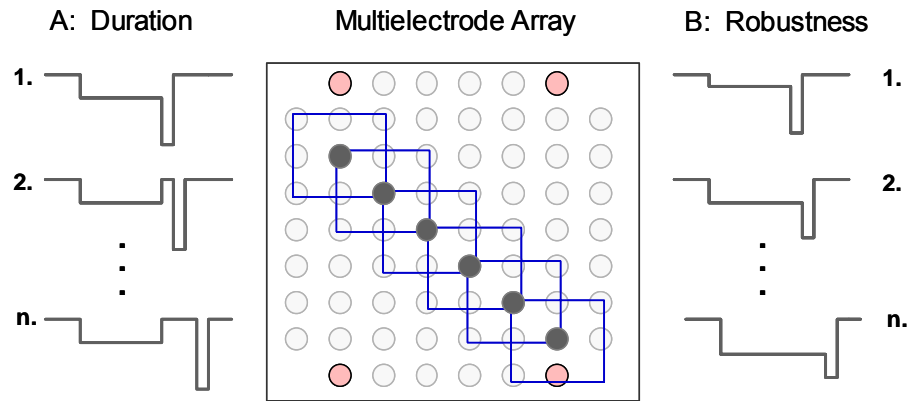


Figure 4.11 Experimental design for the evaluation of monopolar temporal inhibition. Although it is not practical/feasible to temporally sum voltage fields at targeted cells and tissue, the neural membrane and ion-channel time constants introduce a temporal component that can be used to sculpt regions of excitation. (A) Stimulus pulses were swept over one electrode to investigate the duration of the inhibitory effect. Accordingly, the interval between the inhibitory prepulse and excitatory control pulse, Δt , was varied and the Ca response observed. (B) Pre-pulse parameters (i.e. amplitude, duration) were swept over five electrodes to evaluate the pre-pulse efficacy for modulating single cell excitability in dissociated cortical cultures (-2 to $-10\mu\text{A}$ in $-2\mu\text{A}$ intervals and 2ms to 10ms in 2ms intervals; Stimulus control pulse was $-60\mu\text{A}$, $400\mu\text{s}$). For studies (A) and (B), the field of view ($400 \times 400\mu\text{m}$ blue boxes) was centered over the electrode of interest. (In actual implementation, there was no spatial overlap between recordings.)

In order to characterize the duration of the inhibitory effect, we first performed a manual sweep to determine under what stimulus conditions such an experiment would be effective. As demonstrated in figure 4.12A and 4.12B, inhibitory prepulses were effective in preventing an evoked response that would have otherwise occurred. Following manual characterization, a sweep was performed, in which the duration between the prepulse and the stimulus pulse was varied. Figure 4.12 C and D depict the time course of excitability recovery for a single cortical neuron.

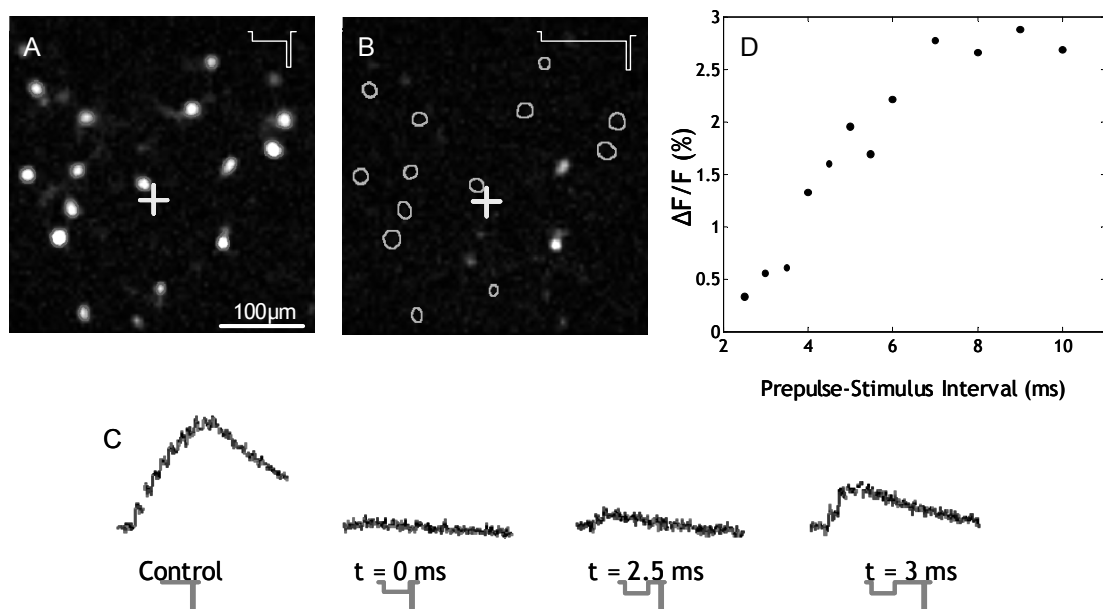


Figure 4.12 Depolarizing pre-pulses transiently inhibit neuronal excitability. (A) Background subtraction image illuminates cell bodies that were stimulated with a 2ms, -5 μ A pre-pulse followed by 0.4ms, -20 μ A stimulus (the crossbars indicate the stimulation site). (B) Extending the pre-pulse duration three-fold to 6ms suppressed stimulation in most of the neurons. The segmentation boundaries indicate somata with suppressed activity. (C) In a separate study, the time interval between the pre-pulse (-5 μ A, 4 ms) and stimulus (-30 μ A, 0.4ms) was adjusted to determine the length of time for which activity was suppressed. Shown are changes in fluorescent intensity ($\Delta F/F$) for one of the suppressed neurons. (D) For the same neuron, Peak $\Delta F/F$ plotted as a function of the time interval between the pre-pulse and stimulus. The cell becomes excitable again around 3ms after the pre-pulse. Normal activity is resumed around 7ms. The gradual recovery of the cell to full excitability results from the probabilities involved that a cell will fire.

Although the results of Figure 4.12 illustrate the feasibility and time course for neural inhibition, it is desirable to understand the conditions under which such an effect can be repeated. In order to more fully characterize inhibitory waveforms, we tracked the excitation responses of neurons to a wide range of inhibitory prepulses. Of particular interest was how effective such prepulses could be in reducing excitability in the immediate vicinity of the electrode (i.e. can inhibitory strategies be used to globally regulate excitation in the neurons surrounding the electrode). As indicated in section 4.3.1, relative changes in fluorescent intensity between stimulus trials can be used as a

robust measure of excitability. By tracking the relative change in peak fluorescent intensity across the full suite of pre-pulses, Figure 4.14 depicts the degree to which the prepulse had an excitatory, inhibitory or negligible effect. Cells represented by bars in the blue shaded region were relatively inhibited, while cells in the red shaded region were relatively excited (x-axis scale is -1 to 1, where -1 indicates 100% *decrease* in excitation and 1 indicates a 100% *increase* in excitation). Cells to the far left of the blue shaded region were completely inhibited (cross bars indicate the mean and standard deviation).

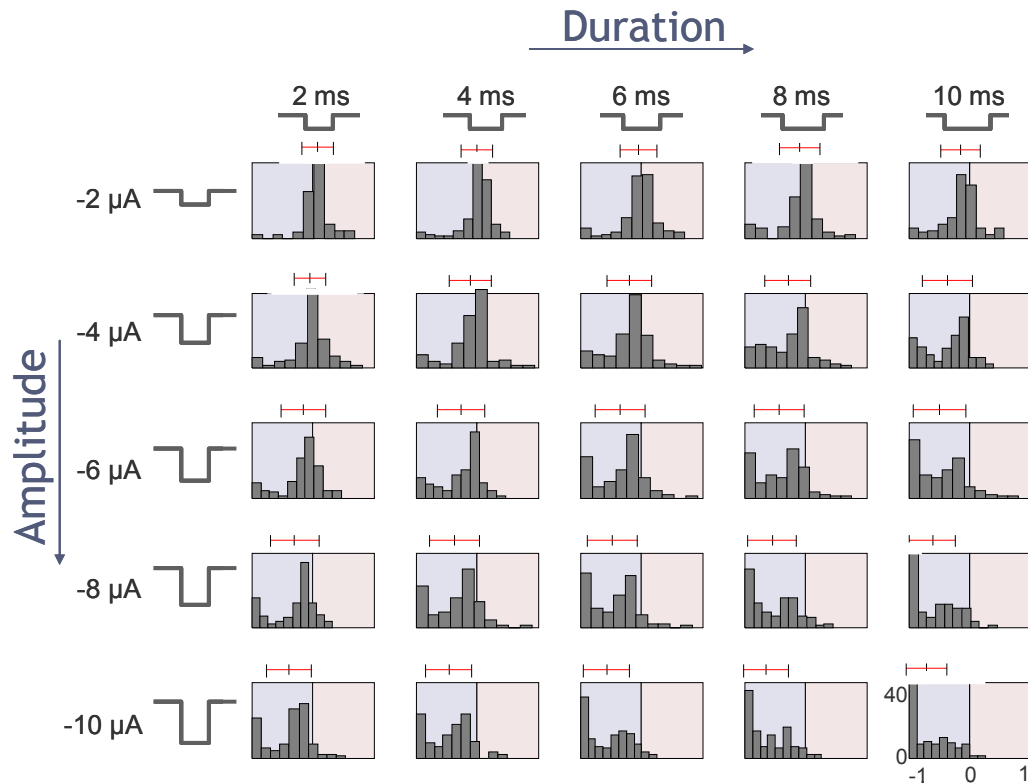


Figure 4.13 Relative changes in neural excitability. Depicted in each graph is a histogram of cell counts (y axis scale: 0 to 40 cells) as function of relative excitability as it relates to the stimulus amplitude and duration (x axis scale: -1 to 1, which indicates a 100% decrease and increase respectively in relative excitability.) Shaded blue region indicates relative inhibition; Red region indicates relative excitation. Cross bars depict the mean and standard deviation. Higher amplitude, longer duration sub-threshold inhibitory pulses induce a near global reduction in relative excitability. The left most bar of each histogram indicates the number of cell for which there was $\leq 5\%$ chance that an action potential would be evoked under the relevant stimulus conditions.

Histograms for which the same stimulus charge was applied (but the amplitude and duration were different) demonstrate very similar patterns, indicating that, like excitation, inhibition is strongly correlated to charge (Data not shown). Shown in Figure 4.14, is the relationship between the percentage of cells that were either relatively inhibited or excited for a given stimulus charge.

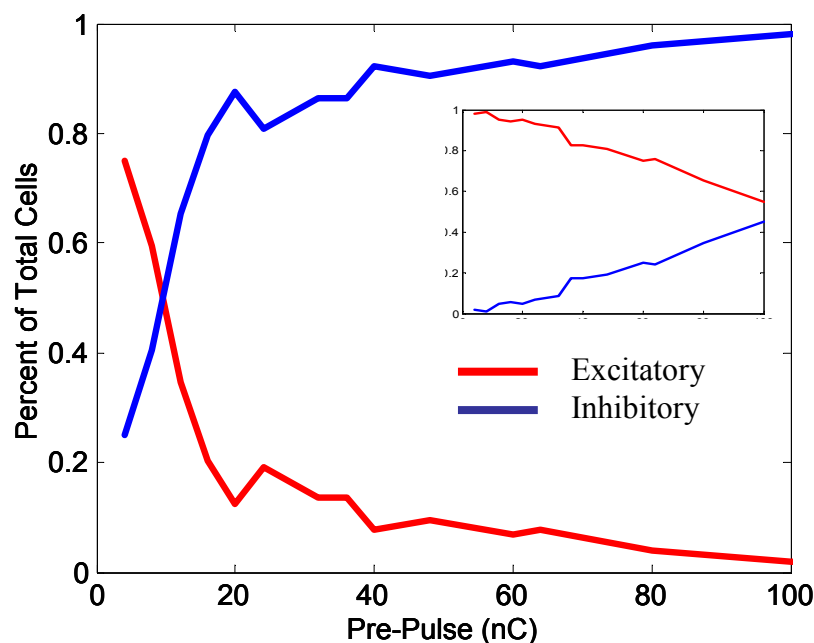


Figure 4.14 Percentage of cells that were either relatively inhibited or excited as a function of stimulus charge. Stimulus pre-pulses on the order of 100nC achieve near global reduction in neuronal excitability within the microscope field of view. Red trace indicates the percentage of cells which experienced a relative increase in excitability. The blue trace, in contrast represents cells that were relatively inhibited. (Inset) Percentage of cells that were either 100% inhibited (blue trace) or at least marginally excitable (red trace.)

As with excitatory pulses, it is important to understand the spatial relationship of inhibition with respect to the stimulating electrode. Figure 4.15 provides an alternative spatial representation of the final pane (bottom right) in Figure 4.13. The relative change

in excitability is depicted in Figure 4.15A. In 4.15B, cells that were completely inhibited are contrasted with cells that were only partially inhibited. In general, there is a global and pronounced trend of inhibition. In the future, the global reduction in excitability could be combined with excitatory waveforms in multipolar configurations to potentially restrict the region of excitation.

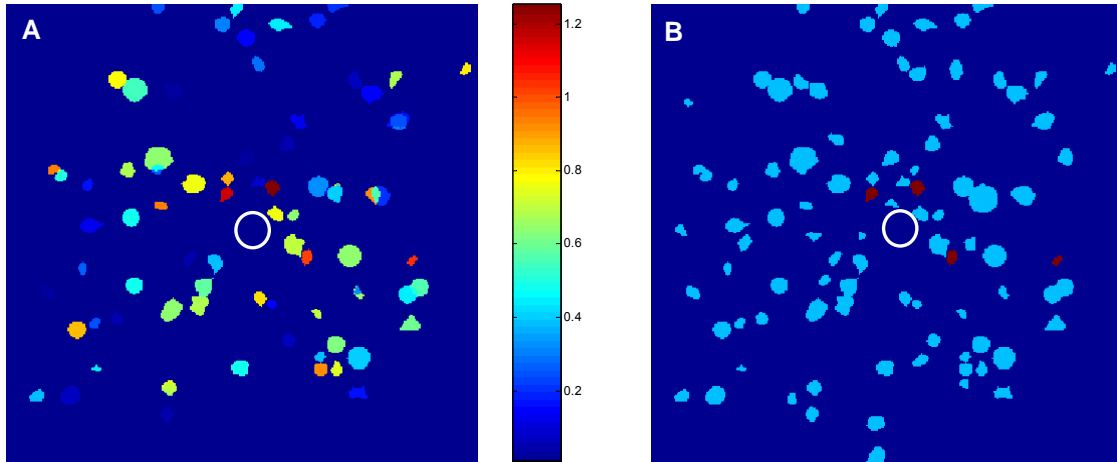


Figure 4.15: Spatial relationship of relative excitability to soma-electrode distances. The 30 μm TiN diameter electrode is in the center of the field of view (white circle), the results from 5 different electrodes with non-overlapping fields of view are superimposed for one culture (A) Relative change in excitability for a 100 nC stimulus pulse (0 indicates 100% inhibition, 1 indicates no change in excitability, and 2 indicates 100% increase in excitability). (B) Cells were color coded blue if they were relatively inhibited and red if they were relatively excited. Picture demonstrates near global inhibition in the vicinity of the electrode. Field of view is 400x400 μm .

4.3 Discussion

We have developed a toolset for high throughput image acquisition and analysis of evoked responses to arbitrary extracellular current waveforms. In addition to developing threshold tracking methodologies, we collected data from thousands of stimulation trials to map out excitation patterns as well as alterations in neuronal excitability (as a function of depolarizing pre-pulse parameters and soma-electrode distances.) These data

demonstrated the performance of the stimulus tracking system and provide a foundation for exploring complex, multipolar stimulus protocols.

One of the challenges in high-throughput optical tracking of functional activity is lack of reliability in signal acquisition. There are many variables that influence the signal quality, including dye loading, photo bleaching, media conditions, and light intensity. In order to accommodate these varying conditions, we devised automated techniques to (1) boost the signal-to-noise ratio and (2) to normalize the fluorescent intensity traces. In particular, a simple ten-shot stimulus proved to be very effective in taking advantage of the slow calcium decay rates to elevate the signal and to provide a robust measure of excitation thresholds. This reduced the required number of triggered averages and consequently increased the throughput with which we could apply and evaluate stimulus pulses (file processing time between movies introduces a fixed delay). Further, the use of synaptic blockers insured that only responses from directly stimulated cells could be observed. Unhindered, the propagation of such stimuli through synaptic networks would have dramatically increased the complexity of the signal processing, particularly in the case of threshold tracking.

Given the brief time window (90-120 minutes) with which we could evaluate functional activity, we used very broad 2-D stimulus sweeps (typically stepping in 10 uA amplitudes and 100us intervals.) We found, however, that by mapping these broad ranged pulse parameters into charge, we could acquire the stimulus threshold with very high fidelity. For some cells, the threshold could be resolved to within ± 0.1 nC. Under certain conditions, in which short pulse durations are used (< 500 us), the charge threshold could be used to specify one stimulus parameter (e.g. amplitude) and to

approximate the other (e.g. pulse duration). The tracking of such charge-induced thresholds also provided a very explicit measure of the probability that a stimulus above or below the threshold would elicit a response.

The relationship of excitation thresholds to soma electrode distances demonstrated a clear lack of correlation, indicating that it is very unlikely to garner spatial control (in the immediate vicinity of the electrode) using a single electrode. However, data from inhibitory waveforms demonstrated that it was possible to approach a global reduction in excitability in the immediate vicinity of the electrode. In the future, as we build towards more complex multi-polar stimulation, it may be possible to take advantage of the transitional inhibitory state induced by the pre-pulses of 4.2.3 to better constrain the response evoked by an excitatory pulse applied at a separate electrode. Specifically, one could draw on biology's own mechanism for heightening sensitivity to certain stimuli—lateral inhibition. Many of the body's sensory input systems (e.g. retina, skin, etc.) enhance signal contrast by inhibiting the activity of neighboring neurons. In a related fashion, one could apply two sets of pre-pulses to create an inhibitory 'moat' around an area of interest. Figure 4.16 illustrates such a strategy. The electrodes on the periphery could be used to apply inhibitory prepulses, while the center electrode could provide an excitatory pre-pulse. Following temporal conditioning, the center electrode could then be used to apply a low-amplitude excitatory and spatially constrained pulse.

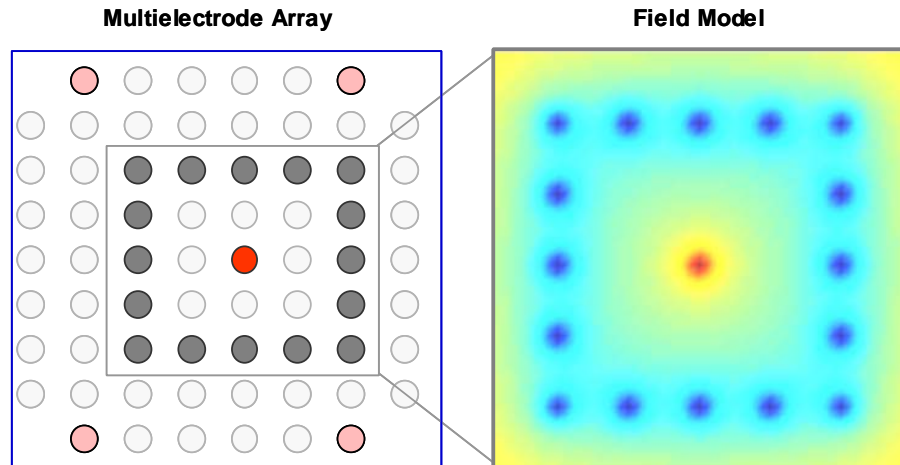


Figure 4.16 Future studies: Multipolar lateral inhibition: (A) A ‘moat’ of inhibition could potentially be created by applying inhibitory prepulses to electrodes surrounding the cells of interest while an excitatory pre-pulse is applied to the center electrode. The application of prepulses could be used to enhance sensitivity to extracellular stimuli in the center while reducing sensitivity in the periphery. This allows for the application a *low-amplitude* excitatory pulse to the target area, which could further improve spatial control of the stimulus. (B) Model of voltage fields during the prepulse conditioning stage as captured 20 μm above the dish.

In this study, the pulse-width duration for effective pre-pulse modulation of excitability (as well as the recovery rate) resided in a regime that is not often reported. Typically, threshold modulating pulses are either $< 1\text{ ms}$ (McIntyre 2000; Grill 1995) or $> 10\text{ ms}$ (Bhadra 2004). In contrast, the most effective pulse-width duration for the stimulation of dissociated cortical cultures resided between 1 and 10 ms. Such a time course and recovery rate may indicate that the mechanism for inhibition may be more related to the passive membrane constant (Bostock 1997) than to the non-linear gating mechanisms of sodium channels (McIntyre 2000; Bhadra 2004). Additional experimentation and a modeling are required to more fully understand the mechanism for inhibition. In the future, well-defined mechanisms would greatly facilitate further exploration and refinement of selective stimulation waveforms.

In these experiments, we did not use the system to track axons, which are among the most sensitive neural elements to extracellular stimulation (Rattay 1999; McIntyre 2000; Nowak 1998). However, the system can account for axonal contributions in a number of ways, either explicitly or implicitly. Explicitly, there are several attractive options: (1) the use of patterned cultured networks to specify the orientation of the axon (2) the use of slices or tissue in which the orientation of axons is known and (3) the use of a higher objective (40x) with a high-density multielectrode array (e.g. MCS ITO array with 10 μ m electrodes and 40 μ m centers). All three options would potentially allow for very high-resolution investigations into the role of the axon in extracellular stimulation (Additional options include intracellular dye injection and viral GFP transfection). The implicit method to account for axons is to assume that in cortical cultures the orientation of axons is random, but that the length is finite. The degree to which this assumption can be quantified, will greatly facilitate estimates of the spatial efficacy of stimulus pulses. (It is interesting to note that the explicit techniques could elucidate methods for algorithmically determining axon orientation in implicit studies). Generally, tissues and cultures that possess more uniform axonal projections may be tremendously easier to selectively stimulate.

The most likely reason that a single electrode cannot elicit a spatially controlled stimulus pattern in dissociated cortical cultures is that the axon projections are seemingly random. Given the finite extent of axons and the statistical improbabilities that axons from all over the dish are traversing every electrode as well as the fact that voltage fields decay inversely with distance, it is likely that there is a spatial pattern for monopolar excitatory stimulation, but that it emerges outside the 400x400 μ m field of view used in

these studies. (A viable option with this system is to build automated collages by systematically shifting the field of view). Nevertheless, the most excitable neural elements (i.e axons, large diameter nerves, etc.) tend to be the most easily inhibited as well. Thus it may be possible to use complex multipolar waveforms to selectively excite somas (or axon hillocks) over so-called axons of passage. In fact, there are published and patent pending monopolar waveforms derived from models that are capable of exerting such control (McIntyre 2000). To the best of our knowledge, however, these waveforms have never been experimentally validated. In the future, such waveforms could be evaluated with the high-throughput stimulus tracking system.

CHAPTER 5

DISCUSSION

In this dissertation we presented a high throughput cellular analysis system for the evaluation of region specific neural excitation and inhibition. The goal of this work was to develop a complete system for (1) precisely controlling critical variables that influence extracellular stimulation and (2) performing high-resolution automated optical tracking of evoked activity. Here we review the design and performance of our system, including each of the novel elements, and discuss the contributions to neural interfacing and medical science. Additionally we evaluate the stimulus strategies presented and discuss future work that could advance selective stimulations technology towards the ultimate goal of seamlessly restoring human nervous-system deficiencies that arise from disease or injury.

5.1 Novel Contributions of this work

In this thesis there were four novel contributions to the field of neural interfacing:

- 1) *Electrode sculpting*: Microfabrication of high-density, high channel-count microelectrodes with automated impedance conditioning
- 2) *Soma segmentation*: The use of 2-D object binning and 3-D context cues for the automated identification of somata in complex, high-density cultures
- 3) *Multicellular analysis*: The development of a high-resolution, high-throughput system for the automated quantification of evoked activity of individual cells in dense populations of neurons.
- 4) *Stimulus waveform characterization*: The spatial and temporal evaluation of single-cell evoked responses to excitatory and inhibitory waveforms.

Our first contribution was the development of automated microfabrication techniques for increasing the electrode count and density as well as specifying the electrical properties of individual electrodes. The electrode is the physical element that is responsible for stimulating, recording, and imaging neural or electroactive tissues. Although many planar MEAs have been developed, few have addressed packaging to insure that the process is scalable to large channel counts and high electrode densities. Furthermore, to the best of our knowledge, this work represents the first attempt to use closed-loop electroplating techniques explicitly specify the impedance magnitude of the electrode. Although the focus of this work was to improve spatial selectivity in neural stimulus applications (i.e. enabling common ground modeling, improving voltage stimulation reliability, and providing more head-room for current stimulation) the matching and specifying of electrode impedance may present a great number of advantages for recording as well: (1) removal of stimulus artifact dependencies on electrode properties (Brown, 2008), (2) reduction of thermal noise introduced by the electrode (Franks 2005), and (3) improved source localization for spike sorting. Finally, pulse plating presented a robust and simple mechanism for improving electrode resilience. Although pulse-plating has found use for bulk electroplating and some large-scale micromolding, it has not been applied to microsensor or microelectrode development. The use of pulse-plating and closed-loop, impedance controlled feedback may present new opportunities for the MEMs and semiconductor industry for automated micromolding and ‘back-side’ wire-trace plating respectively.

Our second major contribution was in the development of novel algorithms for automated 2-D and 3-D soma segmentation in complex, high-density cultures. Unlike

many approaches, which focus either on the identification of dense nuclei or on single-cell complex segmentation, we developed a robust method for high-throughput cell-body identification in dense 3-D cultures possessing rich neurite arborization. Additionally, we created novel algorithms to automatically identify, label, and correct segmentation errors. By incorporating these techniques into a ‘click-and-correct’ graphical interface, we created a platform that could attain near-perfect soma identification in very little time. In the context of stimulus tracking, these algorithms were specially honed to extract spatially-averaged Ca^{2+} waveforms from individual neurons. Although we currently have not implemented high-speed 3-D imaging, these algorithms could be immediately applied towards segmentation in 4-D (three spatial dimensions and time), which would facilitate studies in more complex environments.

Our third major contribution was the development of an experimental system that integrated MEMs, electronics, and optics, with cells, dyes, and drugs. The ensemble of these elements into a flexible and robust system enabled very high-resolution acquisition and analysis of evoked activity. We are among only a few labs that have integrated functional imaging with MEAs, and to the best of our knowledge, the first to develop a high-throughput single-cell stimulus analysis system. Although, the system was exclusively applied to the quantification of evoked activity, the integration of stimulus artifact elimination opens up other possibilities for analysis, namely electrical recording (Please see Appendix A). The pairing of electrical and optical information provides a mechanism to correlate electrophysiological array recordings with a high-resolution ‘standard’ for spatial and functional data.

Our final contribution was the use of the stimulus system to evaluate the spatiotemporal response of neurons to single-electrode excitatory and inhibitory waveforms. While many stimulus mechanisms and waveforms have been simulated, few of these waveforms have been tested in neural cultures, and fewer still have provided detailed, high-resolution measures of the evoked response. Through the evaluation of these waveforms, we determined that although there is very little spatial relationship between cellular threshold and soma-electrode distances, within the confines of a 400x400um field-of-view, it is possible to nearly decrease excitability with inhibitory waveforms. In the future, the ensemble of such excitatory and inhibitory waveforms may enable the region specific excitation of neural tissue.

5.2 System Applications and Future Work

The full scope of this thesis addressed many different elements of selective stimulation. In the course of our work, we encountered many areas in which the system components could be both applied and improved. Additionally, we identified several important future studies that the present system is well equipped to manage. These studies include the investigation of field steering as well as simultaneous optical and electrical recording.

5.2.1 Research Applications

We demonstrated the ability of the system to track the action potentials of individual somas across wide areas and we proposed methods for directly accounting for the contribution of other neural elements, such as axons and dendrites. Such high-resolution insight into the evoked response due to patterned extracellular stimuli may present a

number of opportunities to advance selective stimulation in both basic science and medicine.

In basic science applications, current interfacing technologies limit the ability to explore contributions of individual neurons to network-wide processing. Intracellular interfaces, such as patch clamps and sharp electrodes, provide accurate single-unit stimulation and recording resolution but at the expense of cellular viability and network-wide visibility. Extracellular interfaces, such as multi-electrode arrays (MEAs), are minimally invasive with broad exposure to the network but usually lack the resolution to adequately discern and manipulate individual cells. Selective stimulation through this system has the potential to allow researchers to use extracellular techniques and MEAs to approach intracellular fidelities. Such development will enable the exploration of contributions of individual neurons to network-wide processing; an ability that is critical to the understanding of sensory input processing, memory formation, and behavior (Potter 2001). One such study could involve directly coupling simultaneous stimulation and optical recording with simultaneous electrical recording (Appendix A), to observe stimulus induced plasticity changes and neural network propagation.

In addition to the basic science applications, the Ca^{2+} imaging system could benefit clinical research applications such as retinal implants, neocortex stimulation, and deep brain stimulation. For retina implants, as indicated by (Sekirnjak 2006), one significant challenge is to extracellularly activate neurons at the retinal surface with electrodes that approach cellular dimensions, as little is known about the parameters that would permit reliable retinal stimulation with small electrodes. (Mehenti 2006) were likely the first to use Ca^{2+} to explicitly study the evoked response of patterned, cultured

retinal ganglion cells to single-electrode stimuli. Our system could potentially significantly increase the throughput of similar investigations while enabling much more complex studies, such as the use of coordinated multi-site stimuli or observations across large millimeter scale dimensions. For DBS and epilepsy applications, there has been some notable success in stimulation of the CNS (Kumar 1997). However, efficacy rates for epilepsy control continue to be significantly lower than directly excising out brain tissue. Our system could potentially use epileptic slice models to better understand the scope of the primary evoked responses, towards arresting aberrant activity (Durand 2001). For stimulation of the neocortex, as indicated by (Butovas 2003), multielectrode techniques will be required to reach the spatiotemporal resolution needed to evoke functional activity patterns. Our system could be readily employed to study such multi-site stimulus evoked patterns in either slice or culture preps.

5.2.2 System Improvements

The development of selective stimulation protocols requires unprecedented access to electrical and optical information from the tissue environment. Although this work provides access and control over variables that influence stimulation, improvements in the electrode conditioning, signal conditioning, and image segmentation could significantly improve system *precision* and *throughput* (i.e. number of stimulus applications).

Incorporating real-time image contrast enhancement could provide the most significant improvement to system *throughput*. The present system uses a number of pre-determined steps to insure a high SNR for image processing. For example, *ten* rapid-fire stimuli are currently applied to induce Ca^{2+} accumulation and boost SNR. The use of a

more sensitive dye coupled with real-time contrast evaluation could reduce the number of stimuli significantly. The savings of up to several seconds per stimulus trial could result in hundreds and eventually thousands of additional stimulus trials.

Other improvements that would increase the *precision* of the system include the use of embedded processors during electrode conditioning (chapter 2) and the incorporation of additional context cues for image processing (chapter 3). These improvements are explained in detail in sections 2.4 and 3.4 respectively.

5.2.3 Field Sculpting

The use the fabrication technologies of section (2.1) to develop tightly-packed, micron-sized electrodes, could create an opportunity for advanced stimulus field shaping. In previous research, Spelman demonstrated that closely spaced microelectrodes in 1-D can be used to produce less diffuse, more sharply focused, waveforms that have the potential to improve stimulation efficacy in cochlear implant applications (Spelman 1996). Such approaches could be applied to high density 2-D planar MEAs.

Although a high-density multielectrode array presents tremendous potential for field steering, this potential is coupled with a corresponding increase in complexity. The development of simple models could facilitate the design of intricately contoured extracellular voltage fields and field gradients. Previous research has elucidated how the membrane potential of neural compartments varies as a single stimulation electrode is moved in the extracellular space (McIntyre and Grill, 1999; Rattay 1999). An alternative approach could be to discard the *electrode* orientation models in favor of *field* orientation simulations, thus enabling a more adaptable and flexible approach to deriving stimulus waveforms. One could then solve the ‘inverse problem’ necessary to calculate the pattern

of complex currents required to generate the desired field lines (Rodenhiser 1995). This so called field sculpting could be used to create significantly more accurate stimulus protocols.

5.2.4 Simultaneous Optical and Electrical Recording

Although functional optical recording provides the most accurate measure of the location of stimulated neurons, electrical recording is far better suited for longer term and less invasive studies. Coupling optical and electrical measurements creates and opportunity to develop improved neural localization methods (e.g. spike sorting). Specifically, the optical measurements provide a ‘gold-standard’ or frame of reference with which to develop and evaluate algorithms that can translate electrical neural signals into spatial information. In particular, when stimulation is used with artifact elimination (Appendix A), the opportunity for source localization improves substantially. In fact, it is our hope that, in the future, this system can be supplanted by electrical evaluation techniques that approach the same fidelity. In this manner, the technologies and waveforms derived from this system could find their way into the neural prostheses and therapeutic stimulators of tomorrow.

5.3 Conclusions: Taking a Lesson from the Cells

It is interesting to note that the pre-pulse inhibition phenomenon occurs well beyond the cellular level (e.g. psychological startle reflexes). In fact, the full inhibitory cycle for a neuron is not unlike what a grad-student experiences on vacation. For example, you arrive in a strange and very foreign destination and, as you are in an unnatural environment, you immediately go into a quasi-excitabile state: Where is the

hotel? Is this cab driver trying to rip me off!? Why is that cop tapping his baton and licking his lips!!? After a few days, however, you settle into your environment and you forgot about your job and daily frustrations. When you return from vacation and go back to work, the daily stimuli no longer get your fired up, but, in time, you return to your normal stressed out and ‘excitable’ self. Thus, for cells, psychological reactions, and life itself, it is really just a matter of adaptation and time constants. So, the author of this work is taking a lesson from the cells; after defending this thesis...I’m going on a vacation. And, if you made it this far, maybe you should too! God bless.

APPENDIX A

THE MODELING AND MANAGEMENT OF STIMULATION ARTIFACTS

A fundamental, technical hurdle for electrophysiologists has been to extracellularly record from individual neurons while simultaneously applying micro-stimulation. Unfortunately, stimulation pulses exacerbate neural recording challenges by obscuring action potentials that occur during the time course of the artifact (Gnadt 2003). In recent literature, there are several techniques proposed to remove stimulation artifacts; these, among others, include spectral cancellation (Gnadt 2003), rapid polynomial fitting (Wagenaar 2002), and sample-hold and discharge schemes (Jimbo 2003). Despite the growing number of proposed artifact removal schemes, discussions on the actual cause of stimulation artifacts are notably absent. Ultimately, the best prevention of stimulation artifacts will come from an understanding of their source. In this appendix, a comprehensive model of the stimulus artifact is presented. We then present a closed-loop electrode discharge scheme, which minimizes the stimulation artifact by directly addressing the underlying causes elucidated by the models.

A.1 Non-Linear Electrode Theory

The electro-chemical interactions at the electrode are complicated and elusive; nevertheless, the last 120 years of microelectrode research have produced theories with some meaningful predictive power. David Borkholder summarizes this large body of work in his 1998 thesis submitted to Stanford University (Borkholder 1998). The model in this appendix follows directly from Borkholder's model with a couple of notable

exceptions. To simplify the analysis, Borkholder linearizes the models and assumes that the electrodes never deviate more than 50 mV from equilibrium. The 50 mV range over which his model is valid is actually quite robust, given that neurons seldom produce extracellular potentials at the electrode in excess of 1 mV. In fact, Borkholder is tremendously successful in predicting the frequency dependent impedances for a variety of microelectrode materials and geometries. Stimulation, however, generally occurs in the 0.1 to 5 V range; therefore non-linearities should be incorporated into the model (and then evaluated against linear models). Additionally, non-ideal switching circuitry for stimulation must be modeled to adequately simulate conditions for simultaneous stimulation and recording. In this section, we first provide an overview of the work of Borkholder and Kovacs and then apply their model towards the study of stimulation artifacts.

Immediately after placing a metal in an ionically conducting solution, chemical reactions occur that induce a field at the electrode-electrolyte interface. The electric field, generated by electron transfer reactions, produces the *hydration sheath*, whereby water dipoles orient themselves at the metal surface. Solvated ions aggregate just beyond the hydration sheath, forming what is known as the *outer Helmholtz plane* (OHP). The charges at the metal layer and ions at the OHP form the Helmholtz capacitance, which is given by:

$$C_H = \frac{\epsilon_o \epsilon_r}{d_{OHP}} \quad (\text{A.1})$$

where C_H is the capacitance per unit area, and d_{OHP} is the distance from the OHP to the metal electrode. In addition to the bound ions at the OHP, it has been shown,

experimentally, that capacity at the interface also depends on voltage. Therefore, the Gouy-Chapman capacitance model, which accounts for this dependency by considering the electrical and thermal effects on the time-averaged ionic distribution, can be added in series with the Helmholtz capacitance. The Gouy-Chapman capacitance is given by the following equations:

$$C_{GC} = \frac{\epsilon_r \epsilon_o}{L_D} \cosh\left(\frac{zV_o}{2V_t}\right), \quad L_D = \sqrt{\frac{\epsilon_o \epsilon_r V_t}{2n^o z^2 q}} \quad (A.2)$$

L_D is the Debye length, which characterizes the spatial decay of the potential in the electrolyte, is the characteristic thickness of the Gouy-Chapman capacitance. V_o is the voltage potential at the electrode, z is the valance of the ions, and V_t is kT/q . Both C_{GC} and C_H are serially added to produce the interfacial capacitance, C_I .

If a DC potential is applied across the interface, a current flows. Therefore, it is necessary to model a resistive path in parallel with the capacitor. To produce a net current flow, the potential across the electrode must exceed the equilibrium potential. This potential is termed the overpotential and is characterized by the following four terms:

$$\eta = \eta_t + \eta_d + \eta_r + \eta_c \quad (A.3)$$

where η_t is due to charge transfer, η_d is due to the diffusion of reactants to and from the electrode, η_r is due to chemical reactions, and η_c is due to metal-atom/solution-ion exchange. Borkholder considers the later two insignificant. Charge transfer tends to dominate the overpotential, particularly near the equilibrium point. The current density (A/cm²) generated by the overpotential, η_t , is given by:

$$J = J_o \left(e^{\frac{(1-\beta)z\eta_t}{V_t}} - e^{\frac{-\beta z\eta_t}{V_t}} \right) \quad (A.4)$$

where J_o is the exchange current density (in this case for a Pt Electrode with a hydrogen reaction), and β is the symmetry factor that reflects the energy barrier differences between oxidation and reduction reactions.

Finally, the *spreading resistance* models the spreading of current from the localized electrode to a distant ground electrode in the solution. The spreading resistance is given by (Kovacs 1994) for a rectangular electrode of length, l , and width, w .

$$R_s = \frac{\rho \ln\left(4 \frac{l}{w}\right)}{\pi l} \quad (A.5)$$

where ρ is the resistivity of the electrolyte.

In order to capture the behavior of the electrode under stimulation conditions, the stimulus circuitry must be modeled, which we accomplished by employing a $0.1 \, \Omega$ resistor when a stimulus pulse was applied and $0.1 \, G\Omega$ resistor when the stimulus was off (i.e. a non-ideal switch). The ensemble of all the modeling elements, including the stimulation circuitry is depicted in Fig. A.1

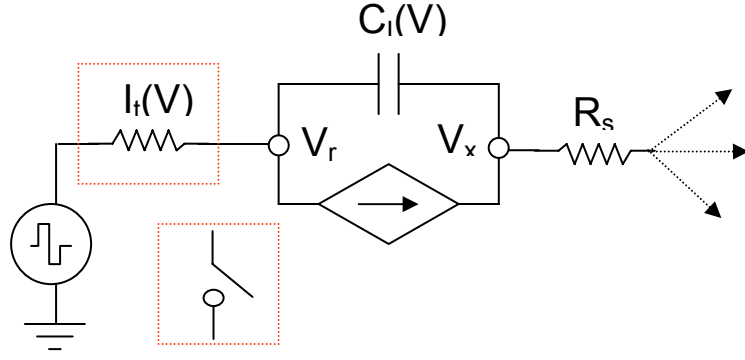


Figure A.1: Circuit diagram for the non-linear electrode model and stimulation circuitry.

A.2. Modeling Stimulation Artifacts

Using Figure A.1, Equations for the voltage at the recording site, V_r , and voltage at the electrode, V_x , were derived using nodal analysis and manipulated to remove any derivatives and algebraic loops. The final expressions for V_r and V_x are as follows:

$$V_x = \frac{R_s(V_{in} - V_r)}{R(t)}, \quad (A.6)$$

$$V_r = \left(1 + \frac{R_s}{R(t)}\right)^{-1} \left(\frac{1}{R(t)C_i} \left(\int (V_{in} - V_p) dt - \int I(V_r - V_x) dt \right) + \frac{R_s V_{in}}{R(t)} \right) \quad (A.7)$$

The solution to the above equations were solved using Simulink's ODE45 (Dormand-Prince) solver with auto-scaled time intervals and error tolerances (Figure A.2).

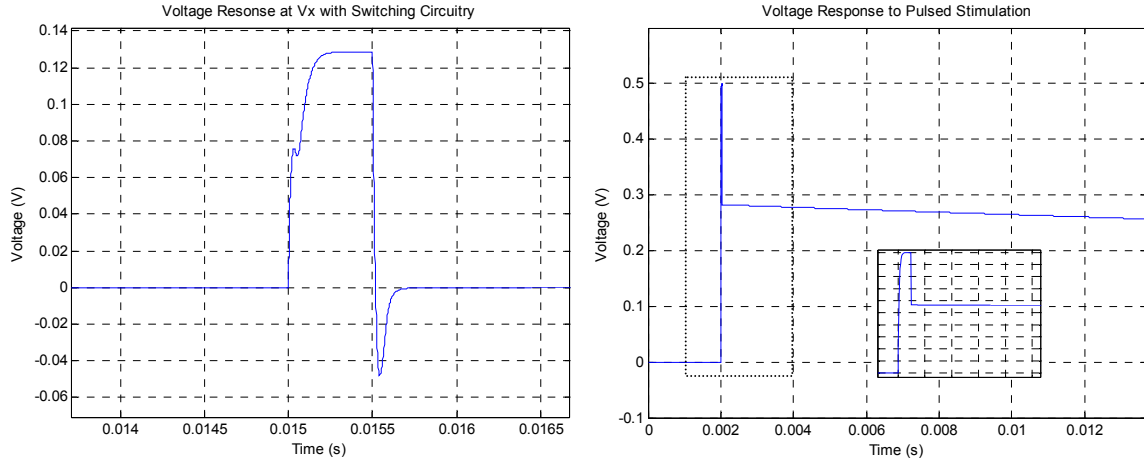


Figure A.3 Voltage Trace measured at V_r both without (A) and with (B) switching circuitry present response. (Inset: zoomed in view stimulus artifact)

The voltage response in Figure A.3 appears very similar in nature to actual stimulation artifacts reported by (Brown 2008, Blum 2007, Jimbo 2003), which clearly implies that the switching circuitry is significant in producing the artifact. Further, in figure A.4, a “biphasic” pulse is applied, producing yet another typical artifact.

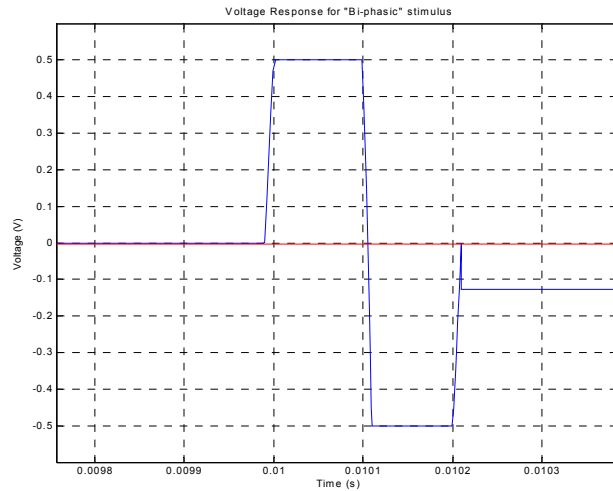


Figure A.4 Voltage Trace measured at V_r demonstrating that charge is trapped on the electrode.

The length of time for which the trapped charge remains in Figures A.3 and A.4 (discharge rate) can be reduced by decreasing the closed switch resistance value, which indicates that the time constant given by the switching circuitry resistance and the electrode capacitance determine the discharge rate. This relatively simple behavior is faithfully represented with linear models (Blum 2005). Thus, despite non-linear voltage dependencies of the electrode circuit elements, namely interfacial capacitance and charge transfer resistance, simple linear models sufficiently capture the majority of the stimulation artifact behavior. This characteristic likely results from the fact that the electrode immediately returns to its linear regime following an applied stimulus ($< 50\text{mV}$).

A.3 Managing Stimulation Artifacts

Our initial work on simultaneous stimulation and recording began with an inquiry into the source of the stimulation artifact. Our intention was to develop a more comprehensive solution to the stimulation problem through a better understanding of the underlying causes. A comparison of complicated, non-linear stimulus-electrode models with simple, linear models indicated that the major source of artifacts is trapped charge that accumulates on the electrode (Blum 2004). Using a linear electrode model, we observed that complete artifact elimination would require at least eleven time constants, of the model components, to remove the artifact. For a $40\text{ }\mu\text{m} \times 40\text{ }\mu\text{m}$ platinum black extracellular electrode in an open circuit this could take at least 50 ms and would depend on the applied stimulus waveform. Our model also demonstrated that multiple or unbalanced stimuli could extend the artifact duration well into the tens of seconds.

Despite our efforts, none of the electrode models (linear or non-linear) could capture all of the long-lasting artifact dependencies, stochastic, and non-linear processes that resulted from redox reactions at the electrode-electrolyte interface (Brown 2008). Furthermore, while the primary cause of stimulation artifacts was the charge stored in the electrode, both the models and our empirical observations confirmed that effects from the intervening circuitry could easily aggravate the artifact. Thus a solution was required that could account for linear and non-linear electrode effects as well as circuit effects.

To address the compounding and highly sensitive artifact problems, we designed an integrated circuit (IC) to integrate each electrode into a feedback loop (US Patent No. 07/0178579). This strategy actively discharges the electrode in a manner that can control both linear charge accumulation as well as transient and non-linear electrode effects. Additionally, simultaneous stimulation and recording could be achieved by preventing circuit-artifacts at multiple sources, which involved the following strategies or phases: (1) amplifier blanking, (2) filter response management, and (3) soft switching. Specifically, amplifier blanking was used to reduce cross-talk induced by high-amplitude and high-speed stimulus pulses, filter management was used to improve the recovery speed of the recording amplifiers, and soft switching was used to avoid abrupt voltage transitions at the amplifier inputs. Figure A.5 depicts our current IC.

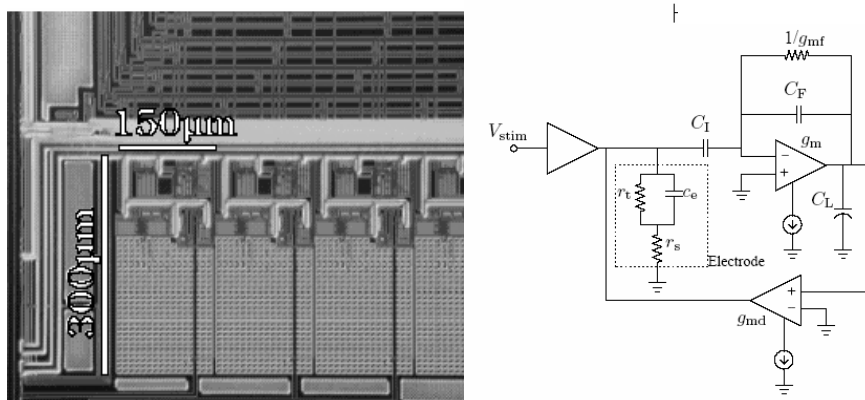


Figure A.5: Artifact elimination technology (A) micrograph of custom IC for simultaneous stimulation and recording. White box highlights the electrode control circuitry for a single electrode, for which a high level schematic is depicted. (B) The stimulating, recording, and artifact elimination circuitry integrate the electrode into a feedback loop, which is capable of removing accumulated charge at the electrode-electrolyte interface. The dashed-box depicts the circuit elements that represent the electrode model.

To accommodate the hardware and software support required by our custom IC, we built a system that enabled both high-level experimental design, such as stimulus waveform shaping and electrode selection, and low-level control and characterization of the stimulating electrode. This development allowed us to fully characterize the performance of our system, and it granted us greater access to the electrode-electrolyte interface. Overall, our current 16-channel system, under optimal conditions, has reduced the artifact to 3 ms or less on the *stimulating* electrode and 500 μ s or less on *neighboring* electrodes, and evoked cellular responses have been consistently observed on the stimulating electrode.

In the figures below (Figures A.6- A.13), we illustrate the performance of various artifact management techniques. In actual practice, each of the individual strategies works in concert to minimize the stimulation artifact (Figure A.6 illustrates the method to

calculate the artifact duration). Specifically, we incorporated the following artifact management strategies into a single simultaneous stimulation and recording platform: (1) Electrode Discharge (Figure A.7), (2) Pole Shifting (Figure A.8), and (3) Soft Switching Figure (A.9). Electrode Discharge removes charge that remains at the end of a stimulus (as indicated by the modeling results in A.2). However, because the frequency characteristics of the amplifier itself contribute to the artifact, modifying the frequency response of the main amplifier, or pole shifting, for a short period following electrode discharge also enables further reduction the artifact. Finally, because abrupt transients affect the filter and the electrode itself, smooth transitions between artifact management phases creates additional opportunities for artifact reduction. Figure A.10 illustrates the software that was used to specify the stimulus and artifact elimination parameters. Figures A.11 and A.12 illustrate the performance of the system when stimulating dissociated cortical cultures. More details can be found in (Brown 2008). (Mr. Nakul Reddy contributed to the acquisition of the artifact elimination data.)

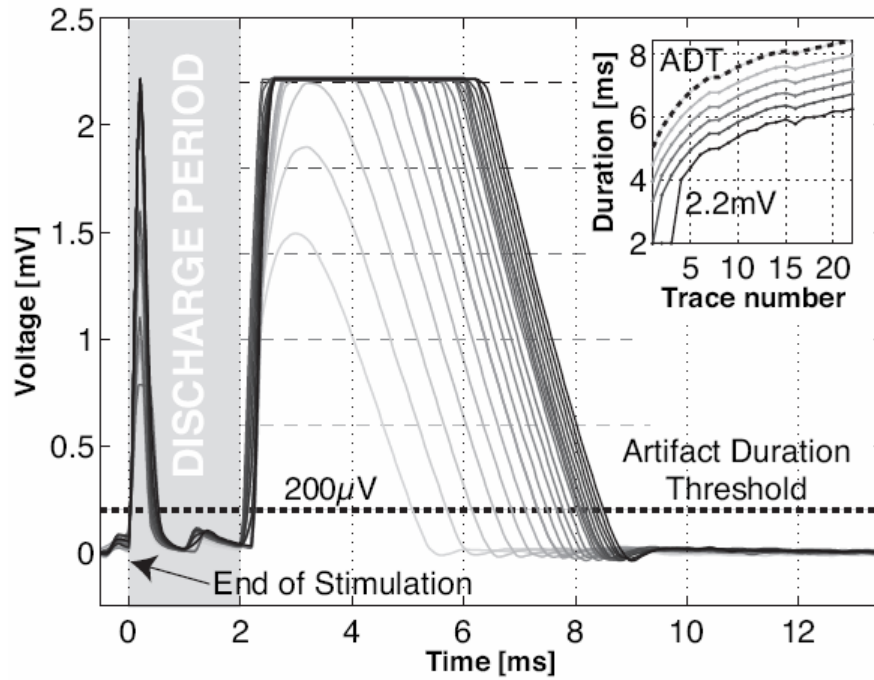


Figure A.6 Definition of Artifact Duration. Example of the output of the recording system after a ± 500 mV, 200 μ s per phase stimulation and a 2 ms discharge (not enough to eliminate the artifact). This 25 trace recording is a transient behavior at the initiation of 8 Hz periodic stimulation (darker traces happened later in time). The artifact variability can be seen to converge towards a narrow range of values. The initial spike (as the main amplifier is turned on), and the relatively flat region that follows, is due to the activity of the discharge loop. In this case the recording system saturates at approximately 2.25 mV. The inset shows the artifact duration depending on the chosen threshold (the shading corresponds to the thresholds indicated by dashed lines in the main figure).

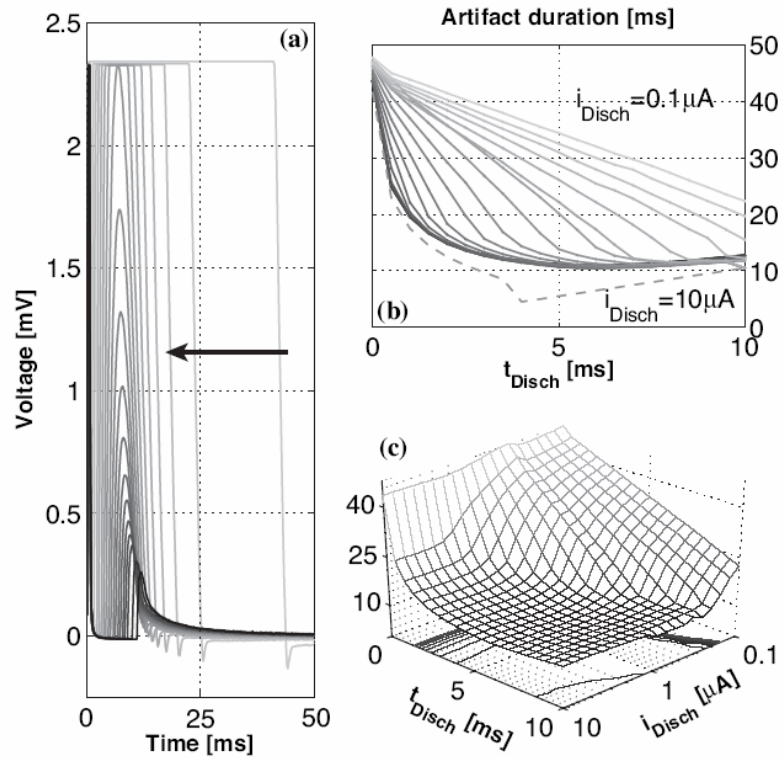


Figure A.7 Artifact duration after an initial discharge period of 500 μs at 10 μA : (a) Set of time traces of artifact data with a discharge current of 10 μA parameterized by discharge time, the arrow indicates the direction of increasing discharge time. (b) Artifact duration with respect to discharge time parameterized by discharge current (logarithmically spaced, 20 current traces from 10 μA to 0.1 μA). The dashed line corresponds to a higher artifact threshold of 2 mV (the sloped region is the total discharge time as the artifact does not exceed the threshold). (c) 3-D representation of the data set from (b). Note that the artifact duration slightly worsens for larger discharge currents and times.

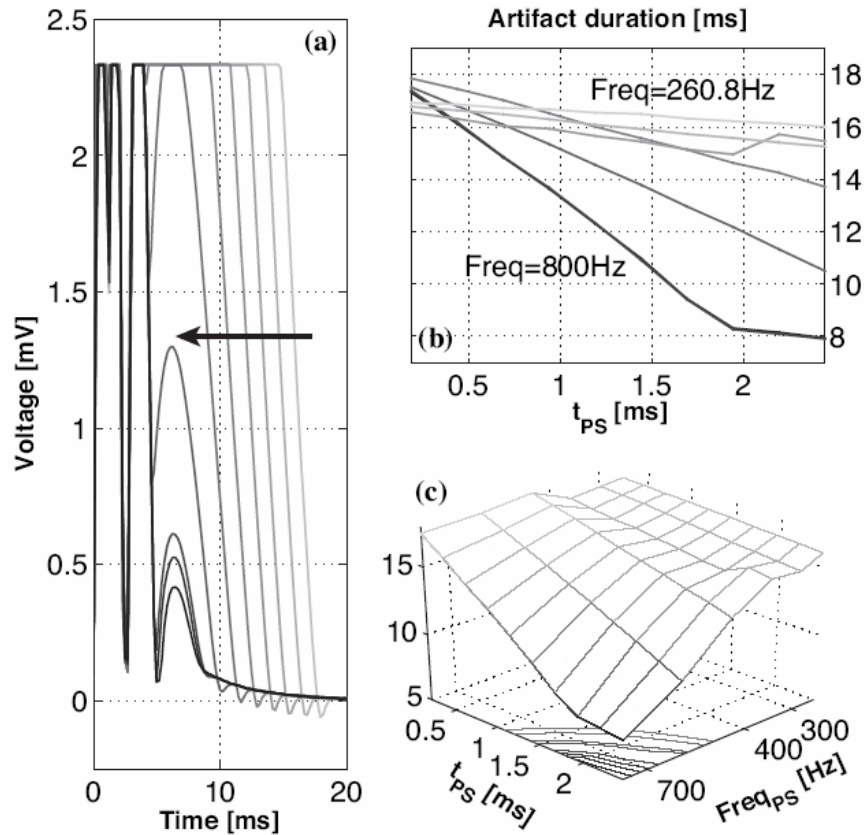


Figure A.8 Artifact duration with respect to pole shift time and frequency after a discharge period of 1 ms at 5 μ A, followed by 1.5 ms at 1 μ A. The pole shift effect is additive to the recording high-pass frequency of 200 Hz (the frequencies shown are actual high-pass values): (a) Set of time traces of artifact data with a pole shift frequency of 800 Hz parameterized by pole shift time, the arrow indicates the direction of increasing pole shift time. (b) Artifact duration with respect to pole shift time, parameterized by pole shift frequency. (c) 3-D representation of the data set from (b).

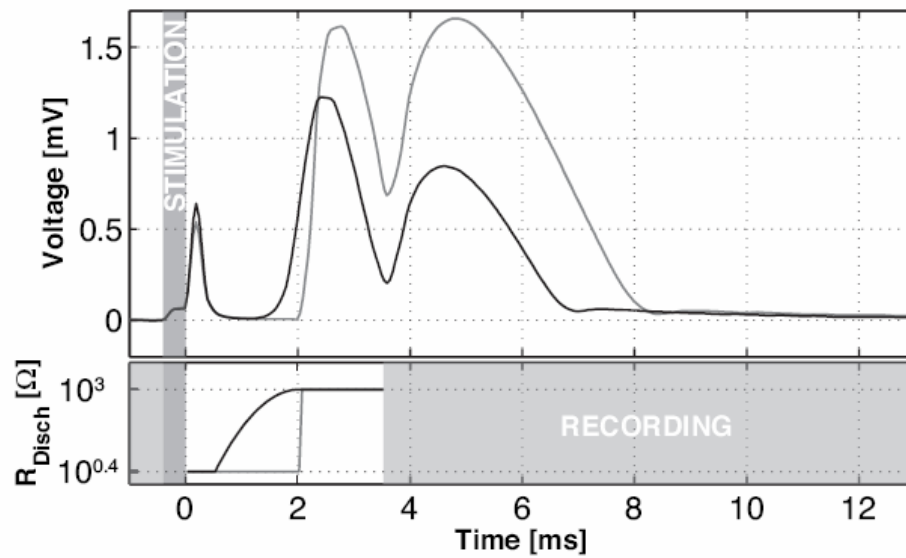


Figure A.9 Soft transients improve recording performance. Example of two artifacts with (black) and without (gray) a soft transition between the high and low discharge currents. The bottom plot shows R_{Disch} for each curve; both start and stop at the same values and have a total discharge time of 3.5 ms. The initial peak saturates the amplifiers though the higher currents make it too fast to be captured at this sampling rate. The gray regions denote the areas in which the corresponding amplifiers are turned off. Note that the larger overall current (smaller overall R_{Disch} value) performs worse than having a smooth transition.

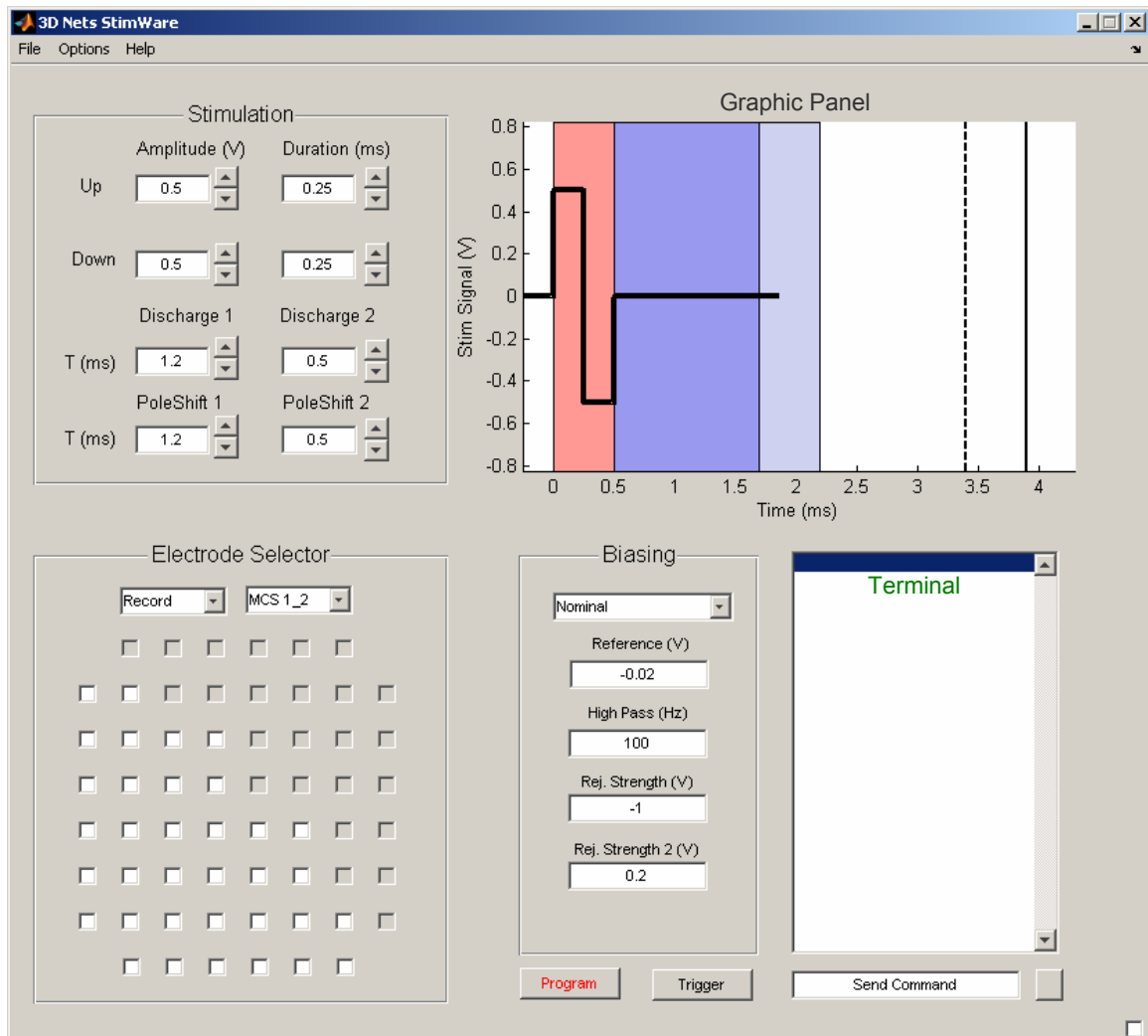


Figure A.10 Graphical user interface for designing stimulus waveforms and managing the artifact elimination parameters. The interface, which translates user specified parameters into PIC microcontroller commands, is divided into five sections, which clockwise from the bottom left are (1) Electrode Selector: Allows the user to turn individual recording channels on or off as well as designate which channel(s) are used for stimulation. (2) Stimulation: A panel for specifying the stimulation and discharge parameters, which are graphically represented in (3) Graphic Panel: The red phase designates the stimulus profile, the dark and light blue phase represent the duration of the 1st and 2nd discharge phase respectively. The vertical dashed and solid line indicate the 1st and 2nd PoleShift phase respectively. (4) Terminal: The terminal displays microcontroller commands that are echoed back from the microcontroller. Finally, (5) Biasing Panel: a multilevel text entry panel for setting the chips biases. Inputs, such as high pass cut off frequency, are mapped through calibration curves into ADC voltage codes.

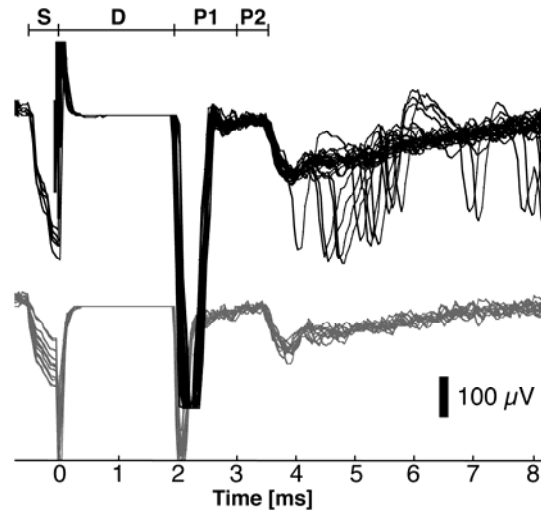


Figure A.11 Recording evoked neural responses. Recordings through our system with a discharge time of 2 ms @ 50 μ A, two pole-shift phases of 0.5 ms @ 2200 Hz and 0.5 ms @ 700 Hz. High-pass filter setting: 200 Hz. Stimuli were positive-first biphasic pulses (pulse width 200 μ s for each phase) with an amplitude of 0.1V (bottom trace) or 0.5V (top trace). Note the recorded responses starting 4 ms after stimulation. Data collected by Johnny Nam at the university of Illinois Urbana Champaign

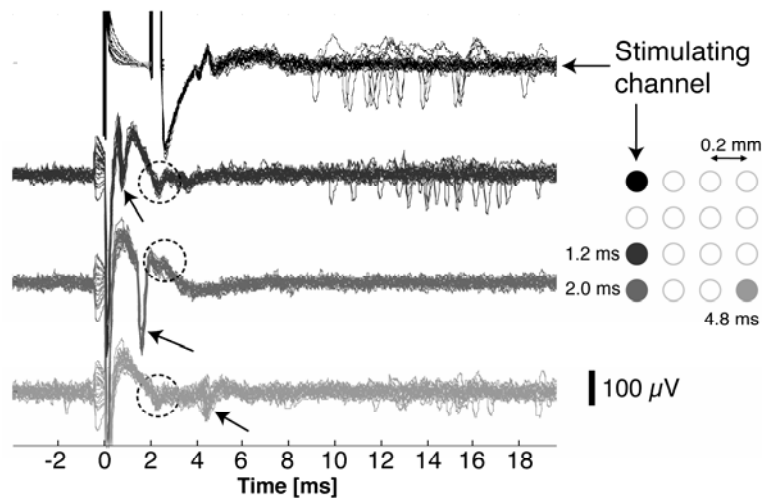


Figure A.12 Performance of Artifact elimination technology. Recordings through our system with a discharge time of 2 ms @ 50 μ A, two pole-shift phases of 2 ms @ 2000 Hz and 0.5 ms @ 500 Hz. High-pass filter setting: 10 Hz. Acquired data were filtered by a digital 2nd order Butterworth high-pass filter with a cutoff frequency of 200 Hz. The stimuli were positive-first biphasic pulses with 200 μ s per phase, at \pm 0.5V. The circles denote additional crosstalk artifacts in the IC, the arrows show time-locked action potentials. Data collected by Johnny Nam at the University of Illinois Urbana-Champaign.

APPENDIX B

ELECTROPLATING HARDWARE, SOFTWARE, AND RECEPIES

This Appendix describes the hardware, software, and chemical solutions used for the closed-loop electroplating techniques described in chapter 2.

B.1 Electrical Schematic for Electroplating Circuitry

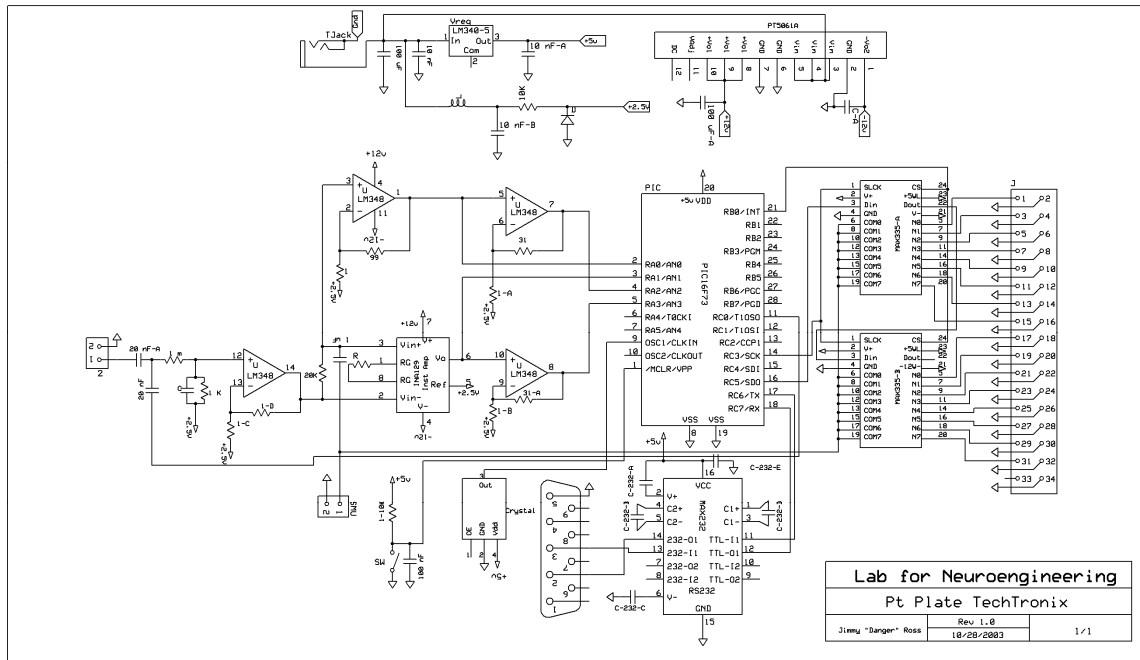


Figure B.1: Electrical Schematic for closed loop electroplating circuitry. The electroplating current is switched onto individual electrodes through two daisy chained, SPI-controlled, Maxim analog switches. A low amplitude (<10 mV) AC 1 khz signal is capacitively coupled onto the electrode and a reference resistor. Waveforms across these elements are amplified (INA129P) and sampled using the PIC 16F73, 8-bit analog to digital converters and transmitted serially (through RS-232) to Matlab for processing.

B.2 Software for Closed-loop Pulse Plating

The current source used provide the plating current was a Keithly 2400. The following code used internal timing configurations and triggering to control the current pulses:

```
function ism2400 = ism2400pulseinit(port,upPhase,downPhase)
```

```

%-----%
%The front-end interface to the Keithly 2400 is not
%configured to apply pulsed currents. The following
%code uses the internal timing configurations to apply
%controlled electroplating pulses.
%
% port: RS-232 comport used for interfacing
% Uphase: Amplitude value for pulse
% DownPhase: 2nd phase amplitude value for pulse
%-----%

global ISM2400_SWEEP_SIZE SWEEP_BIT ISM2400_VCOMPLIANCE

ISM2400_SWEEP_SIZE = 2;
SWEEP_BIT=uint16(2^3);
ISM2400_VCOMPLIANCE = 5;

ism2400 = serial(port);
ism2400.BaudRate = 57600;
fopen(ism2400);
fprintf(ism2400,':*RST');
fprintf(ism2400,':*SRE 1');
fprintf(ism2400,':SYST:AZER:STAT OFF');
fprintf(ism2400,':SOUR:FUNC CURR');
fprintf(ism2400,':SENS:FUNC:CONC OFF');
fprintf(ism2400,':SENS:FUNC "VOLT"');
fprintf(ism2400,':SENS:VOLT:NPLC 0.08'); %page 1870
fprintf(ism2400,':SENS:VOLT:RANG 20');
str_command = [' :SENS:VOLT:PROT:LEV ' num2str(ISM2400_VCOMPLIANCE)];
fprintf(ism2400,str_command);
fprintf(ism2400,':FORM:ELEM VOLT');
fprintf(ism2400,':SOUR:CURR:MODE LIST');
fprintf(ism2400,[' :SOUR:LIST:CURR' num2str(upPhase), ','...'
num2str(downPhase)]);
fprintf(ism2400,':OUTP ON');

function TrigPulse(ism2400);
%-----%
%Function to initiate pulsed-currents and to poll for
%completion
%
% ism2400: serial port object
%-----%
global SWEEP_BIT

TIME_OUT = 5;
fprintf(ism2400,':INIT');
fprintf(ism2400,':stat:oper:cond?');

tic
while (ism2400.BytesAvailable == 0) & (toc < TIME_OUT)
    pause(0.05);
end;
if toc > TIME_OUT

```

```

        disp('Warning: BytesAvailable poll exceeded the maximum allowable
time limit');
end;

bits = uint16(fscanf(ism2400,'%d',ism2400.BytesAvailable));

%Wait until the triggered sweep is done executing
while bitand(bits,SWEEP_BIT)
    fprintf(ism2400,':stat:oper:cond?');tic
    while (ism2400.BytesAvailable == 0) & (toc < TIME_OUT )
        pause(0.05);
    end;
    bits = fscanf(ism2400,'%d',ism2400.BytesAvailable);
end;

function medianVpp = GetData(s,Channel,num)
%-----%
%Function for initiating voltage sampling %
% %
%s: the serial object for communicating with the PIC %
%Channel: The A/D channel to sample %
%num: The number of times to take the sample %
%-----%

for loop = 1:num
    a= [];
    ymid = [];
    f = 0;
    while f == 0
        str_command = ['/a ' num2str(Channel)];
        a=picwrite(s,str_command,'timeout',.40);
        f = size(a) > 160;
    end;
    aa=sscanf(a(5:end),'%2x');
    bb = aa*5/256;
    y=(resample(bb,20,1));
    ymid = y(200:800);
    yMax(loop) = max(ymid);
    yMin(loop) = min(ymid);
end;
yMax - yMin
medianVpp = median(yMax) - median(yMin);

```

B.3 Platinum Black Electroplated Recipe

In a solution of DI water, mix up the following:

- 1) 1% chloroplatinic acid (diluted from 8% hydrogen hexachloroplatinate)
- 2) 0.0025% HCl
- 3) 0.01% lead acetate

APPENDIX C

BIOLOGICAL PROTOCOLS

C.1 Protocol for Preparing Dissociated Cortical Cultures.

This cell culture protocol is primarily derived from (Potter 2001) and incorporates some dissociation techniques developed by Dr. Michelle LaPlaca's research group. Surface coatings such as PEI/Laminin may be used to improved cell adhesion.

1. In a 15 ml centrifuge tube, digest embryonic-day-18 rat whole cortex pieces in 2 ml papain solution for 8 min at 37 °C.
2. To halt digestion, immediately remove the papain and add 1 ml of plating medium (with serum)
3. To facilitate dissociation and digest sticky DNA residue, add 200 µl of DNase (1.5 mg/ml).
4. To dissociate the cells, vortex the solution in 5 second intervals until solution becomes cloudy (do not exceed more than 35 seconds of cumulative vortexing)
5. To remove debris and large volumes of tissue, gently pipet out the suspended cell solution into a 40 µm cell strainer placed within a 35mm petri-dish.
6. Transfer the filtered suspension to a 15 ml centrifuge tube. Increase plating medium volume to 3- 4 ml. Add 0.5 ml of 5% BSA solution in phosphate-buffered saline to the bottom of the solution.
7. Centrifuge the cell suspension at 200 x g for 6 minutes at room temperature
8. Remove and save the supernatant. Add 0.5 ml of the plating medium to the pellet.
9. Triturate the pellet very gently to re-suspend the cells. Count the cells with a hemocytometer.
10. Plate the cells into MEAs (approximately 4×10^5 cells/ cm²)
11. Store in an incubator at 35 °C with 5% CO₂ and 9% O₂

C.2 Preparing Aliquots of Fluo-5F Ca²⁺ Dye

When preparing the dye, care should be taken to minimize light exposure (e.g. wrap foil around the 15 ml centrifuge tube used for preparing the mixture). This recipe is primarily derived from (Ikegaya 2005).

1. Begin with one 50 µg vial of Fluo-5F powder (Invitrogen)
2. Add 45 µL of anhydrous DMSO into the Fluo-5F vial
Note: Mix gently but thoroughly with the micro-pipetter in order to dissolve all of the powder
3. Add the DMSO-Dye solution to 1 ml of artificial cerebral spinal fluid (ACSF) (use the foil-wrapped 15 mL centrifuge tube).
4. Add 1 µl of pluronic F-127 and vortex the whole solution.

5. Partition into 10 aliquots of 100 μ l units. Store in -80°F freezer.

C.3 Protocol for Bulk Loading Ca^{2+} dye into Dense Cortical Cultures

When loading the dye, care should be taken to minimize light exposure (e.g. wrap foil around the top and bottom (independently) of a petri-dish and use to transport vials and dishes).

1. Remove all of the media from the culture dish
2. Add back in 400 μ l of ACSF to the culture dish
3. Add 100 μ l of Fluo-5F dye to the center of the dish (from C.2)
4. Store dish in 34°F incubator for 35 minutes.
5. Remove the dye-rich media from the culture dish and apply 1 ml of your preferred media.

C.4 Protocol for Inhibiting Synaptic Transmission (following dye loading)

The concentration of blockers sufficient to block virtually all spontaneous activity was derived by Dr. Douglas Bakkum.

1. Following 35 minutes of bulk load of Ca^{2+} dyes (C.3), mix up 50 μM BMI, 100 μM APV, and 10 μM CNQX) in 1 ml of ACSF in a 15 ml centrifuge tube
2. Vortex the ACSF and synaptic blockers
3. Withdraw all of the dye-rich media from the culture dish
4. Add in the ACSF with synaptic blockers.
5. After concluding experiments performed with loaded dyes and added blockers, sequentially rinse the dish 3 times with 1 ml of ACSF.
6. Finally, add back in 1 ml of your preferred culturing media.

REFERENCES

- Adiga PSU, Chaudhuri BB (2000) Region based techniques for segmentation of volumetric histo-pathological images. *Computer Methods and Programs in Biomedicine* 61:23-47.
- Adiga PSU, Chaudhuri BB (2001) An efficient method based on watershed and rule-based merging for segmentation of 3-D histo-pathological images. *Pattern Recognition* 34:1449-1458.
- Al-Kofahi KA, Lasek S, Szarowski DH, Pace CJ, Nagy G, Turner JN, Roysam B (2002) Rapid automated three-dimensional tracing of neurons from confocal image stacks. *IEEE Trans Inf Technol Biomed* 6:171-187.
- Bakkum DJ (2007) Thesis In: *Biomedical Engineering*. Atlanta, GA: Georgia Institute of Technology.
- Belien JAM, van Ginkel H, Tekola P, Ploeger LS, Poulin NM, Baak JPA, van Diest PJ (2002) Confocal DNA cytometry: A contour-based segmentation algorithm for automated three-dimensional image segmentation. *Cytometry* 49:12-21.
- Benabid AL, Wallace B, Mitrofanis J, Xia C, Piallat B, Fraix V, Batir A, Krack P, Pollak P, Berger F (2005) Therapeutic electrical stimulation of the central nervous system. *Comptes Rendus Biologies* 328:177-186.
- Berridge MJ, Lipp P, Bootman MD (2000) The versatility and universality of calcium signalling. *Nature Reviews Molecular Cell Biology* 1:11-21.
- Bhadra N, Kilgore KL (2004) Direct current electrical conduction block of peripheral nerve. *Ieee Transactions on Neural Systems and Rehabilitation Engineering* 12:313-324.
- Blum RA, Ross JD, Brown EA, DeWeerth SP (2007) An Integrated System for Simultaneous, Multichannel Stimulation and Recording. *IEEE Transactions on Circuits and Systems* In Press.
- Blum RA, Ross JD, Simon CM, Brown EA, Harrison RR, DeWeerth SP (2003). A custom multielectrode array with integrated low-noise preamplifiers. In: *Proceedings of the 25th Annual International Conference of the IEEE Engineering in Medicine and Biology Society*, pp 3396-3399. Cancun, Mexico: IEEE.
- Borkholder DA (1998) Cell based biosensors using microelectrodes. In: *Electrical Engineering*. Stanford, CA: Stanford University.

- Bostock H, Cikurel K, Burke D (1998) Threshold tracking techniques in the study of human peripheral nerve. *Muscle & Nerve* 21:137-158.
- Brown EA, Ross JD, Blum RA, Wheeler BC, Nam Y, DeWeerth SP (2008) Stimulus Artifact Elimination in a Multielectrode Array System. *IEEE Transactions on Biomedical Circuits and Systems* Submitted.
- Butovas S, Schwarz C (2003) Spatiotemporal effects of microstimulation in rat neocortex: A parametric study using multielectrode recordings. *Journal of Neurophysiology* 90:3024-3039.
- Byers C, Zimmerman P, Feinstein P, Sutter M. (1986). Iridium treatment of neurostimulating electrodes. US Patent 4721551.
- Chawla MK, Lin G, Olson K, Vazdarjanova A, Burke SN, McNaughton BL, Worley PF, Guzowski JF, Roysam B, Barnes CA (2004) 3D-catFISH: a system for automated quantitative three-dimensional compartmental analysis of temporal gene transcription activity imaged by fluorescence in situ hybridization. *J Neurosci Methods* 139:13-24.
- Chiappalone M, Vato A, Tedesco MB, Marcoli M, Davide F, Martinoia S (2003) Networks of neurons coupled to microelectrode arrays: a neuronal sensory system for pharmacological applications. *Biosensors & Bioelectronics* 18:627-634.
- Cossart R, Aronov D, Yuste R (2003) Attractor dynamics of network UP states in the neocortex. *Nature* 423:283-288.
- Crespo J, Maoio V (1999) Shape preservation in morphological filtering and segmentation. In, pp 247-256.
- de Haro C, Mas R, Abadal G, Munoz J, Perez-Murano F, Dominguez C (2002) Electrochemical platinum coatings for improving performance of implantable microelectrode arrays. *Biomaterials* 23:4515-4521.
- Durand DM, Bikson M (2001) Suppression and control of epileptiform activity by electrical stimulation: A review. *Proceedings of the Ieee* 89:1065-1082.
- Franks W, Schenker W, Schmutz P, Hierlemann A (2005) Impedance characterization and modeling of electrodes for biomedical applications. *Ieee Transactions on Biomedical Engineering* 52:1295-1302.
- Fromherz P, Brittinger M, Gleixner R, Schmidtner M, Schoen I, Ulbrich M (2005) Two-way interfacing of silicon chips with Na and K channels. *Biophysical Journal* 88:386A-387A.

- Gesteland RC, Howland B, Lettvin JY, Pitts WH (1959) Comments on Microelectrodes. *Proceedings of the Institute of Radio Engineers* 47:1856-1862.
- Ghodsian B, Jung CW, Cetiner BA, De Flaviis F (2005) Development of RF-MEMS switch on PCB substrates with polyimide planarization. *Ieee Sensors Journal* 5:950-955.
- Gholmieh G, Courellis S, Fakheri S, Cheung E, Marmarelis V, Baudry M, Berger T (2003) Detection and classification of neurotoxins using a novel short-term plasticity quantification method. *Biosensors & Bioelectronics* 18:1467-1478.
- Giovangrandi L, Gilchrist KH, Whittington RH, Kovacs GTA (2006) Low-cost microelectrode array with integrated heater for extracellular recording of cardiomyocyte cultures using commercial flexible printed circuit technology. *Sensors and Actuators B-Chemical* 113:545-554.
- Gladstein M, Guterman H (2001) A novel method of controlling metal deposition during a pulse plating process. *Plating and Surface Finishing* 88:78-79.
- Gladstein M, Guterman H (2005) A new method of current density control during the pulse plating process. *Transactions of the Institute of Metal Finishing* 83:148-153.
- Gobel W, Kampa BM, Helmchen F (2007) Imaging cellular network dynamics in three dimensions using fast 3D laser scanning. *Nature Methods* 4:73-79.
- Gonzalez RC, Woods RE (2002) *Digital Image Processing, Second Edition*. New Jersey: Prentice Hall.
- Gozani SN, Miller JP (1994) Optimal Discrimination and Classification of Neuronal Action-Potential Wave-Forms from Multiunit, Multichannel Recordings Using Software-Based Linear Filters. *IEEE Transactions on Biomedical Engineering* 41:358-372.
- Greenberg RJ, Velte TJ, Humayun MS, Scarlatis GN, de Juan E (1999) A computational model of electrical stimulation of the retinal ganglion cell. *IEEE Transactions on Biomedical Engineering* 46:505-514.
- Grill WM, Mortimer JT (1995a) Stimulus Wave-Forms for Selective Neural Stimulation. *IEEE Engineering in Medicine and Biology Magazine* 14:375-385.
- Grill WM, Mortimer JT (1995b) Stimulus waveforms for selective neural stimulation. *Engineering in Medicine and Biology Magazine, IEEE* 14:375-385.
- Harrison RR, Charles C (2003) A low-power low-noise CMOS amplifier for neural recording applications. *IEEE Journal of Solid-State Circuits* 38:958-965.

- Hornig R, Eckmiller R (2001) Optimizing stimulus parameters by modeling multi-electrode electrical stimulation for retina implants. In: International Joint Conference on Neural Networks, pp 860-865. Washington, DC, USA: IEEE.
- Ikegaya Y, Le Bon-Jego M, Yuste R (2005) Large-scale imaging of cortical network activity with calcium indicators. *Neuroscience Research* 52:132-138.
- Irinopoulou T, Vassy J, Beil M, Nicolopoulou P, Encaoua D, Rigaut JP (1997) Three-dimensional DNA image cytometry by confocal scanning laser microscopy in thick tissue blocks of prostatic lesions. *Cytometry* 27:99-105.
- Janders M, Egert U, Stelzle M, Nisch W (1997) Novel thin film titanium nitride micro-electrodes with excellent charge transfer capability for cell stimulation and sensing applications. In: Proceedings of the 18th Annual International Conference of the IEEE Engineering in Medicine and Biology Society, pp 245-247. Amsterdam, Netherlands: IEEE.
- Jimbo Y, Robinson HPC, Kawana A (1993) Simultaneous Measurement of Intracellular Calcium and Electrical-Activity from Patterned Neural Networks in Culture. *IEEE Transactions on Biomedical Engineering* 40:804-810.
- Jimbo Y, Tateno T, Robinson HPC (1999) Simultaneous induction of pathway-specific potentiation and depression in networks of cortical neurons. *Biophysical Journal* 76:670-678.
- Jimbo Y, Kasai N, Torimitsu K, Tateno T, Robinson HPC (2003) A system for MEA-based multisite stimulation. *IEEE Transactions on Biomedical Engineering* 50:241-248.
- Jolly CN, Spelman FA, Clopton BM (1996) Quadrupolar stimulation for cochlear prostheses: Modeling and experimental data. *IEEE Transactions on Biomedical Engineering* 43:857-865.
- Koh IYY, Lindquist WB, Zito K, Nimchinsky EA, Svoboda K (2002) An image analysis algorithm for dendritic spines. *Neural Computation* 14:1283-1310.
- Kovacs GT, ed (1994) Introduction to the Theory, Design, and Modeling of Thin-Film Microelectrodes for Neural Interfaces. London: Academic Press, Inc.
- Kumar J, Shunmugam MS (2006) Morphological operations on engineering surfaces using a 3D-structuring element of an appropriate size. *Measurement Science & Technology* 17:2655-2664.
- Kumar K, Toth C, Nath RK (1997) Deep brain stimulation for intractable pain: A 15-year experience. *Neurosurgery* 40:736-746.

- Lin G, Adiga U, Olson K, Guzowski JF, Barnes CA, Roysam B (2003) A hybrid 3D watershed algorithm incorporating gradient cues and object models for automatic segmentation of nuclei in confocal image stacks. *Cytometry Part A* 56A:23-36.
- Lin G, Chawla MK, Olson K, Guzowski JF, Barnes CA, Roysam B (2005a) Hierarchical, model-based merging of multiple fragments for improved three-dimensional segmentation of nuclei. *Cytometry A* 63:20-33.
- Lin G, Bjornsson CS, Smith KL, Abdul-Karim MA, Turner JN, Shain W, Roysam B (2005b) Automated image analysis methods for 3-D quantification of the neurovascular unit from multichannel confocal microscope images. *Cytometry A* 66:9-23.
- Marrese CA (1987) Preparation of Strongly Adherent Platinum Black Coatings. *Analytical Chemistry* 59:217-218.
- McIntyre CC, Grill WM (2000) Selective microstimulation of central nervous system neurons. *Annals of Biomedical Engineering* 28:219-233.
- McIntyre CC, Grill WM (2001) Finite element analysis of the current-density and electric field generated by metal microelectrodes. *Annals of Biomedical Engineering* 29:227-235.
- Mehenti NZ, Tsien GS, Leng T, Fishman HA, Bent SF (2006) A model retinal interface based on directed neuronal growth for single cell stimulation. *Biomedical Microdevices* 8:141-150.
- Meijering E, Jacob M, Sarria JCF, Steiner P, Hirling H, Unser M (2004) Design and validation of a tool for neurite tracing and analysis in fluorescence microscopy images. *Cytometry Part A* 58A:167-176.
- Merz M, Fromherz P (2005) Silicon chip interfaced with a geometrically defined net of snail neurons. *Advanced Functional Materials* 15:739-744.
- Meyer RD, Cogan SF, Nguyen TH, Rauh RD (2001) Electrodeposited iridium oxide for neural stimulation and recording electrodes. *Neural Systems and Rehabilitation Engineering, IEEE Transactions on* [see also *IEEE Trans on Rehabilitation Engineering*] 9:2-11.
- Meyer T, Boven KH, Gunther E, Fejtl M (2004) Micro-electrode arrays in cardiac safety pharmacology - A novel tool to study QT interval prolongation. *Drug Safety* 27:763-772.
- Morin F, Nishimura N, Griscom L, LePioufle B, Fujita H, Takamura Y, Tamiya E (2006) Constraining the connectivity of neuronal networks cultured on microelectrode

- arrays with microfluidic techniques: A step towards neuron-based functional chips. *Biosensors & Bioelectronics* 21:1093-1100.
- Morin FO, Takamura Y, Tamiya E (2005) Investigating neuronal activity with planar microelectrode arrays: Achievements and new perspectives. *Journal of Bioscience and Bioengineering* 100:131-143.
- Najafi K, Wise K (1986) An implantable multielectrode array with on-chip signal processing. *IEEE Journal of Solid-State Circuits* 21:1035-1044.
- Nowak LG, Bullier J (1998a) Axons, but not cell bodies, are activated by electrical stimulation in cortical gray matter I. Evidence from chronaxie measurements. *Experimental Brain Research* 118:477-488.
- Nowak LG, Bullier J (1998b) Axons, but not cell bodies, are activated by electrical stimulation in cortical gray matter II. Evidence from selective inactivation of cell bodies and axon initial segments. *Experimental Brain Research* 118:489-500.
- Potter SM, DeMarse TB (2001) A new approach to neural cell culture for long-term studies. *Journal of Neuroscience Methods* 110:17-24.
- Potter SM, Wagenaar DA, DeMarse TB (In Press) Closing the Loop: Stimulation Feedback Systems for Embodied MEA Cultures. In: *Advances in Network Electrophysiology Using Multi-electrode Arrays* (Taketani M, Baudry M, eds). New York: Springer.
- Rattay F (1999) The basic mechanism for the electrical stimulation of the nervous system. *Neuroscience* 89:335-346.
- Robinson HPC, Kawahara M, Jimbo Y, Torimitsu K, Kuroda Y, Kawana A (1993) Periodic Synchronized Bursting and Intracellular Calcium Transients Elicited by Low Magnesium in Cultured Cortical-Neurons. *Journal of Neurophysiology* 70:1606-1616.
- Rodenhiser KL, Spelman FA (1995) A Method for Determining the Driving Currents for Focused Stimulation in the Cochlea. *IEEE Transactions on Biomedical Engineering* 42:337-342.
- Sarti A, de Solorzano CO, Lockett S, Malladi R (2000) A geometric model for 3-D confocal image analysis. *IEEE Transactions on Biomedical Engineering* 47:1600-1609.
- Sekirnjak C, Hottowy P, Sher A, Dabrowski W, Litke AM, Chichilnisky EJ (2006) Electrical stimulation of mammalian retinal ganglion cells with multielectrode arrays. *Journal of Neurophysiology* 95:3311-3327.

- Smetters D, Majewska A, Yuste R (1999) Detecting action potentials in neuronal populations with calcium imaging. *Methods* 18:215-221.
- Solorzano C RE, Jones A, Pinkel D, Gray JW, Sudar D (1999) Segmentation of Confocal Microscope Images of Cell Nuclei in Thick Tissue Sections. *Journal of Microscopy* 193:212-226.
- Stenger DA, Gross GW, Keefer EW, Shaffer KM, Andreadis JD, Ma W, Pancrazio JJ (2001) Detection of physiologically active compounds using cell-based biosensors. *Trends in Biotechnology* 19:304-309.
- Stett A, Ebert U, Guenther E, Hofmann F, Meyer T, Nisch W, Haemmerle H (2003) Biological application of microelectrode arrays in drug discovery and basic research. *Analytical and Bioanalytical Chemistry* 377:486-495.
- Stosiek C, Garaschuk O, Holthoff K, Konnerth A (2003) In vivo two-photon calcium imaging of neuronal networks. *Proceedings of the National Academy of Sciences of the United States of America* 100:7319-7324.
- Tekola P, Baak JPA, VanGinkel H, Belien JAM, VanDiest PJ, Broeckaert MAM, Schuurmans LT (1996) Three-dimensional confocal laser scanning DNA ploidy cytometry in thick histological sections. *Journal of Pathology* 180:214-222.
- Thakur PH, Lu HZ, Hsiao SS, Johnson KO (2007) Automated optimal detection and classification of neural action potentials in extra-cellular recordings. *Journal of Neuroscience Methods* 162:364-376.
- Tsien RW, Tsien RY (1990) Calcium Channels, Stores, and Oscillations. *Annual Review of Cell Biology* 6:715-760.
- Veraart C, Grill WM, Mortimer JT (1993) Selective Control of Muscle Activation with a Multipolar Nerve Cuff Electrode. *IEEE Transactions on Biomedical Engineering* 40:640-653.
- Wagenaar DA, Pine J, Potter SM (2004) Effective parameters for stimulation of dissociated cultures using multi-electrode arrays. *Journal of Neuroscience Methods* 138:27-37.
- Wagenaar DA, Madhavan R, Pine J, Potter SM (2005) Controlling bursting in cortical cultures with closed-loop multi-electrode stimulation. *Journal of Neuroscience* 25:680-688.
- Wearne SL, Rodriguez A, Ehlenberger DB, Rocher AB, Henderson SC, Hof PR (2005) New techniques for imaging, digitization and analysis of three-dimensional neural morphology on multiple scales. *Neuroscience* 136:661-680.

- Weiland JD, Anderson DJ, Humayun MS (2002) In vitro electrical properties for iridium oxide versus titanium nitride stimulating electrodes. *IEEE Transactions on Biomedical Engineering* 49:1574-1579.
- Wong ROL (1998) Calcium imaging and multielectrode recordings of global patterns of activity in the developing nervous system. *Histochemical Journal* 30:217-229.
- Wong ROL, Meister M, Shatz CJ (1993) Transient Period of Correlated Bursting Activity During Development of the Mammalian Retina. *Neuron* 11:923-938.
- Zhang Y, Zhou XB, Degterev A, Lipinski M, Adjero D, Yuan JY, Wong STC (2007) A novel tracing algorithm for high throughput imaging - Screening of neuron-based assays. *Journal of Neuroscience Methods* 160:149-162.